Mon. Not. R. astr. Soc. (1992) **256**, 589–623

Optical properties of active galaxies with ultra-soft X-ray spectra

E. M. Puchnarewicz,[1] K. O. Mason,[1] F. A. Córdova,[2] J. Kartje,[2,3] G. Branduardi-Raymont,[1] J. P. D. Mittaz,[1] P. G. Murdin[4]★ and J. Allington-Smith[5]

[1] *Mullard Space Science Laboratory, University College London, Holmbury St Mary, Dorking, Surrey RH5 6NT*
[2] *Department of Astronomy, 525 Davey Lab, Pennsylvania State University, University Park, PA 16802, USA*
[3] *University of Chicago, 5640 S Ellis Avenue, Chicago, IL 60637, USA*
[4] *Royal Greenwich Observatory, Madingley Road, Cambridge CB3 0EZ*
[5] *Durham University, South Road, Durham DH1 3LE*

Accepted 1991 December 31. Received 1991 December 20; in original form 1991 September 27

SUMMARY

The optical properties of a sample of 53 active galactic nuclei (AGN) which exhibit an ultra-soft X-ray excess are examined. These AGN have been identified as part of the Ultra-Soft Survey (USS) which is selected from *Einstein* IPC sources. We present optical spectra of 27 of these AGN from which we measure continuum and line parameters, including fluxes, line FWHM and equivalent widths. Accurate *B* and *R* magnitudes are measured from CCD images. A UV spectrum of one USS AGN, E0132–411, has been obtained with *IUE* and is combined with the optical and X-ray data to produce a multiwavelength spectrum. We find a large proportion of narrow-line objects among the USS AGN: a comparison of the USS Hβ FWHM distribution with other X-ray selected samples confirms that the permitted lines of the USS AGN are biased to narrow widths. Two possible reasons for this are discussed; either we are looking at a face-on broad-line region (BLR), or the BLR lies further away from the central source than for other AGN. We compare optical line and continuum properties of the USS AGN with their separate hard and soft X-ray component luminosities and with the optical properties of other samples. We find that we are unable to distinguish the USS AGN from other X-ray selected objects on the basis of their optical luminosity. However, the strengths of the permitted lines are relatively low. The optical to X-ray ratio, α_{ox}, is calculated and we define a corresponding ratio for the soft component, α_{os}. The effective α_{ox} for the USS AGN is high, 1.36 ± 0.04, and demonstrates that their mean hard X-ray luminosity is depressed relative to their mean optical luminosity. Optical Fe II emission is generally seen in those objects which have no significant hard X-ray emission, contradicting hard X-ray dependent models for their production, and favouring the Joly model which requires no ionizing continuum. All results are considered in the context of two models for the production of a strong soft X-ray flux, accretion discs and the cool clouds model of Guilbert & Rees. An association of a face-on BLR with an accretion disc in the USS AGN would strongly favour geometrically thick discs over thin.

Key words: accretion, accretion discs – galaxies: active – galaxies: nuclei – X-rays: galaxies.

1 INTRODUCTION

Evidence is growing that soft X-ray excesses may exist in all active galaxies. The first clear indication of a nuclear soft X-ray component was found by Arnaud *et al.* (1985) in the *EXOSAT* spectrum of Mkn 841, a low-redshift ($z = 0.037$) Seyfert 1 galaxy. Turner & Pounds (1989) have reported that in their sample of 48 hard X-ray selected Seyfert galaxies detected with *EXOSAT*, 50 per cent of the unobscured objects have soft X-ray 'excesses'. Fits to *Einstein* IPC data of X-ray bright AGN require a mean 0.1–4.0-keV energy index of ~1 (Wilkes & Elvis 1987; Canizares & White 1989; Kruper, Urry & Canizares 1990), significantly steeper

★Present address: Royal Observatory, Blackford Hill, Edinburgh EH9 3HJ.

than the canonical slope at higher energies (0.7, e.g. Mushotzky 1984; Turner & Pounds 1989). Similar results are inferred from the brightness distribution of *EXOSAT* serendipitous sources (Branduardi-Raymont *et al.* 1985; Giommi *et al.* 1991). This strong, soft component is usually interpreted as the high-energy tail of the 'big blue bump' which is often thought to represent the thermal emission of an accretion disc.

The Ultra-Soft Survey (USS; Córdova & Kartje 1989; Córdova *et al.* 1992; hereafter C92) was undertaken to collate and examine the softest sources detected with the Imaging Proportional Counter (IPC) on the *Einstein Observatory.* Originally designed to search for hot, isolated neutron stars, it selects objects which have a distinct soft component with an 'effective temperature' of the order of 10 eV. These X-ray spectra are similar to those of hot white dwarfs (e.g. Sirius B and HZ 43), polar cataclysmic variables and some nearby stars (e.g. α Cen and Procyon).

There are 230 'candidate' sources in the USS and of these, 136 are classified as 'secure' sources which have a relatively high soft-component significance. Selection is based on the ratios of counts in three bands, $C1 = 0.16-0.56$ keV, $C2 = 0.56-1.08$ keV and $C3 = 1.08-3.5$ keV. For inclusion in the USS a source must satisfy the criteria $R1 = C2/C1 < 0.36$ and signal-to-noise ratio ≥ 3. 'Secure' USS sources are those for which $(R1 + \sigma_{R1}) < 0.6$. In addition, a secure source must be located in regions of the detector field of view which are free from shadowing by the window support ribs. These ribs can potentially distort the apparent energy distribution of source counts (see C92 for more details).

A programme of optical identifications has begun to determine the nature of these objects. Of the 230 candidate sources, 165 have been identified so far and of these, 53, or 32 per cent, are associated with active galaxies. This sample of ultra-soft X-ray emitting AGN, the first of its kind to be selected on the basis of soft X-ray emission, provides a unique perspective on the circumstances in which soft X-ray components are seen in active galaxies.

In this paper, we present and analyse optical data for this sample of AGN. In Section 2, catalogue identifications and the spectroscopic identification procedure are detailed and the identification confidence is discussed. Reduction of the spectra and measurements of the line and continuum parameters are detailed in Section 3, and the AGN are classified according to the convention of Stephens (1989). In Section 4, we give details of optical CCD observations and measurements of B and R magnitudes. Broad-band and monochromatic continuum luminosities have been calculated in the rest-frame of the AGN and are described in Section 5. Section 6 pays particular attention to E0132 − 411, whose X-ray count spectrum has a relatively high statistical quality. The X-ray data are combined with optical and UV spectra to create a multiwavelength spectrum, which we compare with that of a nearby Seyfert galaxy, Mkn 841. In Section 7, the X-ray and optical continuum properties of the *secure* USS AGN are compared with two other X-ray selected samples, the *Einstein* Extended Medium Sensitivity Survey (hereafter EMSS; Gioia *et al.* 1990; Stocke *et al.* 1991; Maccacaro *et al.*, in preparation) and the *EXOSAT* High Galactic Latitude Survey (hereafter HGLS; Giommi *et al.* 1991). We then look for correlations between X-ray and optical parameters (continuum and lines, including Fe II) for those secure and non-secure USS AGN for which we have optical spectra (22 AGN). Optical line emission properties of the USS AGN are compared with those of other appropriate samples. Finally, in Section 8, current models for the soft and hard X-ray emission are reviewed briefly, as are models for production of the permitted lines and the optical Fe II blends. The results from Section 7 are then discussed and interpreted in the context of these models. The Appendix contains notes on individual sources.

2 THE USS AGN

Table 1 lists the USS AGN and is divided into three sections. The first section contains the 'secure' USS sources and the second the remaining 'candidate' USS sources (see Section 1). The third section contains sources on the borderline which fail to satisfy the present USS criteria.† These non-USS sources are listed for information only as possible ultra-soft AGN and, while measurements of optical and X-ray parameters have been made in the same way as for the secure and non-secure sources, these have *not* been included in the analysis and discussion of the results.

2.1 Finding charts

In Fig. 1, we present finding charts for all of the USS sources except those only listed in the EMSS, which may be found in Maccacaro *et al.* (in preparation). These finding charts were made using facilities kindly made available to us by the Space Telescope Science Institute in Baltimore. The AGN is identified by the number 1 on the finding chart, except for E0957 + 561 which is a double (gravitationally lensed) quasar; in this case the two components are labelled 1 and 2. Other labelled objects were examined while searching for the optical counterpart, either spectroscopically in the case of stars, or visually using the William Herschel Telescope (WHT) TV camera for the two galaxies in the fields of E1425 + 169 and E1805 + 700. The numbers on the charts correspond to the 'Star No.' in Table 2.

2.2 The spectroscopic identification procedure

Of the 53 USS AGN (secure and non-secure sources), 22 were independently spectroscopically identified by us during three separate observing runs. As the first step in the optical identification procedure, we examined all the objects near the source's X-ray position on red and blue Palomar Observatory Sky Survey (POSS) plates in the north and SERC J and ESO B plates in the south. Objects which showed unusual colours (e.g. a strong blue excess) were examined first at the telescope. If a positive identification was made but there were other unusual objects in the error circle, then these were also examined. If there was no positive identification or if there were no unusual objects within the error circle, then all objects were examined in and around the X-ray error box, until we found one that was a plausible counterpart of the soft X-ray source.

†It should be noted that since Córdova & Kartje (1989), minor revisions have been made to the criteria for inclusion in the USS; see C92 for the details of these changes.

Table 1. *Einstein* ultra-soft survey of AGN.

Object	J2000 RA	J2000 Dec.	V magnitude m_V	V magnitude Note	N_H 10^{20} cm^{-2}	z	Catalogue cross-ref
SECURE USS							
E0111–015	01 14 27.4	–01 16 34	17.70	(4)	3.67	0.12	HB, EMSS
E0114–016	01 17 10.1	–01 24 39	19.29	(4)	4.3	0.34	EMSS
E0131–408	01 33 51.8	–40 39 06	19.8	(3)	2.11	2.36	HB
E0132–411*	01 34 57.6	–40 56 23	17.47	(5)	2.14	0.27	
E0136–250	01 38 43.1	–24 50 33	17.8	(4)	1.2	0.31	EMSS
E0310–557	03 11 48.3	–55 32 37	17.0:	(4)	1.8	0.23	EMSS
E0331–365	03 33 12.8	–36 19 48	18.0	(4)	1.4	0.31	EMSS
E0845+378	08 48 19.3	+37 40 05	18.03	(4)	3.36	0.31	HB, EMSS
E0944+464*	09 47 18.1	+46 15 09	18.6	(2)	1.30	0.35	
E0957+561*	10 01 27.8	+55 53 28	16.7	(3)	1.28	1.41	HB
E1028+310*	10 31 38.9	+30 46 46	19.50	(1)	1.86	0.25	
E1040+123	10 42 44.7	+12 03 31	17.29	(3)	2.7	1.03	HB
E1146+558*	11 48 52.6	+55 36 02	19.61	(1)	1.30	0.44	
E1208+322	12 10 37.7	+31 57 05	16.71	(6)	1.87	0.39	HB
E1227+140**	12 29 34.2	+13 46 29	17.3	(2)	2.11	0.10	HB
E1251–005	12 53 37.3	–00 48 11	18.45	(4)	1.6	0.43	EMSS
E1254+221	12 56 59.0	+21 53 40	16.98	(4)	2.6	0.19	EMSS
E1255+220	12 57 49.1	+21 44 40	18.50	(4)	2.6	0.26:	EMSS
E1255+017	12 58 21.5	+01 31 57	18.43	(4)	1.7	0.16	EMSS
E1334+038	13 37 09.8	+03 35 55	17.72	(4)	2.0	0.14	EMSS
E1346+266*	13 48 34.5	+26 22 07	18.5	(2)	1.43	0.92	
E1401+098	14 04 10.7	+09 37 45	16.6	(8)	1.98	0.43	HB
E1423+201*	14 26 13.4	+19 55 24	16.0	(2)	2.54	0.21	
E1425+169*	14 27 44.9	+16 41 11	19.1	(2)	1.75	0.22	
E1519+279	15 21 30.5	+27 44 19	18.2	(7)	2.69	0.23	HB
E1614+308	16 16 53.4	+30 45 27	18.01	(4)	2.4	0.27	EMSS
E1704+608	17 04 41.5	+60 44 30	15.28	(3)	2.26	0.37	HB
E2034–228	20 37 27.4	–22 42 48	17.8	(4)	3.8	0.26	EMSS
E2318–423	23 21 00.5	–42 03 31	18.2	(4)	1.98	0.21	HB, EMSS
NON-SECURE USS							
E0007–357	00 10 20.8	–35 26 58	16.0	(4)	1.2	0.05	EMSS
E0039–019*	00 42 20.0	–01 41 52	16.1	(2)	3.91	0.35	
E0114–002*	01 17 03.8	+00 00 27	15.9	(2)	3.53	0.04	
E0129–066*	01 32 16.7	–06 25 21	17.1	(2)	2.50	0.22	
E0141+020	01 43 57.8	+02 20 59	14.16	(9)	3.00	0.02	
E0150–102	01 53 24.1	–10 00 35	18.1	(3)	1.77	0.36	HB
E0200–089	02 03 26.1	–08 43 49	16.52	(4)	2.1	0.77	EMSS
E0337–267*	03 39 13.5	–26 36 48	15.5	(2)	1.16	0.11	
E0436–433*	04 38 00.8	–43 15 47	16.0	(2)	2.53	0.07	
E0844+377*	08 47 16.0	+37 32 18	17.3	(7)	3.61	0.45	HB
E0952+442	09 55 29.2	+43 57 34	17.28	(4)	1.15	0.47	HB, EMSS
E1008+348	10 11 50.0	+34 37 56	17.62	(8)	2.50	0.14	
E1011+496	10 15 04.3	+49 25 59	16.15	(3)	0.83	0.20:	HB
E1059+730	11 02 37.3	+72 46 38	16.32	(4)	4.03	0.09	HB, EMSS
E1215+692*	12 18 14.0	+68 59 59	19.78	(1)	1.59	1.12	
E1217+695*	12 19 25.2	+69 13 43	17.5	(7)	1.60	0.63	HB
E1218+693*	12 20 38.2	+69 05 04	17.69	(1)	1.60	0.11	
E1352+183	13 54 35.8	+18 05 17	15.5	(8)	1.84	0.15	HB
E1423+242	14 25 50.8	+24 04 02	17.2	(3)	2.70	0.65	HB
E1511+671*	15 12 24.8	+66 56 42	17.7	(2)	2.73	0.31	
E1640+537*	16 42 00.7	+53 39 51	18.1	(1)	2.54	0.14	
E1644–029	16 46 48.4	–03 04 14	17.91	(4)	9.2	0.26	EMSS
E1657+326*	16 59 00.7	+32 37 18	17.50	(1)	2.42	0.09	
E1805+700*	18 05 18.1	+70 06 21	18.49	(1)	5.68	0.19	
NON-USS							
E0906+111*	09 09 00.5	+10 59 34	16.93	(4)	4.37	0.16	EMSS
E1213+378*	12 15 29.9	+37 32 28	18.62	(1)	1.50	0.82	
E1227+140**	12 29 34.2	+13 46 29	17.40	(3)	2.29	0.10	HB
E1228+123*	12 31 13.2	+12 03 07	17.10	(3)	1.70	0.12	HB
E1304+342*	13 06 25.1	+34 01 35	17.97	(4)	1.02	0.28	HB, EMSS
E1654+352*	16 56 14.1	+35 10 14	17.58	(1)	2.28	0.80	

:Value uncertain. *Optical spectrum obtained (see Section 3 and Fig. 3). **Two USS spectra for this object, one secure and one non-USS. Optical spectrum obtained. (1) Calculated from optical spectrum (this paper) and scaled to CCD magnitudes to compensate for light lost in the slit (see Section 5.1). (2) Calculated from optical spectrum (this paper) and flux increased by a factor of 1.82 to compensate for light lost through the slit (see Section 5.1). (3) From HB catalogue. (4) From EMSS catalogue. (5) Calculated from optical spectrum (this paper): as this spectrum was taken with a wide slit, no correction to the flux was made (see Section 6). (6) From Moles *et al.* (1985). (7) From Margon, Downes & Chanan (1985). (8) From Kriss & Canizares (1982). (9) From de Ruiter & Lub (1986).

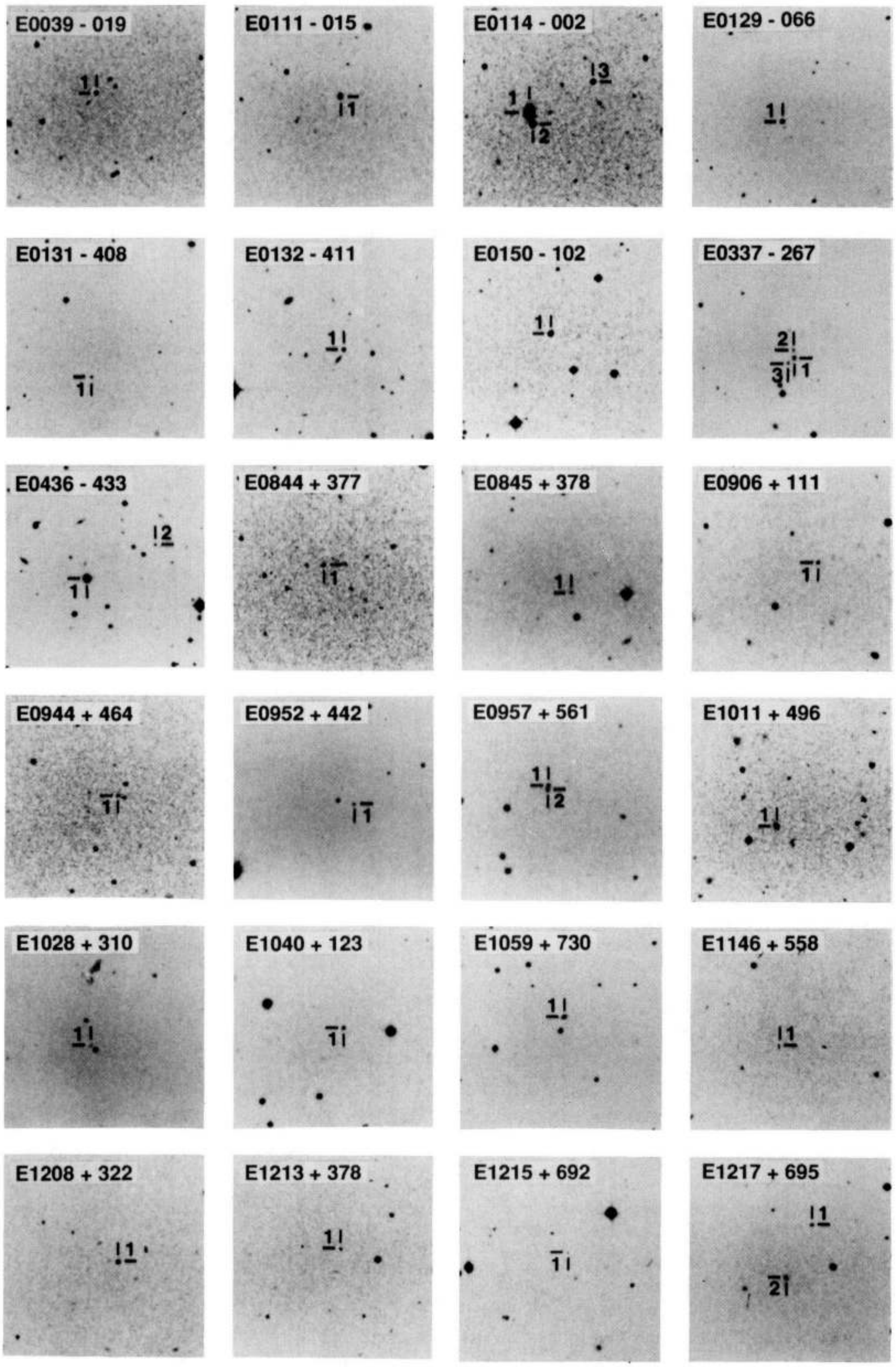

Figure 1. Finding charts for all of the USS AGN except those *only* listed in the EMSS. Each chart is 5 × 5 arcmin^2 and is centred on the USS X-ray position. The AGN is identified by the number 1, except for the double quasar E0957 + 561 whose components are labelled 1 and 2. Other labelled objects were examined at the telescope while searching for the optical counterpart of the USS source (see Section 2.1 and Table 2 for identifications of other labelled objects). Finding charts for five non-USS AGN are included (see Table 1 for the list of these objects).

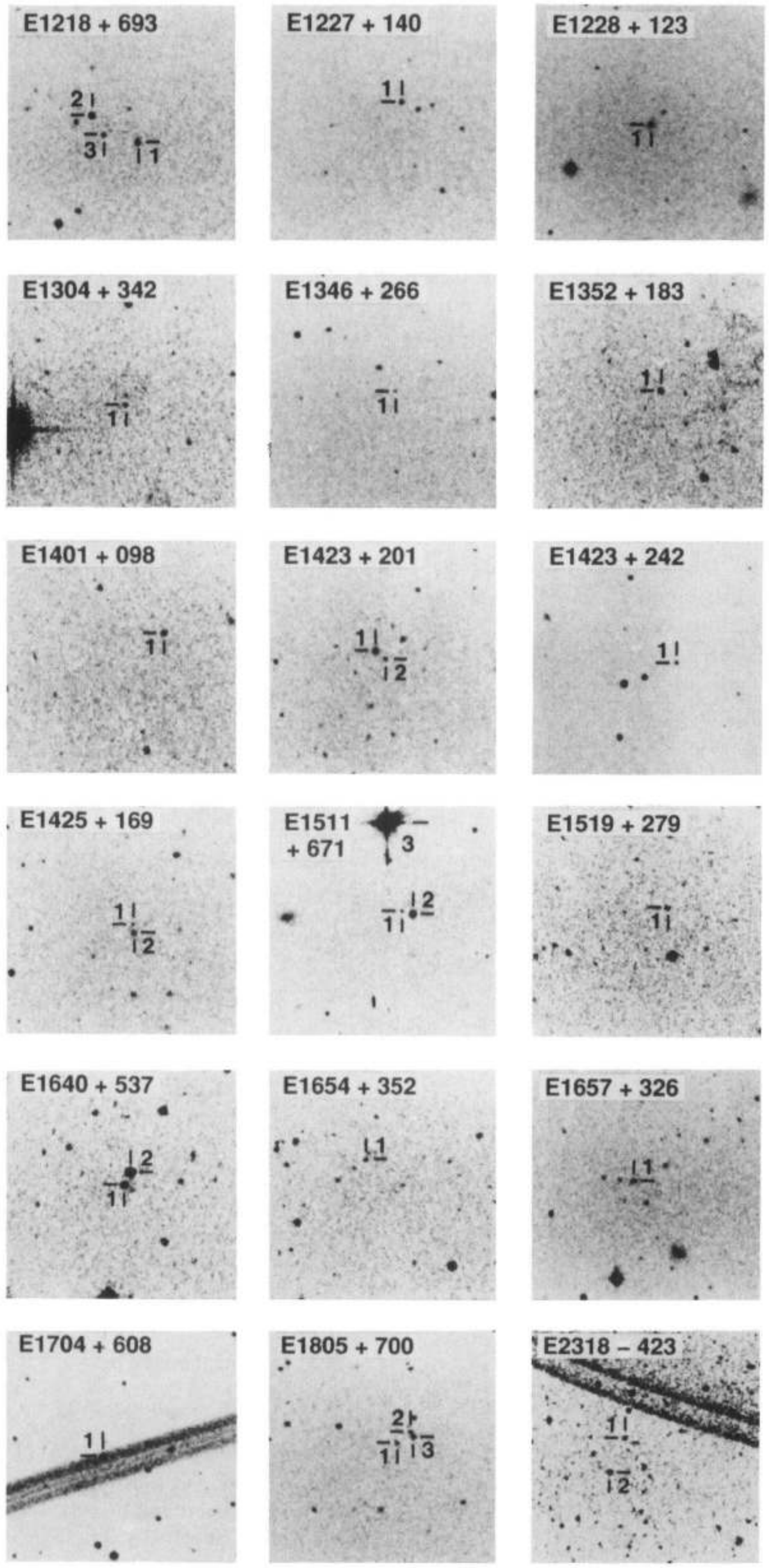

Figure 1 – *continued*

2.3 Catalogues

Given the high incidence of AGN associations revealed by our initial telescopic investigation, the Optical Catalogue of quasi-stellar objects (QSOs) (Hewitt & Burbidge 1987; hereafter HB) and EMSS catalogue were searched for AGN whose positions lay within the X-ray error circles of the USS sources (C92). A further 31 USS AGN identifications were obtained in this way. Five AGN which had been previously discovered in the spectroscopic programme were also found in these searches. In addition, E0132 − 411 had been previously optically identified by Kriss (1982). EMSS and HB catalogue identifications are indicated in Table 1.

2.4 Identification confidence

We have tested the association of USS sources with AGN by determining the separation of each AGN from the measured X-ray source position and comparing this with the probability of finding a random field star as close to the X-ray source. We measured the star density in each USS field and performed a Monte-Carlo simulation to determine the probability of finding a field star at a given distance from the X-ray source. The cumulative function, summed over all the identified AGN fields, which describes the probability that the nearest field star would lie at a given distance from the USS source by chance is shown by the solid curve in Fig. 2. The histogram shows how the separations of the USS sources from the AGN are distributed: the solid histogram is the combined sample of identifications made by us and taken from the HB catalogue while the dashed histogram isolates the HB sources not identified by us spectroscopically.

The USS AGN distribution is significantly more peaked to lower separations than expected if they were just chance associations with objects randomly distributed on the sky. Formally, there is a 2 per cent probability that the two distributions are drawn from the same parent population. Thus, even without taking into account the low surface density of AGN at this magnitude compared to stars, we can demonstrate that the association of USS sources with AGN is more likely than with any other type of object in the field. Thus, statistically, ultra-soft X-ray emission is clearly a property of this AGN sample.

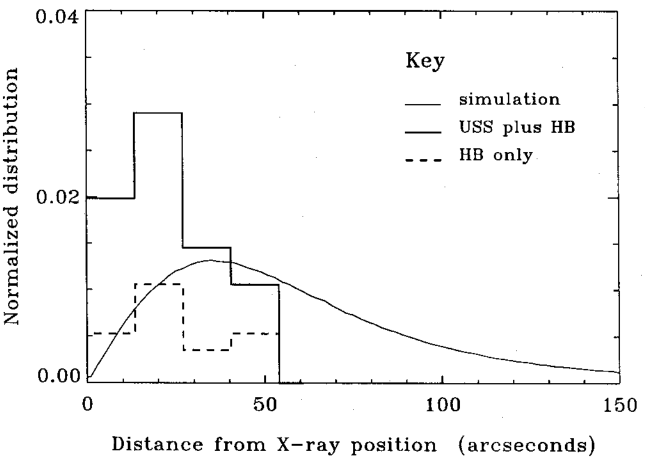

Figure 2. The distribution of separations of the USS (X-ray) sources from the optically identified AGN. The solid histogram is the combined sample of identifications made by us and taken from the HB catalogue, while the dashed histogram isolates the HB sources not independently identified by us. Also plotted, as a solid curve, is the cumulative function which describes the probability that the nearest field star would lie at a given distance from the USS source by chance. See Section 2.4 for further details.

3 OPTICAL SPECTROSCOPY

The spectra of the USS AGN were taken during three observing runs: two on the 4.2-m William Herschel Telescope at the Observatorio del Roque de los Muchachos, La Palma, and one with the 3.9-m Anglo–Australian Telescope (AAT).

The WHT spectra were taken using the Faint Object Spectrograph (FOS; Allington-Smith *et al.* 1989) mounted at the cassegrain focus of the telescope, in 1988 February and June. The FOS is a fixed-format high-throughput spectrograph, which is equipped with a dye-coated GEC CCD. It covers the spectral range from 3600 to 5000 Å in second order and from 5000 to 10 000 Å in first order, with dispersions of 5 and 9 Å pixel^{-1}, respectively.

The AAT spectra were taken in 1989 January using the RGO Spectrograph and Image Photon Counting System (IPCS) in the blue and the Faint Object Red Spectrograph (FORS) in the red. The IPCS was operated in the range 3500 to 5600 Å with data collected in 2048 channels at a dispersion of 1.5 Å pixel^{-1}. The FORS spectra covered the range 5400 to 10 000 Å in 584 channels with a dispersion of 10 Å pixel^{-1}.

A narrow spectrograph slit (between 1.0 and 1.5 arcsec) was used for the WHT and AAT spectra, except for the observation of E0132 − 411 which was made with a wide slit (4.5 arcsec) for photometric accuracy (see Section 6). Generally, the seeing was in the range 1 to 2 arcsec. All spectra were taken with the spectrograph slit at the parallactic angle. Details of the spectroscopic observations made at the WHT and the AAT are listed in Table 2.

3.1 Data reduction

The spectra were extracted and sky-subtracted using Mukai's (1990) implementation of Horne's (1986) optimal-extraction algorithm. Wavelength calibrations were derived from Cu–Ar and Hg arc spectra. Secondary calibrations for the WHT spectra were obtained from night sky lines. Observations of photometric standards were made during each night using the same instrumental set-up as for the programme stars and these were used for flux calibration. To remove atmospheric absorption features in the red, we measured the spectrum of an F8 star, taken from the SAO Catalogue, adjacent in time and sky position to each target.

3.2 Spectral analysis

3.2.1 Line identification and redshift

The spectra taken with the WHT and the AAT are shown in Fig. 3. These are plotted in the rest-frame of the AGN but no correction has been made for the effect of light lost through the spectrograph slit. The expected positions of some emission lines and Fe II blends, commonly seen in the optical spectra of AGN, are indicated.

One or both of the familiar Hβ/[O III]$\lambda\lambda$4959, 5007 and Hα/[S II]$\lambda\lambda$6717, 6731 groups of lines are clearly identifiable in most of the spectra. The positions of [O III]λ4959 and [O III]λ5007, when observed, were used to determine the redshift of the AGN. For the high-redshift AGN, the observed positions of the emission lines were compared with the rest positions of lines which often appear in AGN

Table 2. Observation summary.

Source	Star No.	Classification	Telescope	Date of Spectrum	redshift
SECURE USS					
E0132–411	1	AGN	AAT	07 JAN 89	0.27
E0944+464	1	AGN	WHT	10 FEB 88	0.35
E0957+561	1	double	WHT	16 FEB 88	1.41
	2	quasar	"	"	
E1028+310	1	AGN	WHT	11 JUN 88	0.25
E1146+558	1	AGN	WHT	08 JUN 88	0.44
E1227+140*	1	AGN	WHT	21 FEB 88	0.10
E1346+266	1	AGN	WHT	12 FEB 88	0.92
E1423+201	1	AGN	WHT	22 FEB 88	0.21
	2	star	"	"	
E1425+169	1	AGN	WHT	11 FEB 88	0.22
	2	spiral galaxy		no spectrum	
NON SECURE USS					
E0039–019	1	AGN	AAT	07 JAN 89	0.35
E0114–002	1	AGN	AAT	07 JAN 89	0.05
	2	late-type star			
	3	star			
E0129–066	1	AGN	AAT	07 JAN 89	0.22
E0337–267	1	AGN	WHT	11 FEB 88	0.11
	2	late-type star	"	"	
	3	Hα + G-band star	"	"	
E0436–433	1	AGN	AAT	07 JAN 89	0.07
	2	star	"	"	
E0844+377	1	AGN	WHT	17 FEB 88	0.46
E1215+692	1	AGN	WHT	21 FEB 88	1.12
E1217+695	1	AGN	WHT	22 FEB 88	0.64
	2	star	"	"	
E1218+693	1	AGN	WHT	14 FEB 88	0.11
	2	star	"	"	
	3	M-star	"	"	
E1511+671	1	AGN	WHT	11 JUN 88	0.31
	2	K-star	"	"	
	3	SAO star		no spectrum	
E1640+537	1	AGN	WHT	07 FEB 88	0.14
	2	K-star		"	
E1657+326	1	AGN	WHT	17 JUN 88	0.09
			"	18 JUN 88	
E1805+700	1	AGN	WHT	19 JUN 88	0.19
	2	galaxy		no spectrum	
	3	star	"	19 JUN 88	
NON-USS					
E0906+111	1	AGN	WHT	07 FEB 88	0.16
E1213+378	1	AGN	WHT	21 FEB 88	0.82
E1228+123	1	AGN	WHT	21 FEB 88	0.12
E1304+342	1	AGN	WHT	12 FEB 88	0.28
E1654+352	1	AGN	WHT	08 JUN 88	0.80

*There are two USS X-ray spectra for this object (see Table 1).

spectra, such as Mg II λ2798, C III]λ1908 and [C IV]λ1549, until a match was found. A Gaussian profile was fitted to each line to determine its centroid and the AGN's redshift was calculated by averaging the redshifts of individual lines.

3.2.2 *Measurement of line parameters*

The flux, equivalent width and FWHM of each emission line were measured and the results are presented in Table 3 together with upper limits on the more common lines that were not seen. A Gaussian profile was fitted to each line with the local continuum represented by a second-order polynomial. The line flux, equivalent width and FWHM were usually calculated directly from the data after the fitted continuum had been subtracted. For the weaker lines which are only a few pixels wide, the FWHM was taken to be that of the Gaussian fit (these are marked 'g' in the table). In cases where lines were blended, a Gaussian profile, whose FWHM was fixed to that measured for unblended lines of similar origin, was fitted to each line. The flux and equivalent width were then calculated from this Gaussian fit (in these cases, the flux, FWHM and equivalent width of the line are marked with an 'f' in Table 3). The FWHM listed in Table 3 have *not* been deconvolved from the instrumental profile (see Section 3.2.5 for details of the instrumental linewidths).

3.2.3 *Blended Fe II emission*

Fe II emission is a well-known feature of AGN spectra. Osterbrock (1977) showed that it was present in 90 per cent of Seyfert 1 galaxies. From the analysis of laboratory spectra, 675 energy levels between 900 and 50 000 Å are presently known (Johansson 1986) and the entire Fe II spectrum is complex. Lines within multiplets are blended with each other and multiplets also overlap and are blended. This may produce a 'false' continuum in a spectrum so that the actual underlying continuum is disguised. A model is required to measure the Fe II emission reliably and to estimate the strength in the Fe II spectrum. For the purposes of this paper, however, we follow previous practice (e.g. Stephens 1989) and measure the flux in two relatively well-defined optical Fe II blends between ~4500–4680 Å and ~5100–5500 Å.

For each region, the underlying continuum was represented by a first-order polynomial and the flux was summed from the data after subtracting this continuum. For E0132−411 and E1227+140, the 4500–4680-Å blend appears to be very strong and is blended with a feature that lies beneath the Hβ and [O III]$\lambda\lambda$4959, 5007 lines which may also be due to Fe II emission. This was represented by a Gaussian profile and subtracted from the data before the flux and equivalent width of the remaining iron features were measured. Fe II blend information is presented in Table 4.

3.2.4 *Continuum parameters*

A power-law model was fitted to each spectrum, having first removed the emission features. No attempt was made to subtract other contributions to the optical continuum such as contaminating starlight, Balmer continuum emission and residual blended Fe II emission. This optical power-law index, $\alpha_{\rm opt}$, is an indication of the overall observed shape of the spectrum but may not accurately reflect an intrinsic underlying power law in the optical region. A power law was not an appropriate model for some low-redshift objects where the contribution from the underlying galaxy is strong towards the red; E0436−433 is an extreme example of this and was not measured. Optical power-law indices are listed in Table 3.

3.2.5 *AGN spectral classification*

The AGN have been classified using the criteria in Stephens (1989). According to this scheme, a 'quasar' appears stellar, it has very broad permitted lines (with FWHM typically several thousands of km s^{-1}) and an optical continuum luminosity in the V band, $\log L_\nu > 40.60$ erg s^{-1}. A 'QSO' is a radio-quiet quasar. A 'Seyfert galaxy' has a stellar or semistellar nucleus and $\log L_\nu < 40.60$ erg s^{-1}. There are two main types of Seyfert galaxy; 1 and 2. 'Seyfert 1' galaxies have broad permitted lines with FWHM up to 10^4 km s^{-1} and narrow forbidden lines. In 'Seyfert 2' galaxies, the permitted and forbidden lines have similar widths of about 500 km s^{-1} and a ratio [O III]λ5007/Hβ > 3 (Shuder & Osterbrock 1981). A narrow-line (NL) Seyfert, quasar or QSO is defined as one which has an Hβ FWHM < 2000 km s^{-1} (Goodrich 1989).

1992MNRAS.256..589P

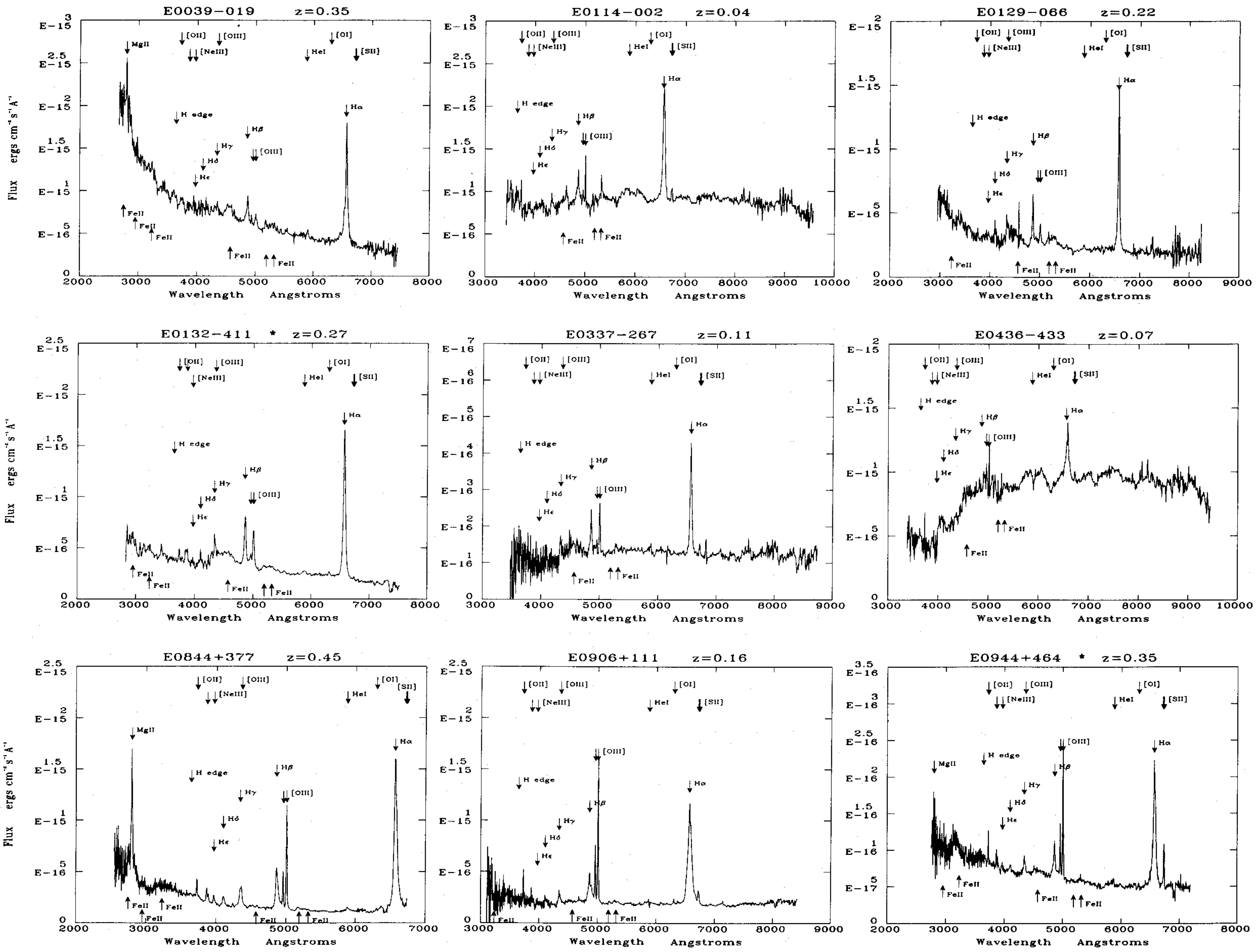

Figure 3. Optical spectra of the USS AGN taken at the WHT and the AAT. Secure USS sources are indicated with an asterisk. Each spectrum is plotted in the rest-frame of the AGN but no corrections have been made to the observed flux. Also indicated are the expected positions of some emission lines and Fe II blends commonly seen in the spectra of AGN. Spectra of five non-USS AGN are included.

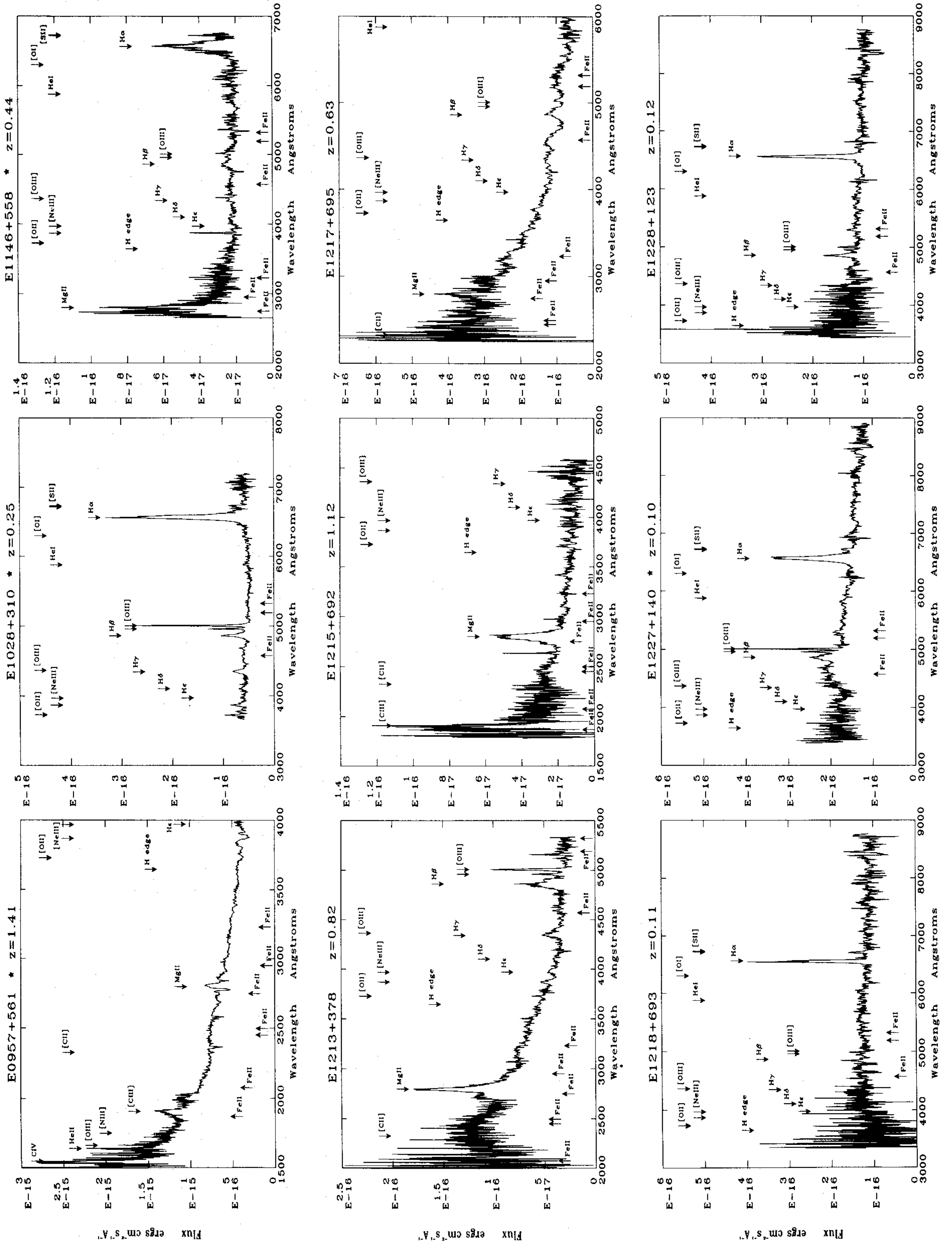

Figure 3 – *continued*

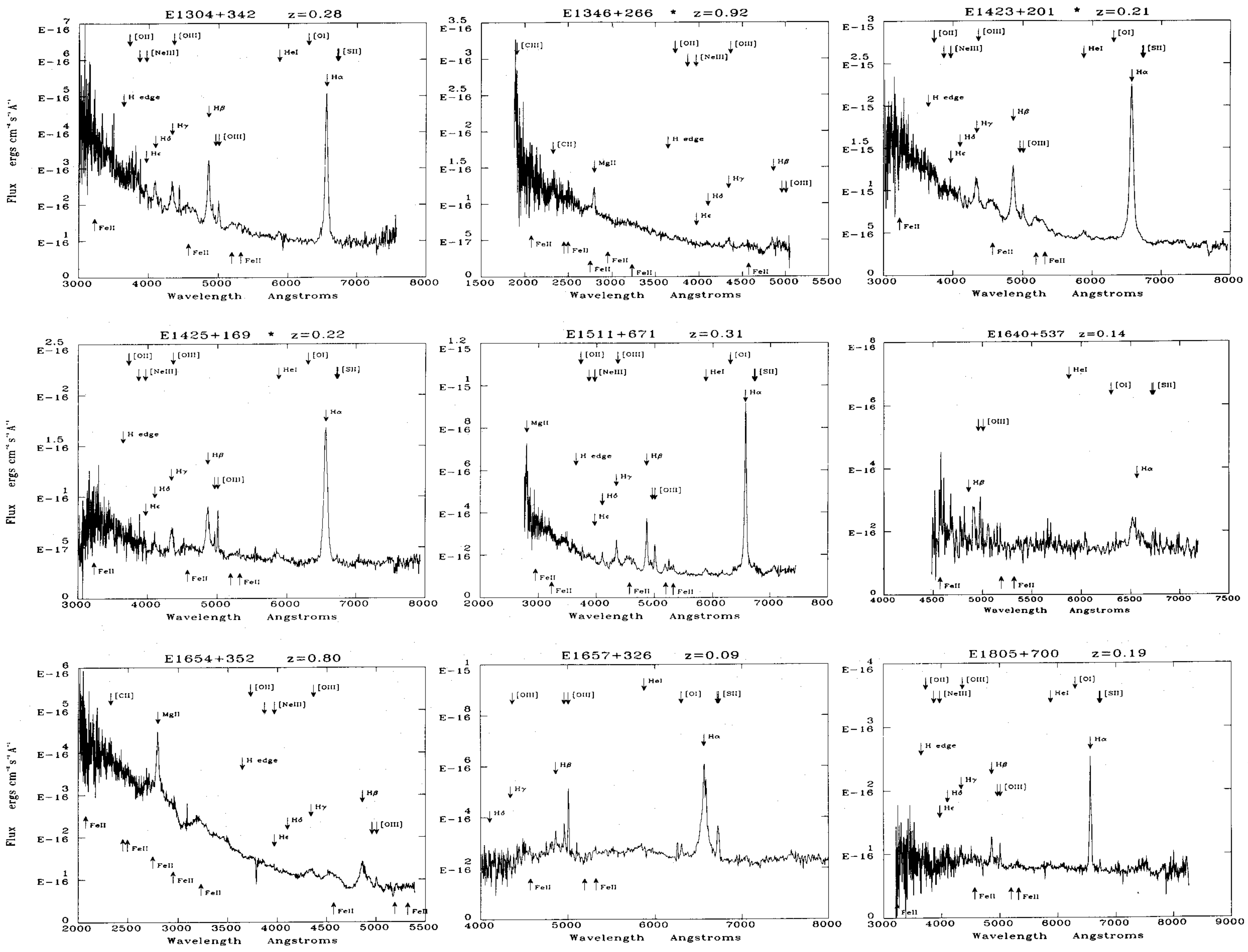

Figure 3 – *continued*

Table 3. USS AGN optical spectral parameters.

Object	s.f.	α_{opt}	2798 MGII	3430 [NeV]	3729 [OII]	3782 H10/11	3868 [NeIII]	3970 H_ϵ	4102 H_δ	4340 H_γ	4363 [OIII]	4861 H_β	4959 [OIII]	5007 [OIII]	5876 HeI	6300 [OI]	6563 H_α	6717 [SII]	6731 [SII]
E0039–019	1.8	0.3	23.4[1]	—	<2.8	—	<1.1	<1.5	<3.5	<6.6	<1.4	23.1	<0.7	9.0	4.4	—	122.7	<4.1	
			6.8[2]	—	<1.8	—	<0.8	<1.0	<2.5	<4.9	<1.0	20.5	<0.6	8.5	5.3	—	177	<6.3	
			3.4[3]	—	1.53	—	1.57	1.57	1.52	1.37	1.35	1.13	1.08	1.06	0.82	—	0.69	0.69	
			1700[4]	—	1330f	—	1280f	1960f	1890f	1820f	1370f	1690	700f	2300	1270	—	1300	1580f	
E0114–002	1.8	1.9		—	<5.2	—	<1.8	<2.1	<5.7	<0.2	<0.6	23.6	3.6	9.1	<4.1	—	125.4	—	6.8
				—	<3.4	—	<1.3	<1.5	<3.9	<5.3	<0.4	14.3	2.1	5.7	<2.3	—	73.0	—	4.2
				—	1.55	—	1.46	1.36	1.46	1.47	1.47	1.64	1.62	1.59	1.80	—	1.72	—	1.63
				—	720f	—	730f	2670f	2700f	2600f	730f	2980	750	560	2160f	—	2300	—	1250
E0129–066	1.8	0.8		—	<0.4	—	<0.8	<3.0	6.1	6.9	4.8	20.9	2.3	9.2	1.9	—	76.2	<0.5	—
				—	0.8f	—	1.6f	5.6f	11.8	12.8	8.7	46.6	5.1	20.0	4.8	—	167	1.2f	—
				—		—			0.52	0.56	0.56	0.45	0.45	0.46	0.40	—	0.45		
				—	1330f	—	1280f	2130f	2140	1460	1460	1540	1340f	1330	1340	—	1290	1050f	—
E0132–411	1.0	0.8		3.0	2.3	0.6	1.8	0.3	2.2	2.4g	2.4g	18.6	4.0	12.2	2.2	0.5	66.2	<0.4	
				7.2	6.2	1.4	5.0	0.7	6.5	5.5g	5.5g	54.7	12.6	39.1	9.0	2.0	275.0	2.1f	
				0.41	0.37	0.37	0.36	0.35	0.34	0.43	0.43	0.34	0.32	0.31	0.24	0.24	0.24	0.20	
				1660	1500	1270	970	1490	1980	790g	1940g	2080	1510g	1500	3720	1040	1760	1360f	
E0337–267	1.8	2.1		—	<0.8	—	<0.4	<0.3	1.8	2.7	0.9	5.9	1.1	5.0	0.7g	—	21.1	0.9	—
				—	3.9f	—	2.5f	1.6f	10.0	13.8	4.3	25.5	5.0	21.8	3.2	—	89.2	4.0	—
				—	0.20	—	0.18	0.18	0.18	0.20	0.21	0.23	0.23	0.23	0.24	—	0.24	0.23	—
				—	950f	—	910f	1600f	1400	1630f	970f	1560g	1000	1120	1560f	—	1710	760	—
E0436–433	1.8			—	4.9	—	<0.7	<1.2	<0.9	<2.0	<0.6	<2.7	9.6g	16.9g	<0.8	—	37.1	—	3.0
				—	6.7	—	1.0f	1.6f	0.8f	1.7f	0.5f	1.8	6.2	11.0	0.5f	—	20.7	—	1.7
				—	0.73	—	0.76	0.78	1.09	1.13	1.13	1.55	1.55	1.55	1.80	—	1.80	—	1.71
				—	700	—	550f	2310f	2410f	2280f	490f	2180f	350g	310g	2160f	—	2080	—	1220
E0844+377	1.8	0.0	84.6	—	4.8	—	5.9	3.8	5.8	14.4g	0.3g	33.9	11.7	31.0	6.8	—	151.8		
			97.2	—	10.5	—	15.4	11.1	18.8	60.8	17.7	131	47.5	128	35.2	—	597		
			0.79	—	0.46	—	0.38	0.34	0.31	0.30	0.29	0.26	0.25	0.24	0.19	—	0.25		
			2170	—	1110	—	1280	1420	1840g	1250g	1320g	2300	870	840	2390	—	2120		
E0906+111	1.8	1.9		—	6.3	—	1.9	0.7	1.9	4.5g	1.8g	24.9	14.5	41.7	<3.4	1.2	148.0	2.4	2.3
				—	16.2	—	5.3	2.0	5.7	12.6	5.2	60.3	35.9	106	<10.0	3.4	407	6.1	6.1
				—	0.38	—	0.36	0.35	0.33	0.35	0.35	0.38	0.38	0.38	0.34	0.35	0.36	0.40	0.40
				—	950	—	700	750	920	1490g	890f	3860	800	850	3000f	490	3070	450f	450f
E0944+464	1.8	1.0	1.3	0.3	0.7	—	0.6	0.2	0.6	0.9	0.3	2.1	1.6	4.8	0.3	—	15.8	1.5	—
			6.4	1.6	4.8	—	4.3	1.6	4.9	7.3	2.2	16.2	12.9	39.9	2.7	—	167	16.2	—
			0.20	0.16	0.15	—	0.14	0.13	0.13	0.14	0.14	0.12	0.12	0.12	0.10	—	0.09	0.09	—
			1700	870	1420	—	1160	1590	1930	1590f	900f	1480	700	870	1250	—	1970	620	—
E0957+561	1.0	0.3	4.36	—	<0.20	—	<0.21												
			6.7	—	<0.5	—	<0.5												
			0.65	—	0.40	—	0.39												
			3250	—	1510f	—	1500f												
E1028+310	1.0	1.7		—	0.49	—	0.65	<0.15	0.38	0.24	0.14	2.21	1.19	3.42	0.21	—	16.3	—	0.88
				—	7.9	—	10.8	2.5f	6.60	13.8	3.80	40.8	22.3	64.8	4.2	—	277	—	14.7
				—	0.062	—	0.060	0.060	0.058	0.056	0.056	0.054	0.053	0.053	0.049	—	0.059	—	0.060
				—	1260	—	1640	2130f	1150	2120f	970f	1920	810	840	1040	—	2400	—	690
E1146+558	2.5	1.3	15.83	—	<0.11	—	0.72	<0.02	<0.15	0.20g	0.04g	0.42	0.13	0.31	<0.13	—	8.49	—	0.47
			239	—	<2.1	—	13.8	<0.4	<2.8	3.6	0.74	7.3	2.4	5.5	<2.5	—	147	—	7.2
			0.066	—	0.054	—	0.050	0.050	0.054	0.054	0.054	0.056	0.054	0.054	0.054	—	0.058	—	0.066
			2120	—	950f	—	930	2080f	2050f	2280f	970f	5220g	1180	1030	2040f	—	4420g	—	50
E1213+378	1.6	0.0	8.65	—	0.19	—	0.39	0.49	0.29	1.01g	0.12g	2.58g	0.50g	1.69g					
			60.4	—	2.5	—	5.7	8.0	5.1	19.0	2.4	46.6	9.5	34.4					
			0.142	—	0.078	—	0.066	0.060	0.056	0.054	0.054	0.050	0.050	0.048					
			3460	—	650	—	1450	3260	3690g	2600	650f	3350	630	840					
E1215+692	1.8	0.5	4.82	0.28	0.29	—	<0.11	<0.15	<0.13	<0.39	<0.04								
			123	10.1	11.6	—	<4.7	<6.4	<5.4	<21.1	<2.30								
			0.038	0.028	0.024	—	0.026	0.026	0.026	0.018	0.018								
			5830	2140	1040	—	1460f	4450f	4300f	4230f	1380f								
E1217+695	1.9	0.0	5.78	—	<0.13	—	<0.21	<0.32	<1.09	<1.27	<0.06	6.43g	0.16	1.31	<1.89				
			9.9	—	<0.5	—	<0.8	<1.3	<5.8	<5.7	<0.3	40.6	1.0f	8.4	<15.9				
			0.58	—	0.28	—	0.26	0.25	0.22	0.22	0.22	0.16	0.16	0.16	0.12				
			2550g	—	1700f	—	1640f	4800f	4990f	4880f	1460f	5290g	1570f	1650	4800f				

Table 3 – *continued*

Object	s.f.	α_{opt}	2798 MGII	3430 [NeV]	3729 [OII]	3782 H10/11	3868 [NeIII]	3970 H_ϵ	4102 H_δ	4340 H_γ	4363 [OIII]	4861 H_β	4959 [OIII]	5007 [OIII]	5876 HeI	6300 [OI]	6563 H_α	6717 [SII]	6731 [SII]
E1218+693	2.6	2.0		—	<2.7	—	<1.8	<1.2	<2.7	<0.6	<0.5	2.5	1.0	1.4	<1.1	—	25.7	3.2	
				—	<10.4	—	<6.4	<3.9	<8.4	<7.7	<1.6	7.9	3.0	4.4	<3.3	—	87.3	10.9	
				—	0.23	—	0.26	0.29	0.32	0.33	0.33	0.32	0.32	0.31	0.32	—	0.29	0.29	
				—	1330f	—	1280f	1600f	1810f	1790f	1290f	1620	1280	1190	1800f	—	1860g	1160	
E1227+140	2.2	1.6		2.8	2.1	—	0.7	<0.9	<2.8	<2.8	<1.0	7.6	3.4	8.1	<0.5	—	35.6	0.5g	0.8g
				6.8	5.3	—	1.9	<2.4	<7.3	<7.1	<2.7	17.3	8.1	19.9	<1.4	—	106	2.0	3.0
				0.41	0.40	—	0.39	0.39	0.38	0.38	0.40	0.44	0.42	0.41	0.37	—	0.33	0.34	0.34
				940	800	—	730	3020f	3100f	3170f	890f	3390	1070g	830g	3730f	—	3740g	470g	650g
E1228+123	3.7	1.6		—	<4.5	—	<2.4	<4.9	<5.6	5.8g	<1.0	9.5	1.5	2.6	<1.8	—	38.2	<1.5	
				—	<9.0	—	<5.1	<10.5	<12.6	14.0	<2.4	22.6	3.7	6.2	<4.5	—	98.0	<3.8	
				—	0.52	—	0.50	0.48	0.46	0.44	0.44	0.42	0.42	0.41	0.41	—	0.39	0.39	
				—	1140f	—	1190f	1870f	1890f	2090g	1130g	1860	1150	1190	1980f	—	2030	1370f	
E1304+342	1.9	-0.1		—	<1.2	—	<0.2	2.1	3.8	4.9g	0.8g	13.6	0.2	2.3	1.9	—	45.1	<0.5	
				—	<2.2	—	<0.4	5.0	9.6	13.6	2.2	44.0	0.8	8.1	9.4	—	245	<2.5	
				—	0.52	—	0.49	0.43	0.40	0.36	0.36	0.31	0.30	0.29	0.20	—	0.18	0.18	
				—	760f	—	770f	1740	2250	2230f	760f	2180	640	910	2070	—	1950	1260	
E1346+266	1.8	0.4	1.64	—	0.18	—	0.13	<0.04	0.29	0.61g	<0.07	1.88							
			10.2	—	1.9	—	1.5	<0.6	3.8	8.3	<1.0	31.1							
			0.160	—	0.094	—	0.086	0.082	0.078	0.072	0.072	0.060							
			2560	—	1130	—	1720	1780f	1810	1790f	1290f	1900							
E1423+201	1.8	-0.1		—	<2.8	—	<2.1	4.4	8.5	31.8g	1.9g	53.1	<1.6	6.7	12.4	—	240.8	<0.8	
				—	<1.4	—	<1.1	2.5	5.3	21.0	1.3	40.6	<1.4	5.5	15.7	—	304	<1.1	
				—	2.09	—	1.91	1.74	1.61	1.64	1.62	1.31	1.18	1.22	0.79	—	0.79	0.80	
				—	1170f	—	1190f	1420	1970	3890g	700f	2850	<930	1300	1930	—	2630	1260f	
E1425+169	1.8	1.4		—	<0.23	—	<0.05	<0.33	0.91	1.91g	0.15g	4.65	0.48	1.32	0.64g	—	16.66	—	0.20
				—	<2.1	—	<0.5	<3.6	10.8	22.8	1.8	55.0	5.9	16.2	9.1	—	254	—	3.1
				—	0.112	—	0.100	0.090	0.084	0.082	0.082	0.082	0.080	0.080	0.068	—	0.064	—	0.064
				—	950f	—	970f	2670f	4280	3230g	890f	2620	600	950	2760g	—	2790	—	600
E1511+671	1.8	0.0	16.1	—	<0.2	—	<0.8	1.1	3.4	4.5g	1.4g	16.8	1.7	6.6	3.0	—	87.0	1.0	—
			23.4	—	<0.6	—	<2.4	3.4	12.0	14.8g	4.7g	71.5	7.3	29.2	15.2	—	472	4.0	—
			0.69	—	0.38	—	0.34	0.31	0.28	0.29	0.29	0.23	0.22	0.22	0.20	—	0.18	0.25	—
			2350	—	1510f	—	1520f	1410	1530	1950f	1460f	1790	870g	1410	2080	—	1740	1040	—
E1640+537	2.2	1.6								<4.2	<2.0	2.6	<0.4	1.2	<0.8	—	7.3	0.9	—
										<20.1	<9.7	15.1	<2.4	7.2	<5.7	—	48.1	6.1	—
										0.210	0.210	0.185	0.180	0.175	0.151	—	0.152	0.148	—
										1380f	1290f	1250	1140f	1130f	5050f	—	4540	650	—
E1654+352	1.4	0.0	6.15	—	<0.11	—	<0.24	<0.38	<0.35	1.35g	0.26g	6.21	<0.29	0.65					
			13.9	—	<0.5	—	<1.3	<2.1	<2.2	8.7g	1.7g	54.2	<2.5	5.7					
			0.44	—	0.216	—	0.192	0.180	0.164	0.156	0.154	0.114	0.114	0.114					
			2880	—	1230f	—	1240f	3740f	3790f	3820f	1310f	3650	1140f	1090					
E1657+326	1.4	2.0		—	7.5	—	<0.8	<0.8	<1.6	<1.6	<0.2	2.5	2.5	4.6	<0.4	1.7	45.9	—	6.9
				—	34.3	—	<3.4	<2.8	<5.3	<5.3	<0.5	6.5	6.6	12.3	<1.0	4.6	132	—	20.4
				—	0.216	—	0.230	0.258	0.288	0.302	0.302	0.374	0.374	0.374	0.384	0.360	0.346	—	0.338
				—	720	—	920f	2490f	2500f	2440f	890f	1000	920	860	2460f	900	2490	—	1400
E1805+700	1.8	1.8		—	<0.35	—	<0.76	<0.39	<0.77	0.95g	<0.34	2.34	0.48	1.02	<0.28	—	10.5	—	0.49
				—	<2.3	—	<6.0	<2.9	<5.1	6.1g	<2.2	15.6	3.3	7.2	<2.0	—	78.4	—	3.8
				—	0.078	—	0.063	0.070	0.077	0.077	0.078	0.074	0.072	0.071	0.069	—	0.066	—	0.065
				—	1510f	—	1500f	1600f	1810f	1740g	1550f	1860	1520	1620	1650f	—	1640g	—	690

[1](Flux in units of 10^{-15} erg cm^{-2} s^{-1}). [2](Equivalent width in Å). [3](Continuum flux in units of 10^{-15} erg cm^{-2} s^{-1} Å^{-1} – may include Fe II emission, Balmer continuum etc.). [4](FWHM in km s^{-1}). FWHM in this Table have *not* been deconvolved from the instrumental width. s.f. = Flux scaling factor (see Section 5.1). α_{opt} = power-law index (in F_ν) fitted to the optical continuum (see Section 3.2.4).

For the purpose of this spectral classification, we define the V-band optical continuum luminosity, L_ν, as the luminosity at 5500 Å (assuming $H_0 = 75$ km s^{-1} Mpc^{-1} and $q_0 = 1$ for consistency with Stephens). The luminosity was derived from the flux of the power-law continuum model (fitted to the rest-frame spectrum) at 5500 Å, except in the case of E0436–433 where the continuum flux was measured directly from the spectrum. The flux was corrected for light lost through the slit (see Section 5.1 for details) before the luminosity was calculated. The Hβ FWHM was deconvolved

Table 4. USS AGN optical Fe II blend parameters.

Object name	$FeII_{blue}$ 4500-4680Å	$FeII_{red}$ 5100-5500Å	Ratio $FeII_{blue}/FeII_{red}$	Hβ ratio $FeII_{blue}/H\beta$	$FeII_{red}/H\beta$
E0039–019	[1]32 [2]25 [3]1.3	30 31 0.95	1.1	1.4	1.3
E0114–002	<28 <19 1.5	<44 <28 1.6	—	<1.2	<1.9
E0129–066	38 46 0.86	65 86 0.75	0.59	1.8	3.1
E0132–411	23 79 0.29	14 52 0.26	1.7	1.2	0.74
E0337–267	6.6 29 0.23	<4.7 <20 0.23	—	1.1	<0.79
E0436–433	<31 <23 1.3	<27 <18 1.5	—	<11	<9.8
E0844+377	6.9 27 0.26	11 55 0.20	0.61	0.20	0.33
E0906+111	<11 <33 0.32	<19 <62 0.30	—	<0.83	<0.76
E0944+464	2.8 24 0.12	3.6 38 0.095	0.76	1.3	1.8
E1028+310	<2.0 <39 0.052	<1.9 <41 0.045	—	<0.90	<0.85
E1146+558	<0.49 <9.0 0.054	<1.1 <22 0.049	—	<1.2	<2.6
E1213+378	<0.82 <17 0.050		—	<0.32	
E1215+692	<0.72 <62 0.011		—		
E1217+695	10 59 0.17	20 160 0.13	0.51	1.6	3.1
E1218+693	<7.3 <25 0.29	<7.6 <25 0.30	—	<2.9	<3.0
E1227+140	18 50 0.37	<13 <36 0.36	>1.5	2.4	<1.7
E1228+123	<12 <31 0.38	<16 <42 0.38	—	<1.3	<1.7
E1304+342	9.6 31 0.32	12 50 0.23	0.84	0.71	0.84
E1346+266	1.9 30 0.063			0.98	
E1423+201	40 30 1.3	41 42 0.97	0.97	0.75	0.77
E1425+169	2.4 31 0.078	2.2 31 0.069	1.1	0.52	0.47
E1511+671	15 62 0.24	11 56 0.20	1.3	0.89	0.68
E1654+352	4.5 36 0.12			0.73	
E1657+326	<5.9 <18 0.33	<8.5 <25 0.34	—	<2.4	<3.5
E1805+700	<2.8 <20 0.14	<3.2 <25 0.13	—	<1.2	<1.4

[1](Flux in units of 10^{-15} erg cm^{-2} s^{-1}). [2](Equivalent width in Å). [3](Continuum flux in units of 10^{-15} erg cm^{-2} s^{-1} Å^{-1}; may include Fe II emission, Balmer continuum, etc.).

from the instrumental profile by assuming that the observed width is the quadrature sum of the intrinsic Hβ and instrumental FWHM, and that these lines have a Gaussian profile. Instrumental FWHM were measured from the calibration arc spectra, at 14.5 Å for the FOS and 16.0 Å for the FORS. There are two objects, E0114−002 and E0436−433, whose Hβ lines were measured with the IPCS; it was not necessary to deconvolve these lines due to the higher resolution of this detector (see Section 3).

The optical continuum luminosity at 5500 Å, deconvolved Hβ FWHM and the classification for each spectrum are listed in Table 5. Also listed are details from Stephens (1989) where USS optical spectra are not available. (The *observed* FWHM for the USS AGN are listed in Table 3.)

4 CCD IMAGING

Direct CCD images of the sources listed in Table 6 were obtained at the Isaac Newton and Jacobus Kapteyn Telescopes of the Observatorio del Roque de los Muchachos in 1989 March and May respectively. The filters used and exposure times are given in Table 6. Observations of flux standards and sky flat-fields in red and blue filters were taken at the beginning and end of each night. All of the images were corrected for bias and flat-field variations using image processing software developed at the Mullard Space Science Laboratory.

4.1 Magnitudes

Each source was fitted with a Gaussian profile superposed on a first-order polynomial to represent the sky background. Source counts were summed after subtracting the background, and count rates were converted to magnitudes by comparing them with the count rates measured for the flux standards. The AGN magnitudes have been corrected for differences in the airmass between the object and the standard. Integrated magnitudes in B and R filters, which include flux from any underlying galaxy, are presented in Table 6. We estimate errors on the magnitudes of ~ 10 per cent.

4.2 Extended sources

A measurement of the spatial extent of the AGN image in these CCD frames is also given in Table 6 as an indicator of the presence of an underlying galaxy. This is the σ of the Gaussian fitted to the AGN (see Section 4.1) in arcseconds, σ_{gal}. It has been deconvolved from the seeing profile by assuming that the observed σ is the quadrature sum of σ_{gal} and the seeing profile. For each AGN, the seeing profile was assumed to be the σ of point-like objects in the field. Upper limits are given for AGN whose profiles are not distinguishable from the point-like sources. Other details from the CCD images, e.g. morphology of the underlying galaxy, may be found in the Appendix.

5 OPTICAL AND X-RAY LUMINOSITIES

In computing the X-ray and optical luminosities of the USS AGN, we have assumed values of 50 km s^{-1} Mpc^{-1} for the Hubble constant, H_0, and 0.0 for the deceleration parameter, q_0. Optical luminosities between 3000 and 6000 Å, L_{opt}, and at 2500 Å, $L_{2500\,Å}$, in the rest-frame of the AGN were calculated and are listed in Table 7. Also listed, from C92, are the broad-band X-ray luminosities for separate soft and hard components integrated between 0.2 and 4.5 keV, L_{soft} and L_{hard}, together with monochromatic luminosities at 0.2 keV

Table 5. Spectral classifications of the USS AGN.

Object Name	Redshift	Log L_ν	FWHM Hβ km s^{-1}	Stephens Classification	Present Classification
Secure USS					
E0111–015	0.12	39.31[s]	1130[s]	NL Sey 1	
E0132–411	0.27	40.46	1930		NL Sey 1
E0845+378	0.31	40.18[s]	3450[s]	Sey 1	
E0944+464	0.35	40.23	1320		NL Sey 1
E0957+561	1.41	41.75	3250*		Double quasar
E1028+310	0.25	39.92	1780		NL Sey 1
E1146+558	0.44	40.15	5180		Sey 1
E1227+140	0.10	39.82	3290	Sey 1	Sey 1
E1346+266	0.92	40.64	1840		NL QSO
E1401+098	0.43	40.76[s]	8270[s]	quasar	
E1423+201	0.21	40.78	2750		QSO
E1425+169	0.22	39.76	2520		Sey 1
E1519+279	0.23	39.99[s]	2210[s]	Sey 1	
Non-secure USS					
E0039–019	0.35	41.21	1520		NL QSO
E0114–002	0.04	39.69	2980		Sey 1
E0129–066	0.22	40.51	1310		NL Sey 1
E0150–102	0.36	40.34[s]	3400[s]	quasar	
E0337–267	0.11	39.71	1340		NL Sey 1
E0436–433	0.07	40.14	2180		Emission line galaxy
E0844+377	0.45	40.74	2220	Sey 1	QSO
E1008+348	0.14	39.69[s]	3310[s]	Sey 1	
E1011+496	0.20				BL Lac[W]
E1059+730	0.09	39.91[s]	6630[s]	Sey 1	
E1215+692	1.12	40.13	5830*		Sey 1
E1217+695	0.63	40.81	5260		Sey 1
E1218+693	0.11	39.84	1410		HII region galaxy
E1352+183	0.15	41.01[s]	4540[s]	quasar	
E1511+671	0.31	40.47	1650		NL Sey 1
E1640+537	0.14		970		NL Sey 1
E1657+326	0.09	39.73	570		Sey 1.9
E1805+700	0.19	39.89	1700		NL Sey 1
Non-USS					
E0906+111	0.16	40.17	3780		Sey 1
E1213+378	0.82	40.44	3310		Sey 1
E1228+123	0.12	40.01	1680	Sey 1	NL Sey 1
E1304+342	0.28	40.42	2060	Sey 1	Sey 1
E1654+352	0.80	40.84	3620		QSO

*FWHM of Mg II λ2798 (Hβ out of range). [s]From Stephens (1989). [W]Classification from Wisniewski *et al.* (1986).

NB All Hβ FWHM listed in this Table have been deconvolved from the instrumental profile.

($L_{0.2\,\mathrm{keV}}$) and 2.0 keV ($L_{2\,\mathrm{keV}}$). Note that for the X-ray luminosities, the range has been extended to 0.2 keV, lower than the traditional 0.5 keV, so as to include a significant fraction of the soft-component luminosity (see C92).

5.1 Optical luminosities

The broad-band optical continuum luminosity, L_{opt}, is defined as the luminosity between 3000 and 6000 Å in the AGN rest-frame. The optical continuum flux was measured from the power-law fit to the spectrum where available (for E0436 – 433, the flux was measured directly from the spectrum). To determine the fraction of light lost through the slit, 'magnitudes' determined from the spectra were compared with the accurate CCD magnitudes (see Section 4) when both were available (13 objects) and the spectral flux was scaled up accordingly. These scaling factors are listed in Table 3. On average, the flux measured from the spectrum was 1.8 ± 0.2 times lower than the corresponding CCD flux. Where CCD magnitudes were not available, the average scaling factor was used.

In cases where we do not have spectra, optical luminosities have been determined by converting the V magnitude listed in Table 1 to the flux at 5500 Å using the equations in Allen (1973), then integrating over the appropriate range assuming a power-law index of 1.0 (the average optical index measured in our sample of spectra), having made corrections for the effects of redshift. We have compared luminosities derived using both of these methods for the sources for which we have spectra and find an average difference of 10 per cent.

The rest-frame flux at 2500 Å ($f_{2500\,\mathrm{Å}}$) was measured directly from the spectrum or, when this region was not observed, by extrapolating the optical power-law fit to the continuum and scaling using the factors in Table 3. In the case of objects for which spectra were not available, $f_{2500\,\mathrm{Å}}$ was calculated from colour magnitudes using the equations given in Schmidt (1968; these extrapolate the flux to 2500 Å by assuming an optical power-law index of 0.7 over the range of 1500 to 3700 Å in the rest-frame of the AGN). If more than one observed colour fell within this range, we took the weighted mean value of $f_{2500\,\mathrm{Å}}$.

Table 6. CCD observations of the USS AGN.

Object Name	Date	Telescope	Filter	Exposure Time (s)	Mag[i]	σ_{gal}^{ii} (″)
E1028+310	10 May 89	JKT	R	1800	18.6	<0.4
E1146+558	09 May 89	JKT	R	1800	18.7	0.8
E1213+378	29 Mar 89	INT	R	300	18.3	<0.2
"	"	INT	B	300	19.0	<0.3
E1215+692	29 Mar 89	INT	R	300	19.1	<0.3
"	"	INT	B	300	20.1	<0.4
E1217+695	29 Mar 89	INT	R	150	17.1	<0.2
"	"	INT	B	150	17.5	<0.2
E1218+693	29 Mar 89	INT	R	500	16.9	1.2
"	"	INT	B	500	18.4	1.2
E1228+123	13 May 89	JKT	R	1800	16.8	1.0
E1304+342	29 Mar 89	INT	R	300	17.8	<0.3
"	"	INT	B	300	18.3	<0.2
E1511+671	09 May 89	JKT	R	300	17.9	0.3
"	"	JKT	B	400	18.4	0.3
E1640+537	29 Mar 89	INT	R	300	16.8	0.6
"	"	INT	B	100	18.8	0.9
E1654+352	09 May 89	JKT	R	1000	17.5	<0.2
"	"	JKT	B	1000	17.9	<0.2
E1657+326	29 Mar 89	INT	R	300	17.1	1.2
"	"	INT	B	300	18.5	1.4
E1805+700	29 Mar 89	INT	R	300	17.7	0.8
"	"	INT	B	300	19.2	0.6

[i]Integrated magnitude of the AGN (includes flux from the underlying galaxy). [ii]Gaussian sigma of the AGN in arcsec, σ_{gal}, deconvolved from the seeing profile. Upper limits are given where the AGN profile is point-like.

5.2 X-ray luminosities

Separate hard and soft X-ray component luminosities have been calculated for the USS AGN. The spectral fitting procedure and X-ray luminosity calculations are detailed in C92, but a brief description is given here for completeness. The IPC count distributions (see C92) show that many spectra have a hard component in addition to the soft excess, therefore a 'mean' two-component model spectrum was fitted to all of the IPC spectra simultaneously. The hard component was represented by a power law whose index was fixed at the canonical value of 0.7 (Mushotzky 1984; Turner & Pounds 1989), while blackbody spectra were fitted to the soft component. Mean blackbody temperatures were tried in the observer frame and the rest-frame. The absorbing column in front of each source, N_H, was fixed at the value taken from Stark *et al.* (1984). A best fit was obtained for a blackbody temperature, kT_{eff}, of ~10 eV in the rest-frame for the low-redshift, $z<0.5$, AGN.

Hard- and soft-component X-ray luminosities, L_{soft} and L_{hard}, are calculated over the 0.2–4.5-keV range in the rest-frame. L_{soft} was not calculated for objects at $z>0.5$ because the soft-component spectra could not be extrapolated reliably below a *rest-frame* energy corresponding to the lower energy limit of the *observed* spectra, i.e. 0.16 keV (see C92). The X-ray luminosities for three objects, E0150−102, E1218+693 and E1644−029, are not listed because they were not satisfactorily fitted by the model. L_{soft} and L_{hard} were calculated for two different mean soft-component spectra; one where the soft blackbody kT_{eff} is fixed at 10 eV in the *rest-frame* of the AGN, and another where kT_{eff} is fixed at 7.85 eV in the *observer* frame [the mean redshift of the low-redshift secure AGN ($z<0.5$) is $\bar{z}=0.27$: a rest-frame kT_{eff} of 10 eV for an AGN at this redshift corresponds to a kT_{eff} of ~7.85 eV in the observer's frame]. In both cases, the hard-component index was fixed at 0.7. Table 7 lists L_{soft} for both of these models while the value for L_{hard} corresponds to the observer-frame kT_{eff} of 7.85 eV (when calculated for a rest-frame $kT_{eff}=10$ eV, L_{hard} differed on average by ~2 per cent from the observer-frame value). The monochromatic X-ray luminosities listed in Table 7, $L_{0.2\,keV}$ and $L_{2\,keV}$, were calculated from the $kT_{eff}=7.85$ eV observer-frame model and correspond to measurements for the separate soft and hard components respectively.

6 E0132−411

Before going on to the analysis of the survey as a whole, we take a closer look at one particular secure USS AGN, E0132−411. This object ($z=0.267$) was independently identified by Kriss (1982) and was also discussed by Córdova & Kartje (1989). It was contained within a deep *Einstein* IPC field (effective exposure time 28.5×10^3 s). Consequently, though it is not an intrinsically bright source (IPC count rate 0.01 count s^{-1}), the X-ray spectral data on this object have good statistical quality. It exhibits a soft overall X-ray spectral distribution with little evidence of a hard spectral component. X-ray spectral fits using all of the *Einstein* IPC PHA channels may be found in C92. E0132−411 is also relatively bright optically ($V=17.4$). We therefore made a particular effort to obtain an accurately flux-calibrated optical spectrum of this AGN in order to investigate its multiwavelength spectral distribution. We also observed it with *IUE* as described in Section 6.2.

6.1 Optical spectrum

The optical continuum of E0132−411 rises towards the blue and is fitted with a power-law index = 0.8 (in F_ν). The Balmer lines are strong and relatively narrow (FWHM Hβ = 2080 km s^{-1}) and are visible down to Hε. Forbidden lines of [O II], [O III], [Ne III] and [Ne V] are also seen but [O I] and [S II] are weak. Perhaps the most striking feature is the presence of strong red and blue optical Fe II blends. Fe II emission between 4500 and 4680 Å is particularly strong; it extends blueward beyond Hγ and blends with another Fe II feature which lies beneath Hβ and [O III]$\lambda\lambda$4959, 5007. At a value of 1.7, E0132−411 has the highest ratio of blue to red Fe II flux of the sources listed in Table 4.

6.2 UV spectrum

We have made two observations of E0132−411 in the ultraviolet using the short-wavelength camera (SWP) on the *International Ultraviolet Explorer* satellite (*IUE*). The first was taken on 1990 January 3 at the Villafranca Tracking Station (VILSPA) and the second on the night of 1990 June 4 at the NASA Goddard Space Flight Center. Both were taken in low-resolution mode and covered the range of 1150 to 1980 Å with a resolution of 5–8 Å pixel^{-1}. The two weighted spectra have been added together and the result is shown in Fig. 4.

The UV spectrum shows strong Lyα emission at 1216 Å ($F\sim2\times10^{-13}$ erg cm^{-2} s^{-1}) and possibly Lyβ at 1026 Å ($F\sim2\times10^{-14}$ erg cm^{-2} s^{-1}). The continuum flux at 1200 Å (in the rest-frame) was $\sim3\times10^{-15}$ erg cm^{-2} s^{-1} Å^{-1} and the rest-frame continuum between 1000 and 1500 Å was best

Table 7. USS AGN luminosity table.

Object	L^1_{soft} (1)	L^2_{soft} (2)	L_{hard} (3)	L_{opt} (4)	$L_{0.2keV}$ (5)	L_{2keV} (6)	L_{2500A} (7)	α_{os} (8)	α_{ox} (9)	α_{sx} (10)	z (11)	N_H (12)
E0111–015	44.03	43.93	<43.37	43.83	28.45	<25.27	28.22	–0.14	>1.12	>3.18	0.12	3.67
E0114–016	46.58	46.49	44.19	44.13	30.99	26.09	29.27	–1.07	1.21	4.90	0.38	4.30
E0131–408			45.94	45.25		27.84	30.19		0.89		2.36	2.11
E0132–411	44.48	44.48	43.37	44.50	29.00	25.27	29.59	0.36	1.65	3.72	0.27	2.14
E0136–250	43.99	44.03	44.46	44.54	28.54	26.36	29.69	0.71	1.27	2.17	0.31	1.20
E0310–557	44.09	44.04	44.58	44.62	28.56	26.48	29.78	0.75	1.26	2.08	0.23	1.80
E0331–365	44.64	44.67	<44.35	44.46	29.19	<26.26	29.62	0.26	>1.28	>2.92	0.31	1.40
E0845+376	45.90	45.90	44.13	44.45	30.41	26.03	29.88	–0.33	1.47	4.37	0.31	3.36
E0944+464	44.47	44.54	<44.23	44.32	29.05	<26.13	29.40	0.21	>1.25	>2.91	0.35	1.30
E0957+561			<45.95	46.23		<27.85	31.40		>1.35		1.41	1.28
E1028+310	43.90	43.88	*43.29	43.92	28.39	*25.27	28.57	0.10	*1.26	*3.12	0.25	1.86
E1040+123			<45.75	45.65		27.69	31.43		1.43		1.03	2.70
E1146+558	44.97	45.04	<44.28	44.17	29.55	<26.19	29.24	–0.19	>1.17	>3.36	0.44	1.30
E1208+322	45.56	45.59	44.93	45.45	30.10	26.84	30.28	0.10	1.31	3.26	0.39	1.87
E1227+140	42.52	42.25	43.45	43.70	26.77	25.36	28.65	1.16	1.26	1.41	0.10	2.11
E1251–005	45.14	45.19	<43.88	44.53	29.70	<25.79	29.67	–1.99	>1.48	>3.90	0.43	1.60
E1254+221	43.89	43.82	43.69	44.48	28.34	25.59	29.64	0.80	1.55	2.75	0.19	2.60
E1255+220	44.74	44.74	<43.15	44.12	29.25	<25.06	29.29	1.93	>1.62	>4.19	0.26	2.60
E1255+017	43.00	42.84	43.49	43.77	27.36	25.39	28.94	0.98	1.36	1.96	0.16	1.70
E1334+038	42.44	42.24	43.43	43.92	26.76	25.33	29.09	1.44	1.44	1.42	0.13	2.00
E1346+266			<45.04	44.97		<26.94	30.54		>1.38		0.92	1.43
E1401+098	45.88	45.88	45.26	45.46	30.38	27.16	30.74	0.22	1.37	3.21	0.44	1.98
E1423+201	44.90	44.85	<43.79	44.96	29.37	<25.69	30.29	0.57	>1.76	>3.67	0.21	2.54
E1425+169	43.66	43.61	*43.58	43.73	28.12	*25.49	28.81	0.42	*1.27	*2.63	0.22	1.75
E1519+279	44.87	44.85	<43.34	44.15	29.37	<25.24	29.81	0.27	>1.75	>4.12	0.23	2.69
E1614+308	44.08	44.08	43.99	44.36	28.59	25.89	29.51	0.56	1.38	2.70	0.27	2.40
E1704+608	45.35	45.36	44.74	45.69	29.86	26.65	30.89	0.63	1.62	3.21	0.37	2.26
E2034–220	45.71	45.71	44.33	44.40	30.22	26.24	29.56	–0.41	1.27	3.98	0.26	3.80
E2318–423	43.83	43.77	43.82	44.09	28.28	25.72	29.71	0.88	1.52	2.56	0.21	1.98
E0007–357	41.79	41.38	43.22	44.29	25.91	25.12	29.47	2.21	1.66	0.78	0.09	1.20
E0039–019	46.80	46.76	<44.20	45.34	31.27	<26.10	30.46	–0.50	>1.67	>5.16	0.35	3.91
E0114–002	42.17	41.89	*42.09	43.38	26.42	*23.99	28.34	1.19	*1.66	*2.42	0.04	3.53
E0129–066	44.65	44.62	<44.39	44.58	29.14	<26.29	29.81	0.41	>1.34	>2.84	0.22	2.50
E0141+020	41.31	40.89	41.73	43.58	25.42	23.64	28.77	2.08	1.96	1.78	0.02	3.00
E0200–089			<44.98	45.75		<26.88	31.21		>1.65		0.77	2.10
E0337–267	42.38	42.03	<43.16	43.53	26.91	<25.06	28.39	0.91	>1.27	>1.85	0.11	1.16
E0436–433	42.66	42.35	<43.00	43.91	25.96	<24.90	28.64	1.66	>1.43	>1.05	0.07	2.53
E0844+377	47.22	47.05	44.66	44.96	29.86	26.57	30.39	0.32	1.46	3.29	0.45	3.61
E0952+442	44.57	44.64	45.10	45.08	29.67	27.01	30.31	0.39	1.26	2.66	0.47	1.16
E1008+348	44.13	43.98	44.08	44.01	27.58	25.99	29.18	0.99	1.22	1.58	0.14	2.50
E1011+496	43.79	43.65	<43.26	44.86	28.94	<25.16	29.92	0.60	>1.82	>3.77	0.20	0.83
E1059+730	43.77	43.64	<43.29	44.13	26.15	<25.20	28.92	1.72	>1.42	>0.95	0.08	4.03
E1215+692			<44.82	44.53		<26.73	30.01		>1.25		1.12	1.59
E1217+695			<45.06	45.10		<26.96	31.04		>1.56		0.63	1.60
E1352+183	44.23	44.05	44.16	44.89	28.57	26.07	29.24	0.41	1.21	2.50	0.15	1.84
E1423+242			<45.32	45.35		<27.22	30.69		>1.33		0.65	2.70
E1511+671	45.40	45.40	<43.54	44.59	29.92	<25.45	29.83	–0.05	>1.68	>4.46	0.31	2.73
E1640+537	43.89	43.75	<43.79	43.95	28.27	<25.69	28.90	0.38	>1.22	>2.58	0.14	2.54
E1657+326	41.98	41.73	43.16	43.47	26.26	25.06	28.55	1.42	1.33	1.20	0.09	2.42
E1805+700	45.70	45.73	<44.20	43.84	30.25	<26.10	28.74	–0.94	>1.01	>4.15	0.19	5.68
E0906+111	45.90	45.88	<44.52	44.10	30.40	<26.42	29.17	–0.76	>1.05	>3.98	0.16	4.37
E1213+378			<45.24	44.79		<27.14	30.07		>1.12	1.50	0.82	
E1227+140	43.03	42.77	<43.42	43.69	27.30	<25.32	28.65	0.84	>1.27	>1.97	0.10	2.29
E1228+123	43.30	43.04	<44.33	43.93	27.57	<26.23	28.90	0.82	>1.02	>1.33	0.12	1.70
E1304+342	43.79	43.80	<44.00	44.62	28.31	<25.91	29.74	0.88	>1.46	>2.40	0.28	1.02
E1654+352			<44.63	45.18		<26.54	31.25		>1.80		0.80	2.28

(1) Log_{10} of the soft X-ray component luminosity integrated over 0.2–4.5 keV for a blackbody with a rest-frame $T_{eff}=10$ eV, in erg s^{-1} (see Section 5.2). (2) Log_{10} of the soft X-ray component luminosity integrated over 0.2–4.5 keV for a blackbody with an observer-frame $T_{eff}=7.85$ eV, in erg s^{-1} (see Section 5.2). (3) Log_{10} of the hard X-ray component luminosity integrated over 0.2–4.5 keV for a power law with index = 0.7 corresponding to the 7.85-eV observer-frame model, in erg s^{-1} (see Section 5.2). (4) Log_{10} of the optical continuum luminosity integrated over 3000–6000 Å in erg s^{-1} (see Section 5.1). (5) Log_{10} of the soft X-ray component luminosity at 0.2 keV corresponding to the 7.85-eV observer-frame model, in erg s^{-1} Hz^{-1} (see Section 5.2). (6) Log_{10} of the hard X-ray component luminosity at 2 keV corresponding to the 7.85-eV observer-frame model, in erg s^{-1} Hz^{-1} (see Section 5.2). (7) Log_{10} of the optical continuum luminosity at 2500 Å in erg s^{-1} Hz^{-1} (see Section 5.1). (8) Ratio of optical to soft X-ray component luminosities (see Section 7.3) corresponding to the 7.85-eV observer-frame model. (9) Ratio of optical to hard X-ray component luminosities (see Section 7.3) corresponding to the 7.85-eV observer-frame model. (10) Ratio of soft to hard X-ray component luminosities (see Section 7.3) corresponding to the 7.85-eV observer-frame model. (11) Redshift. (12) Absorbing column in units of 10^{20} cm^{-2} taken from Stark *et al.* (1984).

*X-ray spectrum poorly fitted by the model.

fitted using a power law with an index of 0.7 (*cf.* 0.8 in the optical).

6.3 Multiwavelength spectrum

The optical and ultraviolet spectra of E0132 − 411 are combined with the X-ray data in Fig. 5 where we plot log νF_ν versus log ν. The X-ray count rates have been converted from counts per second to flux using the two-component spectral model that has a blackbody temperature of 10 eV (in the rest-frame of the AGN) and a hard power-law index of 0.7. This model is plotted as a thick solid line in Fig. 5. Fitted models with blackbody temperatures of 15, 25, 50 and 100 eV are also shown for comparison, plotted as thin solid lines. Note that as the blackbody temperature increases, the normalization of the hard X-ray power law decreases. Thus the 10-eV model fit provides a reasonable upper limit to the flux in the hard X-ray spectrum.

We have compared the spectral distribution of E0132 − 411 with that of the Seyfert galaxy Mkn 841 ($z = 0.037$), using data taken from Arnaud *et al.* (1985). The spectrum of Mkn 841 has been redshifted to the same distance and normalized to the optical spectrum of E0132 − 411. The relative distribution of flux between the optical, ultraviolet and soft X-ray bands is very similar in the two objects. The major difference between them is that the hard X-ray component in E0132 − 411 is depressed by more than an order of magnitude relative to Mkn 841.

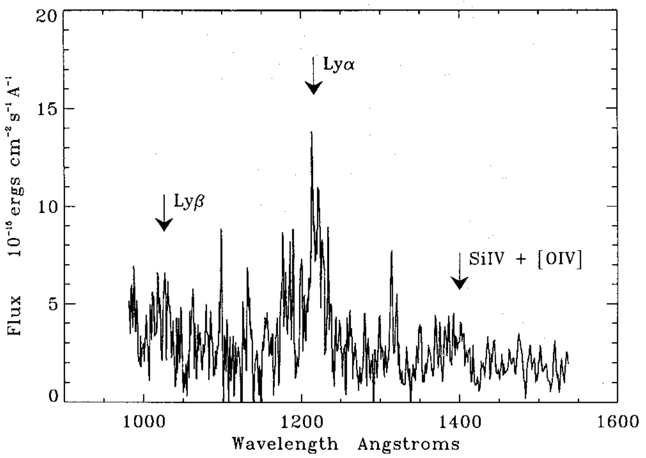

Figure 4. The UV spectrum of E0132 − 411. This spectrum is derived from the weighted sum of two exposures taken with *IUE*. The spectrum is plotted in the rest-frame of the AGN. No correction for redshift has been made to the flux. The expected positions of Lyα, Lyβ and the Si IV/[O IV] blend are indicated.

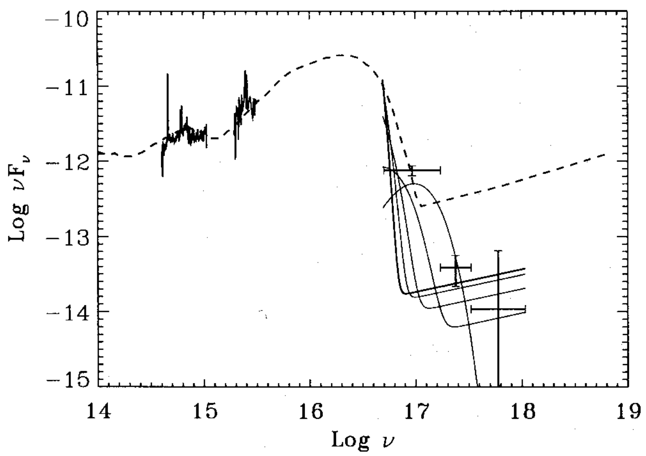

Figure 5. The multiwavelength spectrum of E0132 − 411. Plotted as solid lines are the optical spectrum taken at the AAT (also shown in Fig. 3) and the UV spectrum taken with *IUE* (also shown in Fig. 4). The X-ray spectrum is represented by a two-component model, a soft blackbody with $T_{eff} = 10$ eV in the rest-frame of the AGN and a hard power law with an index of 0.7, and is plotted as a thick solid line. Also plotted as thin lines are fitted models with rest-frame T_{eff} of 15, 25, 50 and 100 eV (see Section 6.3). The three X-ray data points represent the counts detected in the *C1, C2* and *C3* bands, and were calculated using conversion factors from counts to flux derived from the 10-eV two-component fit. The multiwavelength spectrum of the Seyfert galaxy Mkn 841 (from Arnaud *et al.* 1985) is plotted as a dashed line for comparison.

7 ANALYSIS

This section examines more closely the X-ray and optical properties of the USS AGN. To search for relationships between the various line and continuum parameters, we have computed linear correlation coefficients for each parameter pair in turn and these are summarized in Table 8. Correlations between the continuum parameters of the secure sources are given in Table 8(a). Line and continuum correlations, for those secure and non-secure sources for which we have spectra, are given in Table 8(b). Only measured values were used in the correlations, although upper limits may be included in associated plots. No correlation coefficient is given in Table 8 if the number of available data pairs (given in parentheses) was less than five.

7.1 Redshift

The redshift distribution of the secure USS AGN is shown in Fig. 6, together with the distributions for the EMSS and HGLS surveys. There are no secure USS sources with a redshift of less than 0.1, four out of 29 sources have $z \geq 0.92$ and the remaining secure USS AGN are distributed evenly over the 0.1 to 0.5 range. In contrast, the EMSS AGN distribution shows a strong peak between 0.05 and 0.20 while the HGLS peaks at the lowest redshifts ($z < 0.1$). Applying the Kolmogorov–Smirnov test to the distributions yields a probability of 4 per cent that the EMSS and secure USS AGN are drawn from the same parent population, and a corresponding probability for the HGLS and secure USS of less than 1 per cent.

The apparent cut-off at $z = 0.5$ for the secure USS AGN may indicate that there is an upper limit to the 'temperature' of the soft component which is moved out of the IPC bandpass at higher redshifts. This was previously suggested by Wilkes *et al.* (1989) who also saw this cut-off in their sample. The lack of secure USS AGN at $z < 0.1$ is curious; soft X-ray excesses have been discovered in very low-redshift ($z < 0.1$) AGN of other *Einstein* samples (e.g. Urry *et al.* 1989, Wilkes *et al.* 1989), and six (out of 24) of the *non-secure* USS AGN lie below this redshift. Confirmation of this restricted range (i.e. $z = 0.1$–0.5) for the steepest soft X-ray spectra in a larger sample of higher data quality would have important conse-

Table 8. (a) X-ray and optical continuum correlations for the secure USS AGN.

	L^1_{soft}	L^2_{soft}	L_{hard}	L_{opt}	$L_{0.2keV}$	L_{2keV}	L_{2500A}	z	N_H	α_{os}	α_{oz}
L^2_{soft}	1.0(25)										
L_{hard}	0.7(17)	0.7(17)									
L_{opt}	0.6(25)	0.6(25)	0.8(18)								
$L_{0.2keV}$	1.0(25)	1.0(25)	0.7(17)	0.6(25)							
L_{2keV}	0.7(17)	0.7(17)	1.0(18)	0.9(19)	0.7(17)						
L_{2500A}	0.6(25)	0.6(25)	0.8(18)	0.9(29)	0.6(25)	0.8(19)					
z	0.8(25)	0.8(25)	0.7(18)	0.6(29)	0.8(25)	0.7(19)	0.5(29)				
N_H	0.4(25)	0.4(25)	0.0(18)	−0.2(29)	0.4(25)	0.1(19)	−0.2(29)	−0.2(29)			
α_{os}	−0.6(25)	−0.6(25)	−0.3(17)	−0.1(25)	−0.6(25)	−0.3(17)	−0.1(25)	−0.6(25)	−0.2(25)		
α_{oz}	0.0(17)	0.0(17)	−0.5(18)	0.1(19)	0.0(17)	−0.4(19)	0.2(19)	−0.6(19)	0.0(19)	0.3(17)	
α_{sz}	0.9(17)	0.9(17)	0.3(17)	0.3(17)	0.9(17)	0.3(17)	0.3(17)	0.7(17)	0.8(17)	−0.9(17)	0.1(17)

Linear correlation coefficient (number of data pairs)

Table 8. (b) Optical line and continuum correlations (secure and non-secure).

Line luminosity

	L^1_{soft}	L^2_{soft}	L_{hard}	L_{opt}	$L_{0.2keV}$	L_{2keV}	L_{2500A}	z	α_{os}	α_{oz}	α_{sz}	α_{opt}	MgII	H_β	[OIII]	HeI
α_{opt}	−0.9(14)	−0.9(14)	−0.8(7)	−0.9(18)	−0.8(14)	−0.8(7)	−0.9(18)	−0.6(18)	0.6(14)	−0.3(7)	−0.7(7)					
MgII	0.8(5)	0.8(5)	(1)	0.3(8)	0.4(5)	(1)	0.4(8)	0.3(8)	0.0(5)	(1)	(1)	−0.5(8)				
H_β	0.9(14)	0.9(14)	0.8(7)	0.9(17)	0.8(14)	0.8(7)	0.9(17)	0.6(17)	−0.6(14)	0.3(7)	0.8(7)	−0.9(17)	0.5(7)			
[OIII]	0.9(15)	0.9(15)	0.8(7)	0.8(17)	0.8(15)	0.8(7)	0.8(17)	0.7(17)	−0.6(15)	0.1(7)	0.7(7)	−0.8(16)	0.4(6)	0.9(16)		
HeI	0.9(10)	0.9(10)	(4)	0.9(10)	0.8(10)	(4)	1.0(10)	0.6(10)	−0.4(10)	(4)	(4)	−1.0(10)	(4)	1.0(10)	0.8(10)	
H_α	0.9(15)	0.9(15)	0.8(7)	0.9(16)	0.9(15)	0.8(7)	1.0(16)	0.8(16)	−0.7(15)	0.2(7)	0.7(7)	−1.0(15)	0.7(5)	1.0(15)	0.9(16)	1.0(10)

Line FWHM

	L^1_{soft}	L^2_{soft}	L_{hard}	L_{opt}	$L_{0.2keV}$	L_{2keV}	L_{2500A}	z	α_{os}	α_{oz}	α_{sz}	α_{opt}	MgII	H_β	[OIII]	HeI
MgII	0.1(5)	0.1(5)	(1)	−0.2(8)	−0.2(5)	(1)	0.1(8)	0.8(8)	0.2(5)	(1)	(1)	−0.1(8)				
H_β	−0.1(14)	−0.1(14)	−0.1(7)	0.2(17)	−0.1(14)	−0.1(7)	0.3(17)	0.2(17)	0.2(14)	0.1(7)	0.0(7)	−0.3(17)	0.6(7)			
[OIII]	0.6(15)	0.6(15)	0.3(7)	0.7(17)	0.7(15)	0.3(7)	0.7(17)	0.5(17)	−0.7(15)	0.2(7)	0.4(7)	−0.5(16)	−0.1(6)	0.1(16)		
HeI	0.0(10)	0.0(10)	(4)	0.0(10)	−0.1(10)	(4)	0.1(10)	0.1(10)	0.2(10)	(4)	(4)	−0.2(10)	(4)	0.5(10)	0.0(10)	
H_α	−0.4(15)	−0.4(15)	0.0(7)	−0.4(16)	−0.5(15)	0.0(7)	−0.4(16)	−0.3(16)	0.4(15)	−0.7(7)	−0.7(7)	0.2(15)	0.4(5)	0.7(15)	−0.5(16)	0.2(10)

Line EW

	L^1_{soft}	L^2_{soft}	L_{hard}	L_{opt}	$L_{0.2keV}$	L_{2keV}	L_{2500A}	z	α_{os}	α_{oz}	α_{sz}	α_{opt}	MgII	H_β	[OIII]	HeI
MgII	−0.1(5)	−0.1(5)	(1)	−0.6(8)	−0.3(5)	(1)	−0.5(8)	0.1(8)	0.0(5)	(1)	(1)	0.5(8)				
H_β	0.8(14)	0.8(14)	0.8(7)	0.6(17)	0.6(14)	0.8(7)	0.5(17)	0.3(17)	−0.5(14)	0.1(7)	0.7(7)	−0.6(16)	−0.1(6)			
[OIII]	0.5(15)	0.5(15)	0.8(7)	0.2(17)	0.3(15)	0.8(7)	0.2(17)	0.3(17)	−0.2(15)	0.0(7)	0.6(7)	−0.3(16)	0.0(6)	0.8(16)		
HeI	0.7(11)	0.7(11)	(4)	0.5(11)	0.4(11)	(4)	0.6(11)	0.6(11)	−0.2(11)	(4)	(4)	−0.6(10)	(4)	0.9(10)	0.7(11)	
H_α	0.7(15)	0.7(15)	0.9(7)	0.6(16)	0.6(15)	0.9(7)	0.7(16)	0.7(16)	−0.5(15)	0.0(7)	0.6(7)	−0.8(15)	−0.1(5)	0.9(15)	0.7(16)	0.9(11)

FeII parameters

	L^1_{soft}	L^2_{soft}	L_{hard}	L_{opt}	$L_{0.2keV}$	L_{2keV}	L_{2500A}	z	α_{os}	α_{oz}	α_{sz}	α_{opt}	L_{blue}	L_{red}	B/R	L_{blue}/H_β	L_{red}/H_β
L_{blue}	0.9(11)	0.9(11)	0.6(5)	1.0(13)	0.9(11)	0.6(5)	0.9(13)	0.6(13)	−0.8(11)	0.8(5)	0.9(5)	−0.9(13)					
L_{red}	0.8(9)	0.8(9)	(4)	0.9(10)	0.9(9)	(4)	1.0(10)	0.7(10)	−0.7(9)	(4)	(4)	−0.8(10)	1.0(10)				
B/R	0.0(9)	0.0(9)	(4)	−0.1(10)	0.2(9)	(4)	−0.2(10)	−0.3(10)	−0.3(9)	(4)	(4)	0.0(10)	0.1(10)	−0.2(10)			
L_{blue}/H_β	−0.6(11)	−0.6(11)	−0.7(5)	−0.4(13)	−0.5(11)	−0.7(5)	−0.4(13)	−0.3(13)	0.5(11)	−0.3(5)	−0.8(5)	0.5(13)	−0.3(13)	−0.1(10)	−0.3(10)		
L_{red}/H_β	−0.6(9)	−0.6(9)	(4)	−0.2(10)	−0.5(9)	(4)	−0.1(10)	0.0(10)	0.5(9)	(4)	(4)	0.4(10)	−0.2(10)	0.0(10)	−0.6(10)	0.9(10)	
EW(B)	0.0(11)	0.1(11)	−0.3(5)	0.1(13)	0.1(11)	−0.3(5)	0.2(13)	0.0(13)	−0.1(11)	0.6(5)	0.5(5)	−0.2(13)	0.4(13)	0.4(10)	0.5(10)	0.1(13)	−0.1(10)
EW(R)	0.3(9)	0.3(9)	(4)	0.4(10)	0.3(9)	(4)	0.6(10)	0.7(10)	−0.2(9)	(4)	(4)	−0.4(10)	0.5(10)	0.7(10)	−0.4(10)	0.1(10)	0.4(10)

Linear correlation coefficient (number of data pairs)

quences for constraining spectral models of the soft X-ray emission.

We assume that a common mechanism produces the soft X-ray excess in all the low-redshift ($z<0.5$) AGN. The four secure USS AGN with $z>0.5$ are E0131 − 408, a faint QSO ($z=2.36$); E0957 + 561, the double quasar ($z=1.41$); E1040 + 123, a superluminal radio source at a redshift of 1.03, and E1346 + 266, a new USS identification ($z=0.92$) which also appears in the HGLS. The unusual nature of the high-redshift sources suggests that different mechanisms may be responsible for their observed soft X-ray excesses (see the Appendix and C92 for more information).

7.2 Luminosities

We have investigated the USS X-ray and optical luminosity distributions by comparing them with two other large, X-ray selected surveys, the *Einstein* EMSS and the *EXOSAT* HGLS. The EMSS sources are selected from the 0.2- to 3.5-keV band data of the *Einstein* IPC detector while the *EXOSAT* CMA detector used for the HGLS was sensitive between 0.05 and 2.0 keV (unlike the *Einstein* IPC, the *EXOSAT* CMA detector had no intrinsic spectral resolution). We have converted HGLS counts to fluxes using the conversion graph in Giommi *et al.* (1991), assuming a power-law energy index of 1.5 (which was the best fit inferred for the *EXOSAT* sample; Giommi *et al.* 1991) and the N_H listed in the HGLS. The EMSS fluxes used have been taken from Stocke *et al.* (1991) and were converted from count rates assuming an energy index of 1.0.

7.2.1 *Soft X-ray luminosities*

The Ultra-Soft Survey was originally designed to select hot, isolated neutron stars by searching for a steep slope in the lowest energy channels of the *Einstein* IPC PHA distribution, as evidence for the high-energy tail of a ~ 10-eV blackbody. The discovery of so many AGN in the USS sample was an

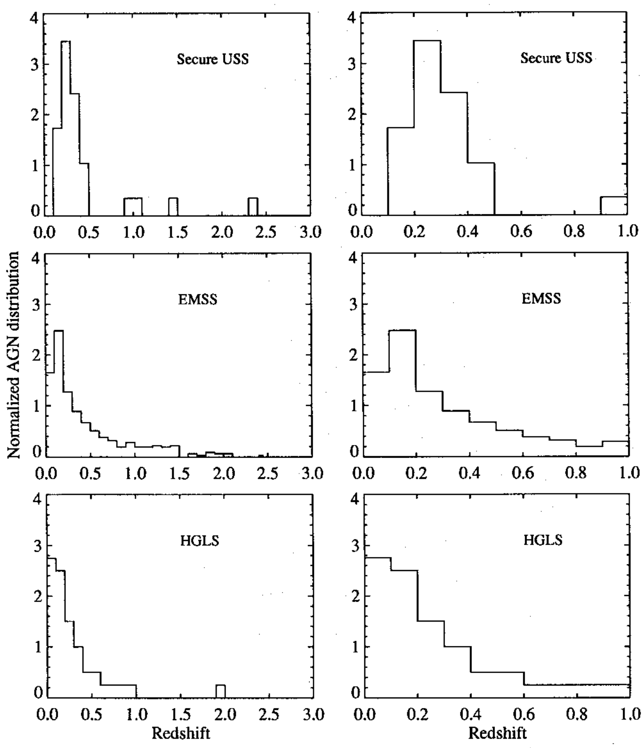

Figure 6. The redshift distribution of the secure USS AGN compared with AGN from the *Einstein* EMSS and the *EXOSAT* HGLS. These are plotted over the full range of redshifts and also between 0 and 1 to highlight the differences at the lowest redshifts.

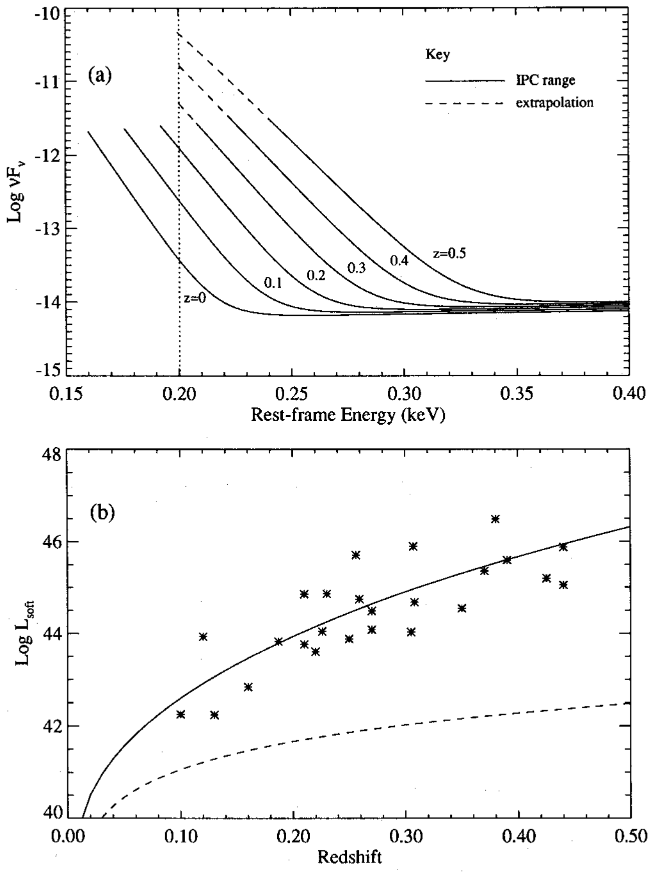

Figure 7. (a) The spectra of six hypothetical USS AGN, which have identical *observed* spectra but different redshifts (from 0.0 to 0.5), plotted as they would appear in the *rest-frame* of the AGN. The redshift of each AGN is indicated on the diagram. The spectra shift towards higher energies as the redshift increases. The dotted line shows the lower limit of the range over which we have calculated the X-ray luminosities (i.e. 0.2 keV). The solid lines cover the *observed* range of the IPC and the dashed lines indicate the extrapolated portion of the fit. (b) The redshift dependence of the soft X-ray component luminosity. The solid line represents the simulated soft-component luminosity distribution for a typical USS-type spectrum observed at redshifts from 0 to 0.5. Measured values of $L_{\rm soft}$ for the secure sources are plotted as asterisks. The dashed line represents a simulated distribution for a perfectly flat spectrum so that there is no redshift dependence in the luminosity, other than the cosmological distance dependence.

interesting and unexpected surprise, but assembling a sample of AGN on the basis of their *observed* soft X-ray spectra has introduced a strong redshift selection effect. We compare the AGN soft- and hard-component luminosities over an energy range which is defined in the rest-frame. The observed portion of the steep soft component is rapidly shifted through this energy range as the redshift of the AGN increases. This is illustrated in Fig. 7(a) where a typical observed USS-type spectrum is represented by a soft blackbody component with a $T_{\rm eff}$ of 7.85 eV and a hard power-law component with an index of 0.7 (Section 5.2).

Fig. 7(a) illustrates how a 'typical' USS AGN spectrum *registered in the observer frame* appears in the *rest-frame* at different redshifts, with the spectrum shifting to higher energies as the redshift increases. Plotted as a solid line in Fig. 7(b) is a simulated soft luminosity distribution (integrated over the 0.2- to 4.5-keV range in the AGN rest-frame), calculated for this 'typical' observed spectrum at different assumed redshifts. The dashed line illustrates the distribution expected for a perfectly flat spectrum, so that there is no dependence on redshift in the luminosity other than the cosmological distance dependence. The actual soft luminosities for the secure USS sources are also plotted for comparison with the models. This emphasizes that the steepness of the soft-component spectrum exacerbates the selection in favour of higher luminosity sources at the higher redshifts.

It is thus clear from Fig. 7 that by selecting a sample of objects at different redshifts on the basis of their *observed* spectral shape, we have introduced a strong redshift dependence into the soft-component luminosity because it is measured over a restricted band. We are unable to quantify the luminosity of the soft component as a whole, without data which reach further into the 'big blue bump' from the UV and the soft X-ray regions. The blackbody parameters which we have derived from modelling the X-ray data are applicable only within the 0.16- to 3.5-keV range; because it is so steep, the model soon becomes unreliable if we extrapolate longwards into the EUV. So when looking for the possible dependence of other parameters on the soft luminosity parameters (e.g. $L_{\rm soft}$, $L_{0.2\,\rm keV}$ and $\alpha_{\rm os}$), this very strong redshift dependence must be borne in mind.

7.2.2 *Hard X-ray luminosities*

The hard-component X-ray luminosity from 0.2 to 4.5 keV, $L_{\rm hard}$ (see Section 7.2), is plotted in Fig. 8(a) as a function of redshift, with the X-ray luminosities of the EMSS and HGLS

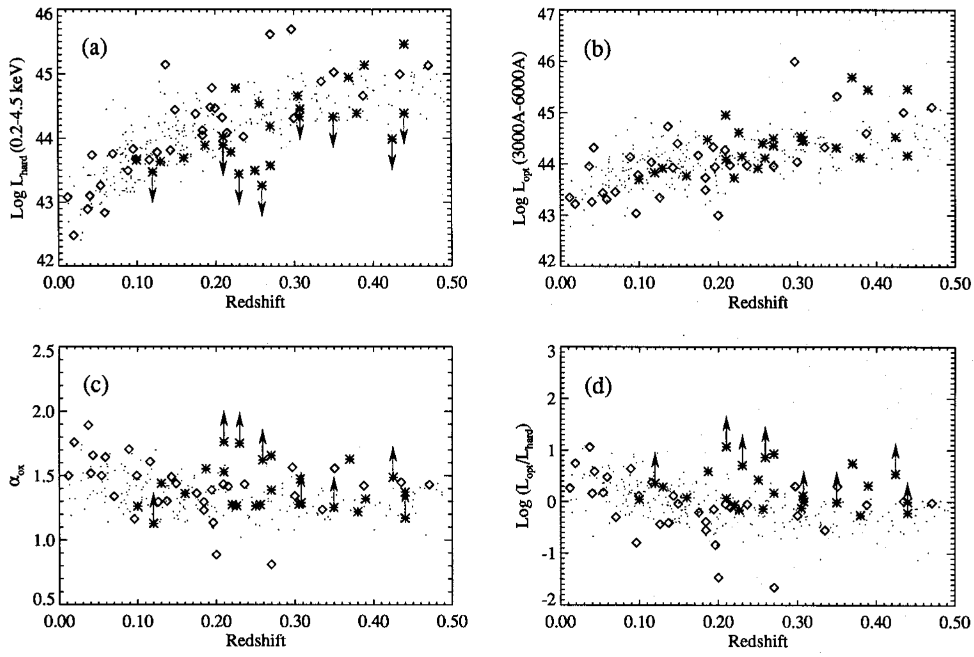

Figure 8. (a) The hard-component X-ray luminosity from 0.2 to 4.5 keV, plotted as a function of redshift, for the low-redshift ($z<0.5$) secure USS AGN (asterisks). The 'total' X-ray luminosities of the EMSS (dots; see Section 7.2.2), and the HGLS (diamonds) over the same range, are plotted for comparison. (b) Optical luminosities of the secure USS AGN (asterisks) plotted as a function of redshift for the low-redshift ($z<0.5$) AGN. Corresponding luminosities are plotted for the EMSS (dots) and the HGLS (diamonds). All luminosities are calculated over the 3000- to 6000-Å range from V magnitudes (see Section 7.2.3). (c) The ratio of monochromatic optical to hard X-ray luminosities, α_{ox}, plotted as a function of redshift for the low-redshift ($z<0.5$) secure USS AGN (asterisks; see Section 7.3 for the definition of α_{ox}). Also plotted is the distribution of α_{ox} for the EMSS (dots) and the HGLS (diamonds). (d) The ratio of broad-band optical to hard X-ray luminosity (shown separately in Fig. 8a and b) for the secure low-redshift ($z<0.5$) USS AGN (asterisks), plotted as a function of redshift. The ratio of broad-band optical to 'total' X-ray luminosity is plotted for the EMSS (dots) and HGLS (diamonds) for comparison.

AGN included for comparison. These are plotted over the redshift range of 0.0 to 0.5, where most AGN in all three surveys lie (see Fig. 6 and Section 7.1). The hard-component luminosities of the USS AGN are on average lower than the X-ray luminosities of the EMSS AGN. The HGLS X-ray luminosities are generally consistent with those of the EMSS.

Fig. 8(a) shows that about one third of the USS AGN have a value for L_{hard} that is significantly lower than the band defined by the X-ray luminosity distribution of the EMSS (note that there are 11 secure USS sources where we have only upper limits on the hard-component flux). Other USS AGN have an L_{hard} that is comparable to the EMSS X-ray luminosity distribution (although generally lower than the average for the EMSS), indicating that for these objects the soft component is superposed on a 'normal' underlying hard X-ray power law.

Note that the 'hard'-component luminosities of the EMSS and HGLS sources will include any photons from a soft component, if present, since multiple spectral components were not differentiated in those studies. Thus if any of the EMSS or HGLS sources have significant soft-component emission, their hard-component luminosities will be overestimated in Fig. 8(a). As an illustration of this, if we calculate luminosities for the USS sources on the basis of a single hard power-law fit to the *Einstein* spectra, we obtain values that are consistent with those in the EMSS, as expected since both are derived from the same count-limited sample. However, we presume that any contribution from the soft component is relatively small in the majority of the EMSS sources, since only a small fraction of *Einstein* AGN appear in the USS sample. By inference, the same is true of the HGLS since the relative numbers of EMSS and USS AGN suggest that the incidence of observable strong soft X-ray emitting components among X-ray emitting AGN is relatively low when they are selected without spectral discrimination.

7.2.3 *Optical luminosities*

We have calculated the optical luminosities in the range 3000–6000 Å for the EMSS and HGLS AGN from the V magnitudes, assuming an optical power-law index of 1.0. We have recalculated the USS optical luminosities in the same way in order to make a comparison. The results are shown in Fig. 8(b) for $z<0.5$ and demonstrate that most of the USS optical luminosities are typical of other X-ray selected AGN (the only notable exception being E1704+608 which is known to be variable).

7.3 X-ray to optical luminosity ratio: determining α_{ox}

Strong correlations between X-ray and optical luminosity have been reported by previous authors in both X-ray selected (e.g. Kriss & Canizares 1982) and optically selected samples (e.g. Zamorani *et al.* 1981; Kriss & Canizares 1985). Fig. 8 shows that this correlation also exists in the EMSS and HGLS AGN (although the latter is not as tight).

We investigate the relationship between X-ray and optical luminosity directly using their ratio parametrized by α_{ox}

which, following Tananbaum *et al.* (1979), is defined by:

$$\log \frac{L_{2500\,\text{Å}}}{L_{2\,\text{keV}}} = 2.605\,\alpha_{\text{ox}},$$

where $L_{2\,\text{keV}}$ is the monochromatic luminosity at 2 keV and $L_{2500\,\text{Å}}$ is the optical monochromatic luminosity at 2500 Å in the AGN rest-frame.

We have defined a corresponding index for the soft-component luminosity, α_{os}, which is given by:

$$\log \frac{L_{2500\,\text{Å}}}{L_{0.2\,\text{keV}}} = 1.605\,\alpha_{\text{os}},$$

where $L_{0.2\,\text{keV}}$ is the monochromatic luminosity at 0.2 keV. Similarly, we define the soft-to-hard X-ray index, α_{sx}, thus:

$$\log \frac{L_{0.2\,\text{keV}}}{L_{2\,\text{keV}}} = \alpha_{\text{sx}},$$

where $L_{0.2\,\text{keV}}$ and $L_{2\,\text{keV}}$ are as given above. Values of α_{ox}, α_{os} and α_{sx} are listed in Table 7 together with the monochromatic luminosities, $L_{0.2\,\text{keV}}$, $L_{2\,\text{keV}}$ and $L_{2500\,\text{Å}}$.

Using the method detailed in Avni *et al.* (1980) which takes into account the upper limits on $L_{2\,\text{keV}}$, we calculate an effective α_{ox} of 1.36 ± 0.05 for the USS secure sources (the *average* detected α_{ox} is 1.37). For the EMSS sample, we calculate an average α_{ox} of 1.33 ± 0.01 (this excludes BL Lac objects, 'normal' galaxies and AGN with an uncertain redshift) and an average of 1.35 ± 0.05 for the HGLS. Due to the redshift effect in the soft-component luminosities, values for α_{os} and α_{sx} are strongly dependent on redshift (see Section 7.1.1) and it is not appropriate to calculate the corresponding averages.

Values of α_{ox} for the secure USS, EMSS and HGLS sources for $z < 0.5$ are plotted against redshift in Fig. 8(c). For the EMSS, the values of α_{ox} are those listed in Stocke *et al.* (1991). We have calculated values of α_{ox} for the HGLS AGN, where the flux at 2500 Å was derived from the V magnitudes using the equations in Schmidt (1968) and the flux at 2 keV was derived in the same manner as the broad-band X-ray flux (see Section 7.2). Note that values of α_{ox} for the USS have been calculated *after* the subtraction of the soft component: EMSS and HGLS values of α_{ox} include any soft-component flux. About two thirds of the USS sources have an α_{ox} which lies within the EMSS range; for these objects, the soft component may be superposed on a 'normal' underlying hard X-ray to optical continuum. The remaining values of α_{ox} are high, suggesting that the hard component is depressed relative to the optical.

The ratios of the broad-band luminosities ($L_{\text{opt}}/L_{\text{hard}}$) for the secure USS, EMSS and HGLS, are plotted as a function of redshift in Fig. 8(d), and bear out the results of the α_{ox} distributions.

7.4 Linewidths

Examination of Table 5 reveals a high proportion of narrow-line objects among the USS sample. A narrow-line Seyfert 1 is defined by Osterbrock & Pogge (1985) as a Seyfert 1 or Seyfert 1.5 galaxy with a broad-line FWHM of less than 2000 km s^{-1}. Osterbrock (1987) reports that approximately 15 per cent of Seyfert 1 and 1.5 galaxies belong to this group. Stephens' (1989) sample of X-ray selected AGN contains 42 potential Seyfert 1 galaxies of which 10 (or 24 per cent) are narrow-line Seyfert 1s. In contrast, when we apply the same criteria to the USS sample, nine out of 17 Seyfert 1 galaxies, or ~50 per cent, have permitted lines with FWHM of less than 2000 km s^{-1}.

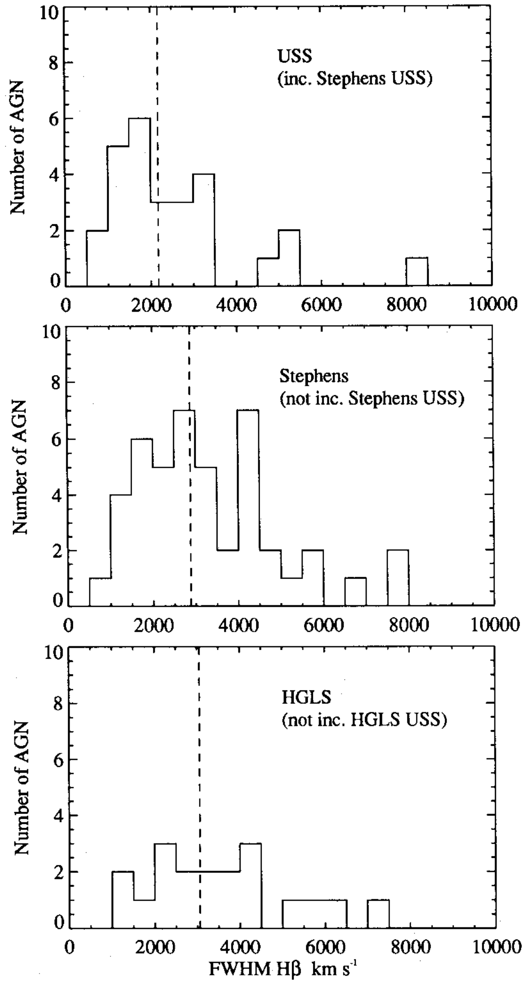

Figure 9. The distribution of the Hβ FWHM for the USS AGN (secure and non-secure sources) compared with the Stephens (1989) sample and AGN from the HGLS. All FWHM have been deconvolved from the instrumental profile. The median of each distribution is indicated by the dashed line.

7.4.1 *Hβ FWHM distribution*

In Fig. 9, we have compared the number distribution of the deconvolved Hβ FWHM for the USS sample with those from the samples of Stephens (1989) and Mittaz (1991; labelled 'HGLS' on the diagram). Only Seyfert 1s and quasars/QSOs are included from each of the three samples.

The Stephens AGN are X-ray selected from *Einstein* IPC data without regard to the X-ray spectral slope. The sample includes 10 USS objects (five secure, five non-secure) as well as those with harder X-ray spectra, and is restricted to objects with redshifts of 0.56 or less. The data on the 10 USS

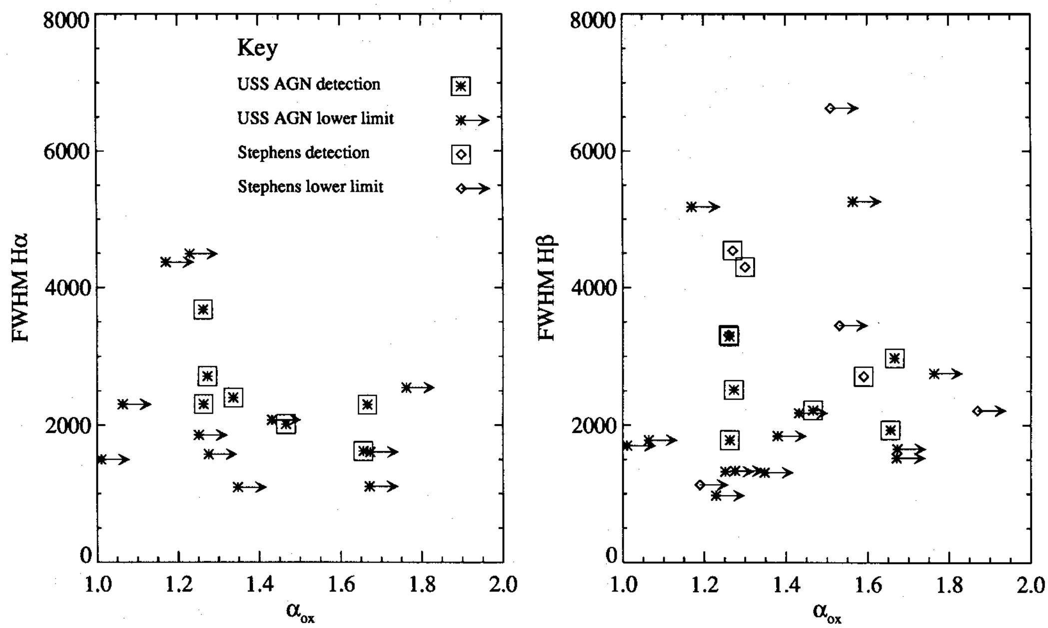

Figure 10. The FWHM of Hα and Hβ plotted as a function of α_{ox} for the USS AGN (secure and non-secure sources). FWHM measured by us are shown as asterisks and those taken from Stephens are plotted as diamonds. A box around an object indicates a measurement of the α_{ox} lower limits to α_{ox} are indicated by the arrows. All FWHM have been deconvolved from the instrumental profile.

objects have been included with our USS measurements, and are excluded from the distribution for the 'Stephens' sample. The FWHM given in the Stephens paper have been deconvolved from the instrumental width.

The Mittaz sample is X-ray selected and is made up of active galaxies identified in the *EXOSAT* High Galactic Latitude Survey (HGLS; Giommi *et al.* 1991). The response of the *EXOSAT* low-energy telescope was biased to lower energies (0.05–2.0 keV) than *Einstein* but the CMA detector used for the HGLS had no intrinsic spectral resolution. Because only a small fraction of the total number of AGN observed by *Einstein* satisfy the USS criteria, we expect that an undifferentiated sample such as the HGLS will contain predominantly 'hard' objects (as does the EMSS), despite the softer energy response of the *EXOSAT* CMA. Indeed, the sample of USS X-ray spectra for which we have optical spectra (secure and non-secure) was best fitted with an 'average' single power law of index 6, much steeper than the index inferred for the HGLS AGN (1.5; Giommi *et al.* 1991). This implies that the HGLS sample is hard in relation to the USS.‡ Two *EXOSAT* HGLS AGN are also USS sources, one secure (E1346+266) and one non-secure (E1059+730). We have deconvolved the HGLS Hβ FWHM from the instrumental width (14.5 Å; Mittaz 1991) to compare them with the USS sample. There is no redshift restriction for the HGLS (the redshift distribution is shown in Fig. 6).

Fig. 9 demonstrates that the Hβ FWHM distribution for the USS AGN is clearly biased to lower widths than the other X-ray selected samples. The median of each sample is indicated by the dashed line and is lowest for the USS AGN (2180 km s^{-1}; *cf.* 3190 km s^{-1} for the HGLS and 3050 km s^{-1} for Stephens).

The comparison between the USS and the Mittaz samples is particularly striking because many of the optical identifications that went into these surveys were made by the same team during the same observing runs and using the same equipment. Therefore, there should be no systematic optical selection bias between these two samples. Also, both sets of optical spectra were reduced using the same software so the method of measuring the FWHM for these samples is consistent. An application of the Kolmogorov–Smirnov (K–S) test indicates that there is an 8 per cent probability that the HGLS and the USS are drawn from the same parent population. There is a corresponding 4 per cent probability for the USS and the Stephens samples.§

These results suggest that the presence of narrow permitted lines is a preferred characteristic of AGN which show the USS phenomenon.

7.4.1.1 Narrow lines and radio properties of AGN. Narrow permitted lines are also a characteristic of core-dominated radio sources; a strong anticorrelation has been reported between the broad-component FWHM of the Hβ line and the ratio of radio core flux density to extended radio lobe flux density, R (Wills & Browne 1986). These authors also found that whereas narrow lines are seen in both core- *and* lobe-dominated quasars, broad lines occur mostly in lobe-dominated quasars.

‡The sample of *secure* USS AGN was best fitted with an average single power law of index 1.9. The difference between these indices is due to the fact that the secure USS are dominated by objects with significant hard components, whereas the sample of AGN with optical spectra has a greater fraction of objects with no detectable hard X-ray flux.

§The K–S test gives a 94 per cent probability that the HGLS and Stephens samples are drawn from the same parent population implying that the *Einstein* IPC and the *EXOSAT* CMA are sampling the same population of X-ray emitting AGN.

7.4.2 *Relationship between Balmer line FWHM and α_{ox}*

Given the high incidence of narrow-line objects in the USS sample, we have looked for a relationship between permitted linewidth and optical and X-ray continuum properties of our sample. There is evidence for an anticorrelation (coefficient = −0.8) between the Hα FWHM and α_{ox}, i.e. sources with a hard X-ray luminosity which is strong relative to the optical luminosity have broader Hα lines. The Hβ data, which include additional data points from Stephens, generally support this correlation and are shown, together with the Hα data, in Fig. 10. This figure also shows upper limits for those objects where the hard X-ray emission is not detected. In general these do not contradict the suggested correlation.

The α_{ox}–FWHM correlation, which is tentative, may only apply in the presence of a strong soft X-ray excess. An investigation into the relationship between the broad-line FWHM and α_{ox} for a sample of objects which have a range of soft X-ray properties, is needed to clarify this (or more specifically, the proper subtraction of any soft X-ray component is required to allow a comparison with our value for α_{ox}). We found no evidence of this correlation in the Stephens sample or in the Stephens subsample of narrow-line objects, but in this case, any soft-component luminosity has not been subtracted before the α_{ox} is calculated.

Blumenthal, Keel & Miller (1982) reported evidence of a *positive* correlation between the half-width at zero intensity (HWZI) of Hβ and α'_{ox} (the ratio of the luminosities at 5000 Å and 2 keV), i.e. in the opposite sense to the relation seen in our data, but they point out that their correlation is mostly due to a few extreme points (and they have made no subtraction of any soft X-ray component).

7.4.3 *Linewidths and continuum luminosities*

There are no significant correlations of the broad-line FWHM with hard X-ray luminosity, soft X-ray luminosity or optical luminosity for the USS AGN. A correlation was reported between the Hβ FWHM and (total; i.e. including any soft-component photons) X-ray luminosity for the Stephens objects (we calculate an associated linear correlation probability of 99.9 per cent for the Stephens sample).

Evidence for a correlation between Balmer line HWZI (which is taken as a representation of the innermost radius of that line-emitting region) and the X-ray luminosities of Seyfert galaxies has been reported (e.g. Kriss, Canizares & Ricker 1980), but this was not seen by Blumenthal *et al.* (1982) in their sample of 23 quasars. A correlation has been reported between the Hβ HWZI and bolometric luminosity, L_{bol}, of Seyferts, but again no corresponding correlation was found for quasars (Padovani & Rafanelli 1988; Padovani 1989). There is evidence for a correlation of the HWZI of C IV λ1549 with L_{bol} for quasars, but there is no corresponding correlation for the FWHM of C IV λ1549 (Padovani 1989).

7.5 Other line parameters

7.5.1 *Line luminosities*

Strong correlations have previously been reported between the Hβ luminosity and the (total) X-ray continuum luminosity of AGN, and also between the Hβ luminosity and the optical continuum luminosity (e.g. Kriss & Canizares 1982; Blumenthal *et al.* 1982). Stephens' (1989) sample shows similar results for the [O III]λ5007 luminosity as well as Hβ, although the Hβ luminosity is more tightly correlated than [O III]λ5007 with both optical and X-ray luminosities.

7.5.1.1 Broad-line luminosities. In the case of the USS AGN, the Balmer line luminosities are strongly correlated with optical luminosity (see Table 8). There is also evidence for correlations of the Balmer line luminosities with both $L_{0.2\,keV}$ and $L_{2\,keV}$ (although there are fewer data pairs for the $L_{2\,keV}$ correlation because many sources for which we have optical spectra have only upper limits to their hard X-ray luminosity; out of seven such data pairs, only three are secure sources). A similar dependence is found for the luminosity in the He I λ5876 line with soft X-ray and optical continuum luminosities (correlations with L_{hard} have not been made because there are only four data pairs).

There are no correlations between the Mg II λ2798 luminosity and the optical luminosities. Although there is no correlation with $L_{0.2\,keV}$, there is a correlation with L_{soft}. Correlations with the hard component were not possible because there was only one data pair (due to the wavelength coverage of the optical spectra and the number of upper limits to the hard X-ray component).

7.5.1.2 Forbidden lines. The luminosity in the narrow, forbidden [O III]λ5007 line is correlated with $L_{2\,keV}$ and $L_{0.2\,keV}$ for the USS AGN. The [O III]λ5007 luminosity is also correlated with L_{opt} but this is not as strong as for the Balmer lines (confirming the Stephens results) and He I λ5876.

7.5.1.3 A comparison with predicted broad-line ratios. USS AGN line ratios have been compared with the models of Krolik & Kallman (1988) who calculated UV and optical line ratios for three different models; a 'bare power law' (with an index of 1.2 for energies <2 keV and 0.7 for energies >2 keV), a '10-eV bump' spectrum and an '80-eV bump' spectrum. The two 'bump' spectra are the sum of the bare power law and a simple accretion disc (e.g. Shakura & Sunyaev 1973), which is geometrically thin and optically thick. Krolik & Kallman compared these (27) models with the list of observed line ratios compiled by Kwan & Krolik (1981) and found that the 10-eV bump model was the best fit.

A He I λ5876/Hβ ratio typical of the USS AGN (average ratio for the USS is 0.15) was reproduced by the 10-eV Krolik & Kallman model, which predicted ratios in the range ~0.14–0.20. The other Krolik & Kallman models predict ratios which are generally too low. The 10-eV model also agrees well with the He I λ5876/Hβ ratios for the samples of Osterbrock (1977; ratio = 0.18) and Stephens (ratio = 0.18). The USS AGN ratios of Hα/Hβ and Mg II λ2798/Hβ are also similar to those predicted by the 10-eV model, as are the UV line ratios of E0132−411, which include Lyα/Hα (~10).

7.5.1.4 [O III]λ5007/Balmer line ratios. Grindlay *et al.* (1980) found a correlation between the [O III]/Hβ luminosity ratio and X-ray luminosity for radio-quiet, X-ray selected objects. Steiner (1981) confirmed this correlation in his low-redshift ($z<0.7$) AGN but only for objects with Fe II emission lines. Kriss & Canizares (1982) found no significant correlation in their data but point out that their sample is much smaller. There is evidence of a correlation of this ratio with R, the ratio of core-to-extended radio luminosity, which is an indicator of the angle of the radio axis to the line of sight (Jackson & Browne 1991). While we could find no correlation between the [O III]/Hβ ratio and the separate X-ray luminosities for the USS sample, there is evidence for a correlation with the FWHM of Hβ and this is shown in Fig. 11 with the Stephens sample for comparison (there is also a corresponding correlation with α_{ox} – see Section 7.4.2).

7.5.2 *Equivalent widths*

There are correlations between the Balmer line equivalent widths (EWs) of the USS AGN and the hard X-ray luminosity. No similar correlation was found in the Stephens narrow-line AGN, but the hard X-ray luminosities in this sample have not been corrected for any contaminating soft X-ray component. There are also weak correlations of the Balmer line EWs and the optical luminosity in the USS data. There are weak correlations between the Balmer line EWs and He I λ5876 EWs with $L_{0.2\,\mathrm{keV}}$, but note that the EWs of Hα and He I have a similar degree of correlation with redshift. There are also correlations between the broad-line EWs and α_{sx}.

Jackson & Browne (1991) found a strong anticorrelation between the [O III]λ5007 equivalent width and R, the ratio of core-to-extended radio luminosity, for their sample of radio-loud quasars and suggest that this is due to anisotropic optical emission, for instance angular-dependent emission in the case of an accretion disc model. There is no correlation of the [O III]λ5007 EW with L_{opt} or $L_{0.2\,\mathrm{keV}}$ for the USS AGN, although there is a correlation with $L_{2\,\mathrm{keV}}$. There is no dependence of the [O III] equivalent width on the Balmer line FWHM.

The EWs of the broad lines (Hα, Hβ and He Iλ5876) in the USS AGN are generally low compared to the Stephens sample. The [O III]λ5007 EWs for the USS AGN are typical of the Stephens sample.

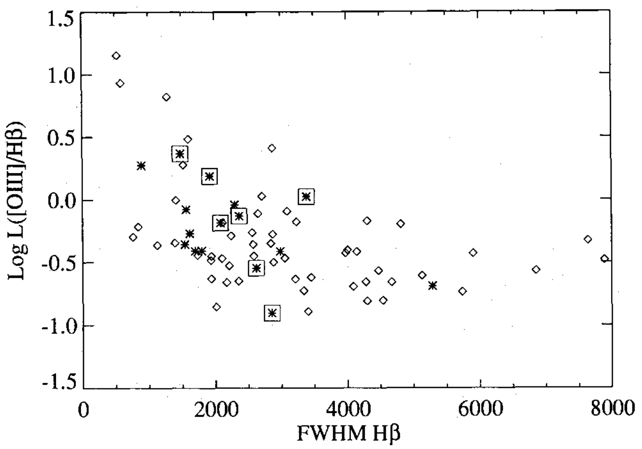

Figure 11. The [O III]λ5007/Hβ luminosity ratio plotted as a function of the Hβ FWHM for the secure and non-secure USS AGN. Ratios from measurements made by us are plotted as asterisks (secure USS in boxes), while measurements taken from Stephens (1989) are plotted as diamonds.

7.5.2.1 *The Baldwin effect.* The 'Baldwin effect' is a term originally used to describe the anticorrelation between the equivalent width of the C IV λ1549 line and the continuum luminosity, L_{ν}, at that line centre (Baldwin 1977; Baldwin *et al.* 1978). Kinney, Rivolo & Koratkar (1990), from *IUE* spectra of 101 quasars and 88 Seyferts, found that this effect extends over seven decades in luminosity and is also seen in the Lyα line.

We have tested the optical spectra of the USS AGN for the Baldwin effect and we find weak *correlations* for the Hα and Hβ lines (coefficient = 0.5; note that this is in the *opposite* sense to the Baldwin effect) and no significant correlation for He I λ5876, [O III]λ5007 and Mg II λ2798. There is a correlation between the Hα EW and redshift (coefficient = 0.7) which may make a contribution to the EW(Hα)/L_{ν} correlation, but there is none between the Hβ EW and redshift.

7.6 Optical Fe II emission-line parameters

7.6.1 *Fe II luminosities*

We find very strong correlations of the Fe II red and blue blend luminosities, L_{blue} and L_{red}, with the optical luminosity (these correlations are also seen in the Stephens subsample of narrow-line objects) and the optical power-law index. There are correlations with $L_{0.2\,\mathrm{keV}}$ and a very weak correlation of L_{blue} with $L_{2\,\mathrm{keV}}$ (the associated correlation probability is 70 per cent). There are strong correlations between L_{blue}, α_{ox} and α_{sx}, but these are based on only five data pairs. There is also an anticorrelation between L_{blue} and α_{os}, but both quantites also depend on redshift.

Table 8(b) also lists a weak anticorrelation (-0.7) between the L_{blue}/Hβ ratio and the hard X-ray luminosity, with an associated correlation probability of 85 per cent. This result is in agreement with the results of Joly (1987), whose model requires that the ionizing flux must be *low* to suppress the Hβ emission relative to Fe II. We point out, however, that the correlation is based on few data pairs (five; although the upper limits in general do not contradict the suggested correlation).

7.6.1.1 *Correlations with other emission lines.* There are weak anticorrelations of L_{blue} and L_{red} with the FWHM of Hα (coefficients of -0.5 and -0.7 for L_{blue} and L_{red} respectively). The Fe II luminosities are strongly correlated with the broad-line luminosities (coefficients ~ 0.9) but less so with the [O III]λ5007 luminosity (coefficients ~ 0.7–0.8). The L_{blue}/L_{red} ratio is weakly correlated with the He I luminosity (coefficient = 0.7 for eight data pairs). There are also anticorrelations between the Fe II$_{red}$/Hβ and Fe II$_{blue}$/Hβ ratios and the broad-line EWs (~ 0.6–0.8).

There is a weak correlation between the Fe II luminosities and the FWHM of [O III]λ5007 and, although we found no correlation between the [O III]λ5007 FWHM and Fe II luminosity for the Stephens (1989) sample as a whole, for the narrow-line Stephens objects there is a weak correlation with L_{red} (coefficient = 0.7 based on seven data pairs).

7.6.2 *Fe II equivalent widths*

Zheng & O'Brien (1990) found that the optical Fe II EW is higher when the Hβ FWHM is narrow and suggested that this is due to an aspect dependence which is consistent with the models of Collin-Souffrin *et al.* (1988; see Section 8.2.2 for a brief description). Jackson & Browne (1991) report a correlation between the Fe II/[O III] ratio and the ratio of core-to-extended radio luminosity, *R*, and also attribute it to the aspect dependence of Collin-Souffrin *et al.* We have found a dependence similar to that reported by Zheng & O'Brien (1990) between the Fe II_{red} and Fe II_{blue} EWs and Hβ FWHM for the Stephens sample (38 objects).

In Fig. 12 we plot Hβ FWHM versus Fe II equivalent width for the USS AGN and compare them with the Stephens sample. Upper limits for the USS AGN are indicated but these were not available for the Stephens AGN. The plot shows that for the Fe II_{red} EW, the USS AGN lie within the Stephens range and have relatively high EWs (again, we point out that upper limits for the Stephens sample are *not* included). For Fe II_{blue}, several of the USS AGN have relatively low EWs at low Hβ FWHM when compared to the Stephens AGN, but the remainder lie within the range of the Stephens sample. However, we caution that there may be systematic differences in the measurements of Fe II between the USS and the Stephens samples, even though we have tried to follow the same procedure.

For both samples, there is an absence of objects at high equivalent width and high FWHM. There are no significant correlations in the USS data between the Fe II equivalent widths and the Hβ and Hα FWHM. However, the range of FWHM for the USS is comparatively narrow; the Zheng & O'Brien (1990) sample extends to FWHM(Hβ) of 11 000 km s^{-1} and the Stephens sample to 8000 km s^{-1}, whereas for the USS the FWHM lie mostly below ~3000 km s^{-1}.

7.6.3 *Fe II emission and the soft X-ray excess*

In a sample of nine low-redshift ($z < 0.3$) quasars, Wilkes, Elvis & McHardy (1987) found that the optical Fe II emission was correlated with the index of a single power law fitted to IPC data in the 0.1–3.5-keV range, in the sense that AGN with steeper soft X-ray slopes (i.e. soft-excess objects) showed stronger Fe II emission (at 99.8 per cent significance). Remillard & Schwartz (1987) found a similar relation from the optical spectroscopy and *EXOSAT* spectra of hard X-ray selected quasars, as did Kruper *et al.* (1990) in the *Einstein* spectra of 11 Seyfert galaxies. However, Zheng & O'Brien (1990), in their sample of 33 predominately low-redshift QSOs, found no correlation between the soft X-ray slope and optical Fe II EW.

Considering the properties of the sample as a whole, we note that the X-ray spectra of those USS AGN for which we have measured Fe II parameters are best fitted with an 'average' single power law of index 6 (see Section 7.4.1). This is much steeper than that inferred for the HGLS (1.5) and for samples of X-ray-bright AGN detected with *Einstein* in the 0.1 – 4.0 keV range (~1; Wilkes & Elvis 1987; Canizares & White 1989; Kruper *et al.* 1990). The Fe II equivalent widths of the USS AGN are generally high when compared to the Stephens sample, which would be consistent with the Wilkes *et al.* effect.

We may consider the α_{sx} as a measure of the slope of the *composite* X-ray spectrum for individual objects, but unfortunately there are few measurements of α_{sx} for those sources which have optical spectra (due to the high number of upper limits to the hard X-ray flux), and α_{sx} has a strong redshift dependence (due to the redshift dependence in $L_{0.2\,keV}$). With these caveats, we have found no correlations between the equivalent widths of the red and blue Fe II blends and α_{sx}. There is a correlation between L_{blue} and α_{sx}, although both of these quantities are also correlated with redshift. There are also correlations between L_{red} and L_{blue} with $L_{0.2\,keV}$.

7.7 Optical power-law index

The distribution of the power-law index measured from the optical spectra, α_{opt}, is shown in Fig. 13 (see Section 3.2.4 for a description of this parameter). The diagram illustrates that the USS selects AGN with a wide range of optical continuum slopes. There is a strong correlation of α_{opt} with the optical luminosity in the sense that brighter objects are bluer. There are weaker correlations of α_{opt} with $L_{0.2\,keV}$ and $L_{2\,keV}$.

Both broad- and narrow-line luminosities are strongly correlated with the optical power-law index (except Mg II

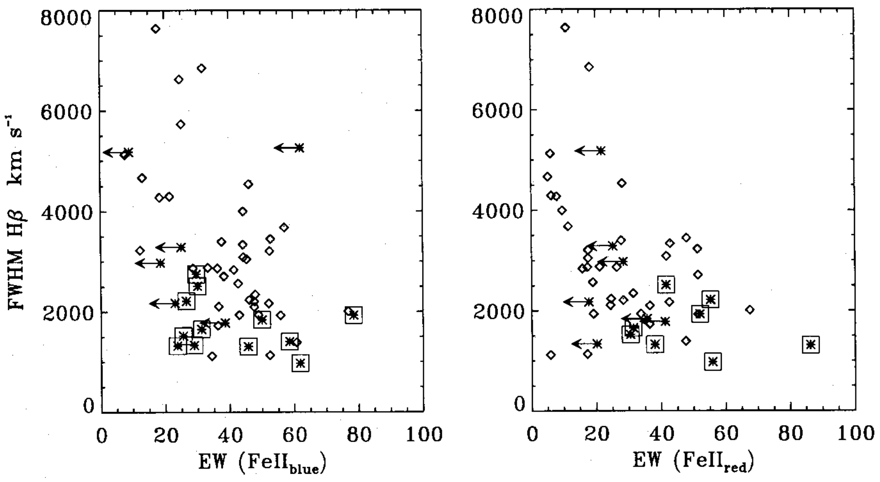

Figure 12. The Hβ FWHM plotted as a function of the equivalent widths of the red and blue Fe II blends for the USS AGN (asterisks in boxes). Values taken from the Stephens sample are plotted for comparison (diamonds). Upper limits to the Fe II equivalent widths are indicated by arrows. Secure and non-secure sources are included.

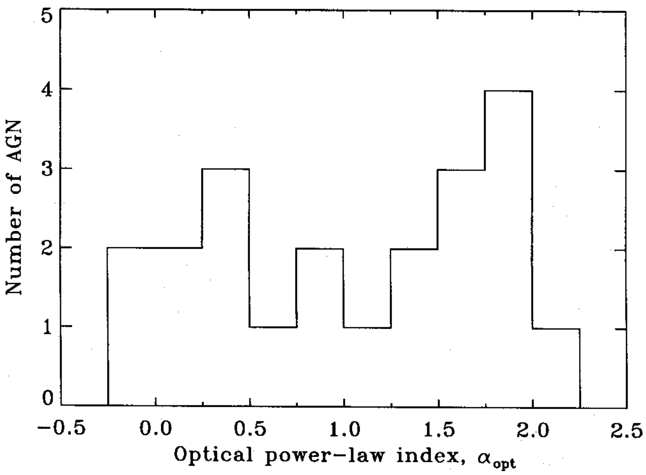

Figure 13. The distribution of the optical power-law index for the secure and non-secure USS AGN (see Section 3.2.4 for a description of this parameter).

λ2798), and the correlation is strongest for the broad lines. Also, the broad-line EWs (except Mg II) are correlated with α_{opt} (especially Hα), but there is no significant correlation for [O III]λ5007. There is a weak anticorrelation of the Mg II EW with α_{opt}.

The strong correlations of α_{opt} with L_{opt}, $E_{2500\,Å}$ and the Balmer and He I λ5876 line luminosities may prove to be powerful indicators of the optical spectral parameters, especially if these correlations are seen in the lines and continuum of a single, varying source.

8 DISCUSSION

In this section we briefly summarize those aspects of AGN models relevant to our work. This is followed by an interpretation of the USS AGN properties and their implications for models of AGN.

8.1 Models for the origin of the X-rays

We begin with a brief description of the models for X-ray emission in AGN before discussing models of the optical line and continuum emitting regions.

8.1.1 *Accretion disc models*

In the accretion disc model of AGN, the soft X-ray excess is believed to be the high-energy tail of the thermal radiation spectrum which is emitted from the inner parts of the disc. The observed strength of the soft X-rays is a function of the angle between the line of sight and the axis of the disc. How the observed strength of the soft excess varies with this angle depends on the type of disc, i.e. whether it is geometrically thick or thin. Sun & Malkan (1989) have investigated the dependence of a thin accretion disc spectrum on the angle of inclination. They found that the emitted disc spectrum shifts to higher energies as the angle of inclination increases, so that discs seen edge-on have the largest soft X-ray excess. In the case of a thick disc, a major fraction of the luminosity is radiated from the funnel-shaped, inner surface of the disc, so that the soft X-ray excess is strongest when the system is viewed face-on, into the cone of emitted radiation (Madau 1988).

Production of the hard X-ray spectrum is believed to be separate from the soft emission for the accretion disc models. Several mechanisms have been suggested, including synchrotron self-Compton models (e.g. Zdziarski 1986), inverse-Compton scattering of soft X-ray photons (e.g. Shapiro, Lightman & Eardley 1976) and electron–positron pair production (e.g. Done & Fabian 1989).

8.1.2 *The 'cool clouds' model*

A soft X-ray excess may also be produced in the 'cool clouds' model proposed by Guilbert & Rees (1988). In this model, relatively cool clouds, confined by a magnetic field or hot, intercloud plasma, exist close to the centre of the active nucleus and perhaps within the central continuum source itself. The primary non-thermal radiation is reprocessed by these small, dense clouds; hard X-rays are absorbed and then reradiated as thermal UV and EUV continuum emission and line features. Under certain conditions, this model reproduces both the soft X-ray excess and the hard X-ray continuum, as well as the optical-UV 'big blue bump' (e.g. Puchnarewicz *et al.* 1992).

8.2 Models of the optical emission-line regions

The broad permitted lines and narrow forbidden lines in the optical and UV spectra of quasars and Seyfert galaxies must be formed in two, spatially distinct regions. These are termed the Broad-Line Region (BLR) and the Narrow-Line Region (NLR). As noted in Section 3.2.5, there is a class of NL Seyfert 1 galaxies which have permitted lines with FWHM $H\beta < 2000$ km s^{-1} (Osterbrock & Pogge 1985). Goodrich (1989) has verified that the narrow permitted lines in his sample of NL Seyfert 1s are indeed emitted from the 'BLR', and are distinct from lines which are formed in the NLR.

8.2.1 *The 'standard' model*

In the 'standard' model of the BLR, the emission lines are formed in clouds and surrounded by either an outflowing wind or perhaps part of the accretion flow. These cold ($T \sim 10^4$ K) line-emitting clouds, which have densities $\sim 10^{10}$ cm^{-3}, may be confined as filaments by magnetic fields (Rees 1987), they may be pressure-confined by a hot intercloud medium (although recent work has cast doubt on this, e.g., Fabian *et al.* 1986; Mathews & Ferland 1987; Rees, Netzer & Ferland 1989), or the clouds may be winds or coronae surrounding stars (Penston 1988). Each standard BLR cloud is divided into two zones (e.g. Kwan & Krolik 1981). Facing the continuum source is a highly ionized zone which draws its energy from the UV and soft X-ray ionizing continuum in the 13.6–500-eV range and emits high-ionization lines (HIL). In the back of the cloud lies the extended ionized zone which draws its energy from the medium X-ray range and emits low-ionization lines (LIL), including most of the Balmer lines, Mg II and the Fe II lines

8.2.2 *A two-component model*

Collin-Souffrin *et al.* (1988) discuss a two-component broad emission line model for AGN, where the HIL are produced in a region distinct from that which produces the LIL, instead of being produced within the same cloud. The HIL are produced in clouds of cooling gas behind shocks in a hypersonic flow of interstellar matter (Perry & Dyson 1985), whereas the LIL are formed in the outer parts of the accretion disc by hard X-rays which are scattered back into the disc from gas behind the shocks in the flow.

8.2.3 *A model for NGC 5548*

Strong observational constraints on the structure of the BLR have recently been provided by flux variability studies of the Seyfert 1 galaxy NGC 5548.¶ Line and continuum emission was monitored in the UV (Clavel *et al.* 1991) and the optical (Peterson *et al.* 1991) over a period of eight months. These observations show that changes in the UV and optical continua were simultaneous from ~1300 to 5000 Å. The amplitude of the continuum variation decreased as the wavelength increased, i.e. the spectrum was 'bluer' when it was brighter (*cf.* Section 7.7). The time taken for the lines to respond to changes in the continuum depended on the degree of ionization of the line; it was shortest for the HIL and longer for the LIL. The amplitude of the variation in the lines also depended on the degree of ionization, being high for the HIL and low for the LIL.

Krolik *et al.* (1991) proposed that the BLR of NGC 5548 has two zones with different physical conditions. Stretching from ~4–14 light-days from the centre lies the inner, high-pressure, high-ionization zone which has a roughly spherical distribution. Beyond this and at least ~20–30 light-days from the central source is the low-ionization zone which is probably flattened; it may be an annulus with a radius of ~100 light-days (and which lies approximately edge-on to the line of sight for the case of NGC 5548).

8.2.4 *Models for the optical Fe II production*

Finally, we consider the production of the optical Fe II blends. In the standard BLR model, hard X-rays (≥800 eV; Krolik & Kallman 1988) penetrate deep into the broad-line clouds and create a warm, partially ionized zone at high optical depths where low-ionization lines, including Fe II and the Balmer lines, are produced (Kwan & Krolik 1981). In the two-component model of Collin-Souffrin *et al.* (1988) these lines are formed in the outer parts of the accretion disc by hard X-rays which are scattered back into the disc (see Section 8.2.2). In the angular-dependent model of Netzer (1987), strong Fe II and Balmer emission do not originate in the same region: Fe II lines are produced in the plane of the accretion disc and the Balmer continuum above the poles. All of these models predict that the strength of the optical Fe II emission increases with the hard X-ray flux.

In an alternative scheme proposed by Joly (1991) and based on the Norman & Miley (1984) model, strong optical Fe II (relative to Hβ) is emitted in the interaction layer between the jets and the region through which they propagate. This region, which is in collisional equilibrium, demands a very weak or no external radiation field, therefore it must be shielded from a power-law continuum (Joly 1987).

¶There is a soft X-ray excess in the spectrum of NGC 5548 (Turner & Pounds 1989; Nandra *et al.* 1991), and X-ray variability studies by Branduardi-Raymont (1989) have shown that the X-ray spectrum is softer when the source is brighter.

8.3 Interpretation of the USS AGN results

The USS survey selects objects which have a high ratio of counts in the 0.16- to 0.56-keV energy band compared to the 0.56- to 1.08-keV energy band. This favours objects with a narrow range of spectral properties which, for AGN, is redshift dependent because the selection is made in the frame of the observer (see Section 7.2.1). Most of the AGN in the sample have redshifts <0.5 and a soft component with a blackbody temperature near to a mean of 10 eV in the rest-frame. Of necessity, the Galactic absorption column in the line of sight to the USS AGN must be low in order for us to see soft X-rays. The UV and optical reddening is therefore also small ($N_H = 2 \times 10^{20}$ corresponds to $A_V = 0.1$). Further, the extinction in the *host* galaxy must also be low!

USS AGN are selected according to their *soft* component flux, and we find a much larger range of *hard* X-ray to optical luminosity ratios than in samples selected at higher X-ray energies. A third of the USS AGN have very low or no detected hard X-ray flux in the IPC energy range. An example is E0132−411 (Fig. 5), whose hard X-ray flux is at least a factor of 30 lower than that of the nearby Seyfert Mkn 841 as a proportion of the optical, UV and soft X-ray continuum. The existence of objects like E0132−411 challenges the suggestion (e.g. Avni & Tananbaum 1982) that all broad-line AGN, i.e. all Seyfert 1s and quasars, are hard X-ray loud.

8.3.1 *X-ray and optical continua*

The X-ray to optical continua of the USS AGN fall into two main categories (see Section 7.3). For approximately two thirds of the AGN, the strong soft component is superposed on a 'normal' underlying hard X-ray continuum. The remaining objects have a significant deficit of X-rays, or no detected hard X-ray component, when compared to other X-ray selected AGN. In both cases, the optical luminosities of the USS AGN are typical of X-ray selected AGN for which USS-type soft X-ray excesses are not observed. (It is important not to rule out the possibility that *intrinsic* soft X-ray excesses, which are not *observed* due to absorption or inclination effects, may occur in other, and perhaps all, AGN.)

8.3.1.1 X-ray and optical continua in an accretion disc model. For a thick accretion disc model, the optical portion of the disc spectrum is brightest when the disc is viewed face-on (Madau 1988). The difference in the observed optical luminosity between a pole-on view and an edge-on view of a thick disc is half a decade when reflection of photons from the funnel walls is taken into account. Therefore, if the presence of a soft X-ray excess in the USS AGN indicates that these contain face-on thick accretion discs, we would expect them to appear optically bright when compared with a sample of randomly orientated AGN. This model is in agreement with the results of Jackson & Browne (1991; see Section 7.5.1) who, based on optical and radio observations of AGN, suggest that the optical emission is anisotropic and, for an accretion disc, would be strongest when the disc is seen face-on.

For the thin accretion disc model (Sun & Malkan 1989), soft X-ray excesses at ~0.2 keV are seen in edge-on systems. The disc spectrum shifts to higher energies as the angle of inclination increases and plots of the Sun & Malkan models show that the *optical* emission observed from a thin disc viewed edge-on is more than two decades *fainter* than when seen face-on.

Neither of these trends is observed in the USS AGN; their optical luminosity distribution is typical of other X-ray selected AGN (see Fig. 8b).‖

8.3.1.2 X-ray and optical continua in the 'cool clouds' model. Ferland & Rees (1988) have calculated model spectra based on the Guilbert & Rees (1988) 'cool clouds' model. Their results show that more hard X-rays are absorbed by clouds as the volume filling factor increases, and the big blue bump grows. This steepens the slope of the optical continuum, but the optical *flux* in the range that we are considering (i.e. from ~2500–7000 Å) shows little change. For this model, then, we would expect AGN with intrinsic soft X-ray excesses to have optical luminosities which are typical of other AGN, and optical power-law indices which are generally steeper. The former is observed for the USS AGN, the latter we are unable to test because there are no data with which to compare them (but see Section 7.7 for the distribution of the USS AGN optical power-law indices). Ferland & Rees caution that this is a preliminary model which should not be directly compared with observations, although the basic principles, i.e. that photoelectric absorption removes X-rays in the medium range and reradiates the energy in the optical to soft X-ray region, still hold.

8.3.2 *The predominance of the narrow Balmer lines*

A striking aspect of the USS AGN is the high proportion of narrow-line objects in the sample. This implies that the broad-line clouds in these systems have low velocities in the line of sight and suggests a link between this and the visibility of the soft X-ray component by which the USS sources are defined. We consider two possibilities; either an inclination effect or a distant BLR. If the broad-line emitting clouds are associated with an accretion disc, or are otherwise confined to circulate in a plane, then an explanation for the narrow permitted linewidths would be that we are viewing the system face-on, i.e. the BLR clouds are circulating in the plane of the sky. Alternatively, assuming that the velocities of the clouds are associated with motion due to the gravitational field of a black hole, the cloud velocities would decrease as their distance from the black hole increased. Thus, the lines would also be predominantly narrow if the BLRs of the USS AGN were further away from the central black hole than for other AGN.

8.3.2.1 A face-on accretion disc? If the narrow lines are evidence of a face-on BLR and the BLR lies in the plane of an accretion disc, then the accretion discs in AGN with strong soft X-ray excesses would be viewed face-on. Thick discs where the strong soft X-ray excess is viewed face-on (Madau 1988) would therefore be favoured over thin discs, where the soft excess is viewed in edge-on systems (Sun & Malkan 1989; but see Section 8.3.1.1). Core-dominated radio quasars, which are believed to be extended double sources seen end-on, also have predominantly narrow permitted linewidths (Wills & Browne 1986). If the radio axis lies perpendicular to the plane of a disc-shaped BLR, then this agrees with a face-on accretion disc geometry (see also Section 7.4.1).

There is tentative evidence that the permitted lines are narrower when the ratio of optical to hard X-ray luminosity, α_{ox}, is high (see Section 7.4). In the context of BLR clouds associated with an accretion disc, this change in α_{ox} would be an inclination effect, i.e. the optical flux decreases relative to the hard X-ray flux as the angle of inclination increases. Such a relationship would be in agreement with the thick-disc model (see Section 8.1.1) provided that the hard X-rays were emitted comparatively isotropically.

8.3.2.2 A more distant BLR? Rather than being associated with a face-on BLR, the narrow lines may be evidence of a BLR which lies further out from the black hole. Krolik *et al.* (1991) have reported a relationship between the broad-line FWHM and the time taken for the line to respond to variations in the continuum for NGC 5548, a measure of the distance to that line-emitting region, and found that the FWHM of the emission lines decrease as the distance increases. This geometry could be tested by monitoring the lines and continuum of a varying USS AGN and measuring the distance to the BLR.

In the case of a distant BLR, an α_{ox} versus broad line FWHM correlation becomes more intriguing, as the distance of the BLR from the central source would be linked to the ratio of the optical and hard X-ray luminosities.

8.3.3 *The strength of the permitted lines*

The Balmer line and He I λ5876 equivalent widths of USS AGN are generally low compared to other X-ray selected AGN and, since we know that the optical continuum luminosities are typical (see Fig. 8b), this implies that the broad-line luminosities are low. Hα and Hβ are produced by photons in the 13.6–54.4-eV range (Krolik & Kallman 1988) as well as hard X-rays; He I λ5876 is produced by 300–500-eV photons. Despite the presence of a strong soft X-ray flux, these lines are *weaker* than in AGN where a soft X-ray excess is not observed. If we assume that the He I and Balmer photons are emitted isotropically, then these results indicate that the soft X-ray excess emission does not communicate with the Balmer and He I line-emitting regions. The correlation (albeit tentative due to the small number of data pairs) between broad-line equivalent width and the hard X-ray component luminosity implies that the hard X-ray flux does communicate with the Balmer and He I line regions.

8.3.3.1 Weak permitted lines in a thick-disc model. Soft X-rays from a thick disc are emitted preferentially in a cone of radiation along the axis of the disc (see Section 8.1.1). Assuming that the BLR is in the plane of the disc, it will lie in the soft X-ray shadow and there would be no communication between the soft X-rays and the BLR. Therefore the line

‖Note, however, that for the thick disc, if reflections from the funnel walls are neglected, then the model predicts a much smaller range of observed optical luminosities, approximately a quarter of a decade (Madau 1988). In this case, the predicted differences in optical luminosity between the USS AGN and other X-ray selected objects would be small.

emission would depend on the observed hard X-ray flux, assuming that the latter is emitted isotropically.

8.3.3.2 The cool clouds model. In the cool clouds model (see Section 8.1.2), both the hard and soft X-ray emission are presumed to be emitted isotropically. Therefore the line-emitting region must be shielded in some way from the ionizing flux *and* there must be no absorbing material along the line of sight to the observer (for the soft X-rays to remain visible). For instance, in the NGC 5548 model of the BLR, the LIL region, where the Balmer and He I lines are produced, is flattened and lies behind the HIL region which absorbs the soft X-rays (see Section 8.2.3). Netzer's model assumes a flattened distribution of 'standard' BLR clouds, in which the soft X-rays are absorbed in the HIL region in the front of the clouds, before reaching the LIL region.

8.3.3.3 A more distant BLR? If the BLR lies a long way from the central ionizing source, the ionizing flux is more dilute and the Balmer and He I $\lambda 5876$ lines would be relatively weak *and* narrow. Therefore shielding from the hard X-rays is not necessary in this case.

8.3.4 *Optical Fe II emission*

The optical Fe II lines are generally believed to be emitted in the presence of a strong X-ray flux (see Section 8.2.4) so we might expect the strength of the Fe II emission to depend on the hard X-ray component. However, the luminosities of the optical Fe II blends are only weakly correlated with hard X-ray luminosity and there are no significant correlations with the EWs (see Section 7.6). While the hard X-ray luminosities of the USS AGN are generally low (see Section 7.2.2), the Fe $\textsc{ii}_{red}$ EWs are generally high (although this may not be true for the blue blend; see Section 7.6.2). There are secure USS AGN which have little or no hard X-ray flux yet strong Fe II emission, e.g. E0132 − 411 and E1423 + 201.

In the model of Joly (1987), no hard X-ray flux is required to produce optical Fe II; indeed the model demands very weak or no ionizing radiation incident on the Fe II-emitting region (see Section 8.2.4). This is necessary to suppress the $H\beta$ emission relative to Fe II. Only two of the USS AGN for which we have optical spectra have measurable Fe II emission *and* a strong hard X-ray flux (E1425 + 169 and E0844 + 377). These objects also have the lowest measured Fe II/$H\beta$ ratio.

8.3.4.1 A dependence on Hβ FWHM. There is evidence that the Fe II strength decreases as the $H\beta$ FWHM increases (see Section 7.6.2). If the observed $H\beta$ FWHM is a measure of the viewing angle, this implies that Fe II emission is anisotropic and is emitted preferentially along the axis of the BLR. Alternatively, if the $H\beta$ FWHM is a measure of the distance to the BLR, then this suggests that the Fe II emission is greater when the BLR is further away from the central source. We note that in the Joly (1987) model, the Fe II/$H\beta$ flux ratio is greatest when the incident radiation is weak or zero.

8.3.4.2 The relationship with the hard X-ray flux. We consider the nature of the Fe II emission from the USS AGN in the context of hard X-ray dependent models of their production. For those sources with weak *observed* hard X-rays, the hard X-ray emission must be enhanced in the direction of the optical Fe II region. Any enhanced hard X-ray emission must be in a direction which is not in the line of sight to the observer *and* it must be directed away from the region which produces the Balmer lines (assuming that these also depend on the hard X-ray flux). The observed hard X-ray emission must correlate with the hard X-rays which reach the Balmer line region. A separation of the optical Fe II and Balmer line regions disagrees with the standard model-type clouds where Balmer lines and optical Fe II are produced in the same region, i.e. in the back of the clouds. In the Collin-Souffrin *et al.* (1988) model, again the Balmer lines and optical Fe II are produced in the same region; the outer part of an accretion disc.

If the He I $\lambda 5876$ and Balmer photons are emitted preferentially in the plane of the BLR, while the Fe II photons are emitted along its axis, then the Fe II and broad lines could be formed in the same region (although enhanced X-ray emission in this zone is still necessary), and the 'standard' and Collin-Souffrin *et al.* models could then apply. In this situation, we would expect to see an anticorrelation between the observed strengths of the Fe II and the Balmer lines. However, we have looked at the $H\beta$ and Fe II EWs from the Stephens (1989) sample (which covers a wider range of Fe II and Balmer line properties than the USS AGN) and we could find no evidence for a correlation of this kind.

For an angular-dependent ionizing continuum model, where a strong EUV excess is viewed in face-on discs, Netzer (1987) found that the Balmer lines and He I $\lambda 5876$ were *not* formed in the same region as optical Fe II. Formation of the Balmer and He I lines was strongest above the poles, while Fe II and Mg II $\lambda 2798$ were strongest in the plane. However, the evidence suggests that Fe II emission is strongest above the *poles* (see Section 7.6.2 and above). This model may be inappropriate for comparison with the USS too; the 'big blue bump' component of the model did not extend sufficiently into the soft X-rays for it to qualify as a USS-type spectrum and the effect of a weak hard X-ray component was not considered.

8.3.5 *Optical Fe II and the soft X-ray excess*

The presence of a soft X-ray excess has been linked to the strength of the optical Fe II emission, via evidence that the steepness of the soft X-ray slope is correlated with the optical Fe II strength (see Section 7.6.3). Unfortunately, analysis of the USS AGN parameters is inconclusive regarding a possible dependence of optical Fe II strength on the soft X-ray excess (mostly due to the strong redshift effect in $L_{0.2\,\mathrm{keV}}$ − see Section 7.6.3), but as a dependence on the hard X-rays would require the conditions discussed in Section 8.3.4, we consider a link with the soft X-ray excess as an alternative.

8.3.5.1 Fe II emission from a thick disc? There are indications (see Sections 7.6.2 and 8.3.4) that optical Fe II emission is anisotropic and is emitted preferentially along the axis of an accretion disc. This would be consistent with Fe II emission from the inner regions of a thick disc or from within the soft X-ray cone itself. It also removes the need for hard X-ray beaming.

If the soft X-ray cone and the radio jet are aligned, this hypothesis would be in agreement with the model of Joly (1991), in which optical Fe II emission is produced in the interaction layer between the radio jets and their surrounding medium. However, the Fe II emitting region must be shielded from the ionizing continuum in this case.

8.3.5.2 Fe II emission from cool clouds. In the cool clouds model, if the optical Fe II emission was dependent on the strength of the soft X-ray excess, we would expect that the Fe II EWs of the USS AGN would be relatively high compared to other X-ray selected AGN (since the optical luminosities would be normal; see Section 8.3.1). Evidence of this effect for the USS AGN is presented in Section 7.6.2. We would also expect to see a correlation of Fe II strength with the slope of a single power law fitted to soft-to-medium X-ray spectra (assuming that this is a measure of the hard X-ray flux absorbed). A dependence of this kind has been reported by previous authors (see Section 7.6.3). When we consider the sample of USS AGN for which we have optical spectra (secure and non-secure), we find that the Fe II strengths are relatively strong and the 'average' index of a single power law fitted to their X-ray spectra is steep (6; see Section 7.6.3).

Since we assume that the cloud spectrum is isotropic, it would be difficult to justify *anisotropic* Fe II emission in this situation, if the Hβ FWHM describes the angle of inclination of the BLR. This may be solved by assuming that the Hβ FWHM is a measure of the distance to the BLR. For the Joly model, then, the Fe II EW would increase with the distance as the ionizing continuum becomes more dilute, resulting in an anticorrelation between Fe II strength and Hβ FWHM.

9 CONCLUSIONS

All of the AGN in this sample have a very strong flux of X-rays in the softest range of the *Einstein* IPC detector, i.e. within 0.16 to 0.56 keV, compared to the flux in the medium range; 0.56 to 1.08 keV. Therefore we know that the amount of absorbing material along the line of sight to the AGN in our Galaxy and the host galaxy must be low. The sample is dominated by narrow-line objects, implying a link between the presence of an observed soft X-ray excess and the relatively low velocity of the line-emitting material in the line of sight. If the FWHM describe the inclination of the BLR, this link favours thick accretion discs over thin, where a strong soft X-ray flux is seen in face-on systems. The Guilbert & Rees cool clouds are another promising mechanism for producing a soft X-ray excess. Alternatively, the low velocity of the permitted lines may be due to a more distant BLR. The separation from the central source to the BLR can be measured directly from the time-lag between line and continuum flux variations. Measurements for objects with a range of FWHM would confirm whether the linewidths depend on the distance to the BLR. The hard X-ray fluxes of the USS are generally low compared to other X-ray selected AGN, and there is tentative evidence for a correlation with the permitted line strengths, which are also relatively low. Their optical luminosities are not distinguishable from those of other X-ray selected AGN. The optical Fe II emission is strong when the hard X-ray flux is weak, contradicting hard X-ray dependent models for the production of the optical Fe II blends, and favouring the Joly model in which no ionizing continuum is required.

Many other aspects revealed by the analysis of these unusual AGN are intriguing, e.g. the anticorrelation between α_{ox} and Balmer line FWHM and the strong correlations between α_{opt} and other optical parameters. Unfortunately, the redshift dependence in L_{soft} may be masking evidence of its relationship with optical properties of the USS AGN, e.g. the strength of the optical Fe II emission. The analysis of a sample of AGN with a range of soft-component strengths is required to search for dependences on the ultra-soft X-ray flux. Observations made with the *ROSAT* satellite will have superior spectral resolution and much greater sensitivity. With the support of a complete and thorough optical programme, a *ROSAT* sample of AGN at the lowest columns will provide a wealth of information for characterizing AGN and constraining current models. We hope that this analysis of the USS AGN will provide a sound foundation for future work on the nature of the soft X-ray component and its effect on the environment of AGN.

ACKNOWLEDGMENTS

The authors would like to thank Gail Reichert for making one of the *IUE* observations, Chris Jomaron for reducing the INT CCD images and Koji Mukai who made the initial spectroscopic identification of E0132 − 411. Alan Smale also assisted with the optical identification programme. We would like to thank Richard Mushotzky for his suggestions and the referee for useful comments. EMP acknowledges an SERC studentship and KOM acknowledges the support of the Royal Society. The WHT, INT and JKT, on the island of La Palma, are operated by the Royal Greenwich Observatory at the Spanish Observatorio del Roque de los Muchachos of the Instituto de Astrofisico de Canarias. This research has made use of the NASA/IPAC Extragalactic Database (NED) which is operated by the Jet Propulsion Laboratory, California Institute of Technology, under contract with the National Aeronautics and Space Administration.

REFERENCES

Allen, C. W., 1973. *Astrophysical Quantities,* 3rd edn, Athlone Press, London.

Allington-Smith, J. R. *et al.,* 1989. *Mon. Not. R. astr. Soc.,* **238,** 603.

Arnaud, K. A., Branduardi-Raymont, G., Culhane, J. L., Fabian, A. C., Hazard, C., McGlynn, T. A., Shafer, R. A., Tennant, A. F. & Ward, M. J., 1985. *Mon. Not. R. astr. Soc.,* **217,** 105.

Avni, Y. & Tananbaum, H., 1982. *Astrophys. J. Lett.,* **262,** L17.

Avni, Y., Soltan, A., Tananbaum, H. & Zamorani, G., 1980. *Astrophys. J.,* **238,** 800.

Baldwin, J. A., 1977. *Astrophys. J.,* **214,** 679.

Baldwin, J. A., Burke, W. L., Gaskell, C. M. & Wampler, E. J., 1978. *Nature,* **273,** 431.

Blumenthal, G. R., Keel, W. C. & Miller, J. S., 1982. *Astrophys. J.,* **257,** 499.

Branduardi-Raymont, G., 1989. In: *Active Galactic Nuclei, IAU Symp. No. 134,* p. 177, eds Osterbrock, D. E. & Miller, J. S., Kluwer Academic Publishers, Dordrecht.

Branduardi-Raymont, G., Mason, K. O., Murdin, P. G. & Martin, C., 1985. *Mon. Not. R. astr. Soc.,* **216,** 1043.

Canizares, C. R. & White, J. L., 1989. *Astrophys. J.*, **339**, 27.
Chanan, G. A., Margon, B. & Downes, R. A., 1981. *Astrophys. J. Lett.*, **243**, L5.
Clavel *et al.*, 1991. *Astrophys. J.*, **366**, 64.
Collin-Souffrin, S., Dyson, J. E., McDowell, J. C. & Perry, J. J., 1988. *Mon. Not. R. astr. Soc.*, **232**, 539.
Córdova, F. A. & Kartje, J. F., 1989. In: *Two Topics in X-ray Astronomy 2. AGN and the X-ray Background, Proc. 23rd ESLAB Symp.* Vol. 2, p. 843, eds Hunt, J. & Battrick, B., ESA Publications Division, Noordwijk.
Córdova, F. A., Kartje, J. F., Thomson, R. J., Mason, K. O., Puchnarewicz, E. M. & Harnden, F. R., 1992. *Astrophys. J. Suppl.*, in press, (C92).
de Robertis, M. M. & Osterbrock, D. E., 1986. *Astrophys. J.*, **301**, 727.
de Ruiter, H. R. & Lub, J., 1986. *Astr. Astrophys Suppl.*, **63**, 59.
Done, C. & Fabian, A. C., 1989. *Mon. Not. R. astr. Soc.*, **240**, 81.
Fabian, A. C., Guilbert, P. W., Arnaud, K. A., Shafer, R. A., Tennant, A. F. & Ward, M. J., 1986. *Mon. Not. R. astr. Soc.*, **218**, 457.
Ferland, G. J. & Rees, M. J., 1988. *Astrophys. J.*, **332**, 141.
Foley, A. R. & Barthel, P. D., 1990. *Astr. Astrophys.*, **228**, 17.
Gioia, I. M., Maccacaro, T., Schild, R. E., Stocke, J. T., Morris, S. L. & Henry, J. P., 1990. *Astrophys. J. Suppl.*, **72**, 567 (EMSS).
Giommi, P. *et al.*, 1991. *Astrophys. J.*, **378**, 77 (HGLS).
Goodrich, R. W., 1989. *Astrophys. J.*, **342**, 224.
Green, R. F., Schmidt, M. & Liebert, J., 1986. *Astrophys. J.*, **310**, 291.
Grindlay, J. E., Steiner, J. E., Forman, W. R., Canizares, C. R. & McClintock, J. E., 1980. *Astrophys. J. Lett.*, **239**, L43.
Guilbert, P. W. & Rees, M. J., 1988. *Mon. Not. R. astr. Soc.*, **233**, 475.
Haniff, C. A., Wilson, A. S. & Ward, M. J., 1988. *Astrophys. J.*, **334**, 104.
Hewitt, A. & Burbidge, G., 1987. *Astrophys. J. Suppl.*, **63**, 1 (HB).
Horne, K., 1986. *Publs astr. Soc. Pacif.*, **98**, 609.
Hutchings, J. B., Crampton, D. & Campbell, B., 1984. *Astrophys. J.*, **280**, 41 (HCC).
Hutchings, J. B., Crampton, D., Campbell, B., Gower, A. C. & Morris, S. C., 1982. *Astrophys. J.*, **262**, 48 (HCCGM).
Jackson, N. & Browne, I. W. A., 1991. *Mon. Not. R. astr. Soc.*, **250**, 422.
Johansson, S., 1986. In: *Physics of Formation of Fe II Lines Outside LTE, IAU Colloq. No. 94,* p. 13, eds Viotti, R., Vittone, A. & Friedjung, M., Reidel, Dordrecht.
Joly, M., 1987. *Astr. Astrophys.*, **184**, 33.
Joly, M., 1991. *Astr. Astrophys.*, **242**, 49.
Kinney, K. L., Rivolo, A. R. & Koratkar, A. P., 1990. *Astrophys. J.*, **357**, 338.
Kriss, G. A., 1982. *PhD thesis,* Massachusetts Institute of Technology.
Kriss, G. A. & Canizares, C. R., 1982. *Astrophys. J.*, **261**, 51.
Kriss, G. A. & Canizares, C. R., 1985. *Astrophys. J.*, **297**, 177.
Kriss, G. A., Canizares, C. R. & Ricker, G. R., 1980. *Astrophys. J.*, **242**, 492.
Krolik, J. H. & Kallman, T. R., 1988. *Astrophys. J.*, **324**, 714.
Krolik, J. H. *et al.*, 1991. *Astrophys. J.*, **371**, 541.
Kruper, J. S., Urry, C. M. & Canizares, C. R., 1990. *Astrophys. J. Suppl.*, **74**, 347.
Kwan, J. Y. & Krolik, J. H., 1981. *Astrophys. J.*, **250**, 478.
Machalski, J. & Condon, J. J., 1983. *Astr. J.*, **88**, 1591.
Madau, P., 1988. *Astrophys. J.*, **327**, 116.
Margon, B., Downes, R. A. & Chanan, G. A., 1985. *Astrophys. J. Suppl.*, **59**, 23 (MDC).
Mathews, W. G. & Ferland, G. J., 1987. *Astrophys. J.*, **323**, 456.
Mittaz, J. P. D., 1991. In: *PhD thesis,* University of London.
Moles, M., Garcia-Pelayo, J., Masegosa, J., Aparicio, A. & Quintana, J. M., 1985. *Astr. Astrophys.*, **152**, 271.
Mukai, K., 1990. *Publs astr. Soc. Pacif.*, **102**, 212.
Mushotzky, R. F., 1984. In: *Advances in Space Research, Vol. 3,* p. 157, eds Bignami, G. & Sunyaev, R., Pergamon Press, New York.
Nandra, K., Pounds, K. A., Stewart, G. C., George, I. M., Hayashida, K., Makino, F. & Ohashi, T., 1991. *Mon. Not. R. astr. Soc.*, **248**, 760.
Netzer, H., 1987. *Mon. Not. R. astr. Soc.*, **225**, 55.
Neugebauer, G., Green, R. F., Matthews, K., Schmidt, M., Soifer, B. T. & Bennett, J., 1987. *Astrophys. J. Suppl.*, **63**, 615.
Norman, C. & Miley, G., 1984. *Astr. Astrophys.*, **141**, 85.
Osterbrock, D. E., 1977. *Astrophys. J.*, **215**, 733.
Osterbrock, D. E., 1987. *Lecture Notes in Physics,* Vol. 307, p. 1, Springer-Verlag, Heidelberg.
Osterbrock, D. E. & Pogge, R. W., 1985. *Astrophys. J.*, **297**, 166.
Padovani, P., 1989. *Astr. Astrophys.*, **209**, 27.
Padovani, P. & Rafanelli, P., 1988. *Astr. Astrophys.*, **205**, 53.
Penston, M. V., 1988. *Mon. Not. R. astr. Soc.*, **233**, 601.
Perry, J. & Dyson, J. E., 1985. *Mon. Not. R. astr. Soc.*, **213**, 665.
Peterson, B. M. *et al.*, 1991. *Astrophys. J.*, **368**, 119.
Puchnarewicz, E. M., Mason, K. O., Córdova, F. A. & Kartje, J. F., 1992. In: *Proc. 2nd Maryland Conference on Testing the AGN Paradigm,* ed. Holt, S., in press.
Rees, M. J., 1987. *Mon. Not. R. astr. Soc.*, **228**, 47.
Rees, M. J., Netzer, H. & Ferland, G. J., 1989. *Astrophys. J.*, **347**, 640.
Remillard, R. & Schwartz, D. A., 1987. *Bull. Am. astr. Soc.*, **18**, 915.
Saikia, D. J., Junor, W., Cornwell, T. J., Muxlow, T. W. B. & Shastri, P., 1990. *Mon. Not. R. astr. Soc.*, **245**, 408.
Schmidt, M., 1968. *Astrophys. J.*, **151**, 393.
Shakura, N. I. & Sunyaev, R. A., 1973. *Astr. Astrophys.*, **24**, 337.
Shapiro, S. L., Lightman, A. P. & Eardley, D. M., 1976. *Astrophys. J.*, **204**, 187.
Shuder, J. M. & Osterbrock, D. E., 1981. *Astrophys. J.*, **260**, 437.
Stark, A., Heiles, C., Baily, J. & Linke, R. A., 1984. Privately distributed tape.
Steiner, J. E., 1981. *Astrophys. J.*, **250**, 469.
Stephens, S. A., 1989. *Astr. J.*, **97**, 10.
Stocke, J. T., Liebert, J., Gioia, I. M., Griffiths, R., Maccacaro, T., Danziger, I., Kunth, D. & Lub, J., 1983. *Astrophys. J.*, **273**, 458.
Stocke, J. T., Morris, S. L., Fleming, T. A., Gioia, I. M., Maccacaro, T., Schild, R., Wolter, A. & Patrick, H. J., 1991. *Astrophys. J. Suppl.*, **76**, 813 (EMSS).
Sun, W.-H. & Malkan, M. A., 1989. *Astrophys. J.*, **346**, 68.
Tananbaum, H., Avni, Y., Branduardi, G., Elvis, M., Fabbiano, G., Feigelson, E., Giacconi, R., Henry, J. P., Pye, J. P., Soltan, A. & Zamorani, G., 1979. *Astrophys. J. Lett.*, **234**, L9.
Turner, T. J. & Pounds, K. A., 1989. *Mon. Not. R. astr. Soc.*, **240**, 833.
Ulvestad, J. S. & Wilson, A. S., 1984. *Astrophys. J.*, **278**, 544.
Urry, C. M., Arnaud, K., Edelson, R. A., Kruper, J. S. & Mushotzky, R. F., 1989. In: *Proc. 23rd ESLAB Symp. on Two Topics in X-ray Astronomy 2. AGN and the X-ray Background,* p. 789, eds Hunt, J. & Battrick, B., ESA Publications Division, Noordwijk.
Wilkes, B. J. & Elvis, M., 1987. *Astrophys. J.*, **323**, 423.
Wilkes, B. J., Elvis, M. & McHardy, I., 1987. *Astrophys. J.*, **321**, L23.
Wilkes, B. J., Masnou, J.-L., Elvis, M., McDowell, J. & Arnaud, K., 1989. In: *Proc. 23rd ESLAB Symp. on Two Topics in X-ray Astronomy 2. AGN and the X-ray Background,* p. 1081, eds Hunt, J. & Battrick, B., ESA Publications Division, Noordwijk.
Wills, B. J. & Wills, D., 1980. *Astrophys. J.*, **238**, 1.
Wills, B. J. & Browne, I. W. A., 1986. *Astrophys. J.*, **302**, 56.
Wisniewski, W. Z., Sitko, M. L. & Sitko, A. K., 1986. *Mon. Not. R. astr. Soc.*, **219**, 299.
Zamorani, G. *et al.*, 1981. *Astrophys. J.*, **245**, 357.
Zdziarski, A. A., 1986. *Astrophys. J.*, **305**, 45.
Zheng, W. & O'Brien, P. T., 1990. *Astrophys. J.*, **353**, 433.

APPENDIX: NOTES ON INDIVIDUAL OBJECTS

* = secure USS AGN.

E0039 − 019, z = 0.35. This is a new USS identification which we have classified as a narrow-line (NL) QSO. No hard X-ray component is detected (i.e. there are no significant counts in the *C3* band). The optical continuum in F_λ rises steeply to the blue (optical power-law index in F_ν, $\alpha_{opt} = 0.3$). The optical spectrum shows narrow Balmer lines and Mg II λ2798, and strong red and blue optical Fe II blends. It appears point-like on the quick V finding chart.

E0111 − 015*, z = 0.12. This X-ray selected object, classified by Stephens (1989) as a NL Seyfert 1, has a strong hard X-ray component. The V magnitude is given by the EMSS as 17.70 (from CCD photometry) and by Stocke *et al.* (1983) as 19.2. The Balmer lines are strong down to Hϵ and the [O III] lines are also strong. The optical continuum is flat. Blue and red Fe II blends are present but the red is weak. It appears slightly extended on the finding chart.

E0114 − 002, z = 0.04. This is a new USS identification and has a strong hard X-ray component. The optical continuum is flat ($\alpha_{opt} = 1.9$) and shows strong features from the underlying galaxy. Hα is relatively narrow compared to Hβ which may be contaminated; [O III] and S II $\lambda\lambda$6717, 6731 are also seen. We have classified this object as a Seyfert 1. It appears extended on the finding chart.

E0129 − 066, z = 0.22. Another new USS identification which is only weakly detected in X-rays with no hard component. The optical continuum rises slowly to the blue (power-law index = 0.8 in F_ν), the Balmer lines are strong and narrow and the optical Fe II blend emission is also very strong. We classify this object as a NL Seyfert 1 and it is point-like on the finding chart.

E0131 − 408*, z = 2.36. An optically selected secure source which has by far the highest redshift of all the USS AGN. The corresponding range of the soft X-ray excess in the rest-frame of the AGN (i.e. the *C1* range), is ~0.5–1.9 keV. The counts in the 1.9–3.6-keV (rest-frame for *C2*) range are relatively low but strong again between 3.6 and 11.8 keV (*C3*). It is point-like on the finding chart which shows no other objects closer to the X-ray position. Lyα and C IV λ1549 have been detected in the UV (HB).

E0132 − 411*, z = 0.27. See Section 6.

E0141 + 020, z = 0.02. This object is better known as Mkn 573, a Seyfert 2. It is a very low-redshift USS AGN and the hard X-ray component is strong. The permitted lines are very narrow; FWHM Hβ = 300 km s^{-1} and FWHM He I λ5876 = 460 km s^{-1} (De Robertis & Osterbrock 1986). Radio maps of Mkn 573 at 6 cm (Ulvestad & Wilson 1984) reveal a triple source whose outer radio components are separated by 3 arcsec. The [O III]λ5007 line emission is aligned with the radio 6-cm emission, but [O III]λ5007 emission at the position of the outer radio lobes is relatively weak (Haniff, Wilson & Ward 1988).

E0150 − 102, z = 0.36. Also known as PHL 1220, this is an X-ray selected source. X-ray counts are very weak in all three bands. From the spectrum in Stephens (1989), it appears to be similar to E0845 + 378, i.e., it has broad and low Balmer lines, the continuum rises steeply to the blue and the [O III] lines are very weak. Classified by Stephens as a quasar/QSO.

E0337 − 267, z = 0.11. The signature of the underlying galaxy is strong in the optical spectrum of this low-redshift USS AGN. The optical continuum is flat ($\alpha_{opt} = 2.1$) and the spectrum shows narrow Balmer lines and the presence of red and blue Fe II blends. E0337 − 267 is a new USS identification and no hard X-ray component is detected. It appears point-like on the finding chart.

E0436 − 433, z = 0.07. The optical spectrum is dominated by light from the underlying galaxy which resembles that of a normal S0 galaxy. Balmer line emission is weak and blended with the galaxy features; the presence of Fe II emission is difficult to determine due to features from the host galaxy. It is a new USS identification and no hard X-ray component is detected. The classification is uncertain but it appears to be a low-luminosity AGN.

E0844 + 377, z = 0.45. The number of X-ray counts detected for this object in all three bands is low, but the hard X-ray component is relatively strong. The optical continuum rises steeply to the blue ($\alpha_{opt} = 0.0$), and shows very strong and narrow emission lines. Blue and red Fe II blends are weak and the red blend is weaker than the blue. Mg II has a strong narrow component and an underlying broad component blended with Fe II. E0844 + 377 is classified in this paper as a quasar/QSO and in Stephens as a Seyfert 1. This source was X-ray selected. Hutchings *et al.* (1982, hereafter HCCGM) report that of all the objects in their sample where they could detect 'fuzz', this has the highest redshift. They also report that it has an extended arc of nebulosity to the north-east and appears to be in a cluster. Hutchings, Crampton & Campbell (1984, hereafter HCC) note that E0844 + 377 is irregular and may be interacting. They derive a corrected ratio of luminosity in the nucleus to luminosity in the surrounding 'fuzz', *Ln*:*Lf*, of 3.0.

E0845 + 378*, z = 0.307. This object has a weak hard X-ray component. From the optical spectrum in Stephens, we note strong Fe II emission and the presence of [O III]$\lambda\lambda$4959, 5007. However, Margon *et al.* (1985: hereafter MDC) report that [O III] is absent but confirm that Fe II is strong. Also from the spectrum in Stephens, the optical continuum rises to the blue and the Balmer lines are broad and low. HCC note that E0845 + 378 has a halo or broad tail and a corrected *Ln*:*Lf* of 0.9. It is an X-ray selected object.

E0906 + 111, z = 0.16. This object also appears in the EMSS and no longer meets the new USS criteria (see Section 2). No hard X-ray component has been detected with the IPC. The optical spectrum shows a flat continuum ($\alpha_{opt} = 1.9$), relatively broad Balmer lines for a USS AGN (FWHM Hβ = 3860 km s^{-1}) and strong [O III]$\lambda\lambda$4959, 5007. Optical Fe II emission is very weak. We have classified this AGN as a Seyfert 1.

E0944 + 464*, z = 0.35. This secure source is a new USS identification and is classified as a NL Seyfert 1. It has no significant hard X-ray component. The Balmer lines are very narrow (deconvolved FWHM Hβ = 1320 km s^{-1}) and the [O III]$\lambda\lambda$4959, 5007 lines are relatively strong. Red and blue Fe II blends are seen in the spectrum; the blue blend in particular is strong. The optical continuum rises to the blue ($\alpha_{opt} = 1.0$).

E0952 + 442, z = 0.47. This AGN has a very strong hard X-ray component and was selected on the basis of its UV excess (HB). It also appears in the EMSS where the presence of Mg II is reported.

E0957 + 561*, $z = 1.41$. This radio-selected object is a gravitationally lensed double quasar and is variable (See HB). A detailed discussion of its soft X-ray emission may be found in C92. It has a high redshift and no hard X-ray component is detected in the *C3* band. The optical power-law index is steep ($\alpha_{opt} = 0.3$) and Mg II $\lambda 2798$ is weak and broad with absorption features either side. The C III]$\lambda 1908$ line is broad and stronger than Mg II, and may be blended with underlying Fe II emission. There is evidence of a strong and narrow C IV $\lambda 1548$ line, but it lies in the noise at the blue end of the spectrum. The two spectra were resolved by Wills & Wills (1980); both spectra show Mg II $\lambda 2798$ as strong as C III]$\lambda 1908$ and the lines have similar profiles, but the continua are flatter than seen in the USS spectrum and rise to the red.

E1008 + 348, $z = 0.14$. This X-ray selected object has a strong hard X-ray component in addition to the soft. Optical spectra are published in Stephens (1989) and Kriss & Canizares (1982), and there are no significant differences between the two. The optical continuum is flat (in F_{λ}). The Hβ FWHM is relatively broad for a USS AGN (3310 km s^{-1}) and optical Fe II emission is not detected (Stephens 1989). Classified by Stephens as a Seyfert 1.

E1011 + 496, $z = 0.20$. This radio-selected source has been identified by Wisniewski *et al.* (1986) as a BL Lac object. The redshift of 0.20 is uncertain and is based on possible membership of the cluster A950. Wisniewski *et al.* give an $\alpha_{ox} \sim 0.9$, (*cf.* our value of > 1.82 which is calculated after the subtraction of the soft component) and an optical spectral index = 1.16. We note that, according to the scheme in the EMSS, this object would be classified as a galaxy, not as a BL Lac, by virtue of its unusually high α_{ox}. It is seen at radio wavelengths as a compact core with a faint extended halo (Machalski & Condon 1983). A slight extension may be seen on the finding chart. No hard X-ray component is detected.

E1028 + 310*, $z = 0.25$. The optical spectrum shows very strong and narrow emission lines; blended Fe II emission is weak. This source has a flat optical continuum slope ($\alpha_{opt} = 1.7$) and lines in the Balmer series are strong down to Hε. It appears point-like on the CCD *R* image, is a new identification and is classified in this paper as a NL Sey 1.

E1040 + 123*, $z = 1.03$. Other names for this AGN include 3CR 245 and 4C 12.37. This is a superluminal radio source (HB) which has a strong hard X-ray component. Radio maps at 6 and 20 cm by Saikia *et al.* (1990) reveal a triple source with a flat-spectrum nucleus and a jet towards the western component which is beamed and curved (Foley & Barthel 1990). The optical spectrum shows a relatively narrow Mg II$\lambda 2798$ line (FWHM = 3750 km s^{-1}; Foley & Barthel 1990). Narrow permitted linewidths and core-dominated radio sources are both associated with a disc-shaped BLR seen face-on (see Section 7.4.1). This source is variable in the optical and high-frequency radio ranges (HB).

E1059 + 730, $z = 0.089$. This is a weak X-ray detection but the hard component is relatively strong. It also appears in the HGLS and in the EMSS. From the spectrum in Stephens, the red Fe II blend appears stronger than the blue. Also, Hα is strong but [N II] is not seen, whereas MDC note that the [N II] emission is strong. The Balmer lines are broad and the Hβ/[O III] lines are badly blended, possibly due to underlying Fe II. The slope of the optical continuum appears flat. This AGN has been classified by Stephens as a Seyfert 1. It appears slightly extended on the quick *V* finding chart. The *V* magnitude is listed in the EMSS as 16.32 (from CCD photometry), and as 14.7 ± 0.5 in Chanan, Margon & Downes (1981). HCC give a ratio of major to minor axis, b/a, of 0.42 and a ratio *Ln:Lf* of 0.57. They describe it as a spiral with an edge-on appearance (possibly due to local obscuration) that may be interacting, and a group/cluster member. HCCGM add that it is one of the two most flattened systems in their sample and has dimensions typical of a large spiral galaxy. This is an X-ray selected source.

E1146 + 558*, $z = 0.44$. This secure USS AGN is a new identification and is classified as a Seyfert 1. The hard X-ray component is weak and the slope of the optical continuum is flat ($\alpha_{opt} = 1.3$). The Balmer lines are broad; only Hα is strong and Hβ is very weak and broad. Blended Fe II emission is weak and may underlie the Hβ and [O III]$\lambda\lambda 4959$, 5007 lines. The [O III] lines are also very weak. Mg II $\lambda 2798$ is very broad and stronger than Hα. The object is extended on the CCD *R* image.

E1213 + 378, $z = 0.82$. This relatively high-redshift object is a new identification, but no longer meets the new USS criteria (see Section 2). The slope of the optical continuum is steep ($\alpha_{opt} = 0.0$). There is strong Fe II emission beneath Mg II $\lambda 2798$ and possibly Hβ, but the strong optical red and blue Fe II emission either side of Hβ is not seen. The Balmer lines (seen from Hβ bluewards) have broad, triangular profiles. This object is point-like on the CCD *R* image and an edge-on galaxy lies 30 arcsec to the south.

E1215 + 692, $z = 1.12$. This is another new USS identification. It has a high redshift of 1.12 and there is no significant detection of a hard X-ray component. The optical continuum is quite steep ($\alpha_{opt} = 0.5$) and Mg II $\lambda 2798$ is broad and may be blended with underlying Fe II emission. There is also evidence for C III]$\lambda 1908$ emission but the spectrum is very noisy in this region. It appears point-like on the CCD *R* image.

E1217 + 695, $z = 0.63$. This is a new USS identification. No hard X-ray component is detected. The optical spectrum shows a continuum which rises steeply to the blue ($\alpha_{opt} = 0$) and generally weak emission lines. Hβ is very weak and broad (it may be broadened by underlying Fe II), [O III]$\lambda\lambda 4959$, 5007 are very weak and Mg II $\lambda 2798$ is weak but narrow. Optical Fe II blends are strong compared to Hβ. It appears point-like on the CCD *R* image and many other galaxies are seen close by.

E1218 + 693, $z = 0.11$. This low-redshift USS AGN is particularly interesting; it is classified in this paper as an H II-region galaxy, yet it has a very strong hard X-ray component. The optical continuum is flat ($\alpha_{opt} = 2.0$), Hα is strong and narrow but Hβ and [O III]/$\lambda\lambda 4959$, 5007 are very weak. Optical Fe II emission is not seen. It appears to be a face-on spiral on the CCD *R* image; the arms are also faintly visible on the *B* image. Many other galaxies can be seen in the field.

E1227 + 140*, $z = 0.10$. Two observations of this X-ray selected object appear in the USS AGN list, one is secure and the other no longer meets the USS criteria (see Section 2). The two X-ray spectra are quite different; both have similar total count rates, but the spectrum of the secure detection shows a strong hard X-ray component whereas the non-USS detection has a weak hard component (see C92 for full details of the X-ray spectral variability). The optical continuum rises slowly to the blue ($\alpha_{opt}=1.6$), Hα and Hβ are broad (FWHM Hβ is 3400 km s^{-1}), and the [O III]$\lambda\lambda$4959, 5007 lines are strong. The red Fe II blend is very weak, whereas the blue blend is strong and blends with Hβ. In Stephens, the optical continuum is flat, there is no red Fe II and the blue blend is weak. The Balmer lines, particularly Hβ whose FWHM was measured by Stephens as 4300 km s^{-1}, are broad. Grindlay *et al.* (1980) found variability in their two spectra of this object which were taken only three days apart. The continuum of the second is more depressed to the blue of Hβ than the first, and they say that emission features in the Hβ profile and at wavelengths of Fe II are marginally significant in the first spectrum but absent from the second. HCC note that this object may be irregular and it may have an associated jet or filament.

E1228 + 123, z = 0.12. This X-ray selected object also appears in the HB catalogue and the HGLS but no longer meets the USS criteria (see Section 2). A hard X-ray component is not detected. It has a flat optical continuum ($\alpha_{opt}=1.6$) and has been classified as a NL Seyfert 1. The spectrum shows narrow Hα and Hβ; Fe II emission is very weak. The CCD *R* image shows a bright nucleus with either a faint ring structure or extension and another extended object about 25 arcsec away. There are no obvious differences between our optical spectrum and that published by Stephens (1989).

E1255 + 220*, z = 0.160. The redshift of this AGN has been listed in the EMSS as uncertain. It is a secure source with no significant hard X-ray component.

E1304 + 342, z = 0.28. There is no significant hard X-ray component in this AGN, which was selected on the basis of its UV excess. Previously a non-secure USS source, it no longer meets the new USS criteria. It appears in the EMSS, HB and Stephens samples. The optical spectrum shows a continuum which rises steeply to the blue (optical power-law index = 0.1 in F_ν), strong narrow Balmer lines, weak [O III] and strong Fe II (the blue blend is stronger than the red). The optical spectrum appears similar in Stephens (1989). It is classified as a Seyfert 1 object and is point-like on the CCD *R* image.

E1334 + 038*, z = 0.136. In the EMSS, the identification for this object is listed as 'tentative' (i.e. it may be a galaxy, LINER, etc.) and it is noted that Hβ may have a broad base and that Mg II is marginally detected. It has a very strong hard X-ray component and is X-ray selected.

E1346 + 266*, z = 0.92. No hard X-ray component has been detected for this source, which also appears in the EMSS survey as well as the *EXOSAT* High Galactic Latitude Survey (HGLS). There is another HGLS source very close by; a $z=0.60$ AGN with a V magnitude of 18.1 which lies approximately 3 arcmin to the east. It has a lower *EXOSAT* count rate (0.0022 count s^{-1}) than the $z=0.92$ AGN (0.0068 count s^{-1}, Mittaz 1991) and is further away from the USS position. The slope of the optical continuum is steep, ($\alpha_{opt}=0.4$), and the emission features are weak. It has been classified as a NL QSO/quasar on the basis of the low FWHM of Hβ (1903 km s^{-1}), but this line is weak and at the red limit of the spectrum where the signal is relatively poor. The FWHM of Mg II λ2798 is 2600 km s^{-1} and may be broadened by underlying Fe II emission.

E1352 + 183, z = 0.15. This X-ray selected source has one of highest X-ray count rates but a weak hard X-ray component relative to the soft. HCC report the presence of a halo or broad tail and a corrected *Ln:Lf* of 7.5. The spectrum in Stephens (1989) shows broad Balmer lines, weak [O III] and blue Fe II stronger than red (both are clearly seen). The optical continuum rises to the blue: it is also a PG quasar and the power-law index was measured by Neugebauer *et al.* (1987) as 1.45 at wavelengths between 10.1 and 1.0 μm and 0.43 between 1.0 and 0.3 μm (see also the notes for E1704 + 608). Classified by Stephens as a Seyfert 1.

E1401 + 098*, z = 0.44. MDC report that this source is located near to the Zwicky cluster ZC 1400.4 + 0940 and 7 arcmin from NGC 5438. The spectrum in Stephens shows an unusual Hβ profile; it appears to be square-shaped and is blended with a feature that underlies the [O III] lines and may be due to Fe II emission. Hγ is also very broad but again this may be partly due to blending with [O III]. The optical continuum rises to the blue, possibly due to strong Balmer continuum emission. This source is classified as a quasar or QSO, and is an X-ray selected source with a very strong hard X-ray component, which shows evidence of X-ray spectral variability (see C92).

E1423 + 201*, z = 0.21. This is a new identification of a secure USS source which we have classified as a QSO. No hard X-ray component is detected. The optical continuum rises steeply to the blue ($\alpha_{opt}=-0.1$), the Balmer lines are strong and the [O III] lines are very weak. Both optical Fe II blends are very strong.

E1423 + 242, z = 0.65. Also known as 4C 24.31 and PKS1423 + 242, the redshift of this radio-selected AGN is uncertain. Although the *Einstein* count *rate* is relatively high, the number of counts detected in all three bands is low and it has a weak hard component.

E1425 + 169*, z = 0.22. We have classified this AGN as a Seyfert 1 galaxy. It is a new secure USS identification which has a strong hard X-ray component. The optical continuum is mostly flat but rises to the blue, possibly due to Balmer continuum emission ($\alpha_{opt}=1.4$). Both red and blue Fe II blends are seen but the red blend is weak.

E1511 + 671, z = 0.31. E1511 + 671, a new USS identification which we have classified as a NL Seyfert 1, has no significant hard X-ray component. The optical continuum rises to the blue (optical power-law index = 0.0 in F_ν), the Balmer lines are strong and narrow (FWHM Hβ = 1800 km s^{-1}), and the [O III] lines are weak. Both Fe II blends are strong and some individual lines are resolved. It is slightly extended on the CCD *R* and *B* images.

E1519 + 279*, z = 0.23. This AGN is X-ray selected yet there is no significant detection in the *C3* band. It appears in the MDC and the Stephens samples. From the spectrum in Stephens, the optical continuum rises to the blue (this may be due to a strong Balmer continuum), the Balmer lines are narrow (FWHM Hβ = 2210 km s^{-1}), [O III]λ5007 is weak and red and blue Fe II blends can be seen. MDC note that Hα is strong and [O III]λ5007 is very weak. It is classified by Stephens as a Seyfert 1.

E1614 + 308, z = 0.27. This is drawn from the EMSS catalogue and may be a BL Lac object. Lines of Mg II λ2798 and Hβ are reported in the EMSS.

E1640 + 537, z = 0.14. This is a new USS identification and has no hard X-ray component. The optical spectrum has poor quality; the continuum is flat ($\alpha_{opt}=1.6$) and there are very weak and possibly broad Balmer lines. The [O III] lines are also weak and Fe II is not seen. It is extended on CCD *R* and *B* images. On the *R* image, it appears to be a face-on, barred spiral galaxy. The arms are very faint, indicating that it may be an anaemic S0-type galaxy. The arms are not seen on the *B* image.

E1654 + 352, z = 0.80. This is a new identification which no longer meets the USS criteria. No hard X-ray component was detected in this relatively high-redshift object. The optical continuum rises very steeply to the blue ($\alpha_{opt} = 0.0$), Hβ and Hγ are weak and broad and the [O III] lines are very weak. The blue optical Fe II blend and the blends around the narrow Mg II λ2798 line are strong. It appears point-like on the CCD *R* and *B* images and is classified in this paper as a QSO.

E1657 + 326, z = 0.09. A very strong hard X-ray component is detected in this low-redshift AGN which is a new USS identification and classified as a NL Seyfert 1. The slope of the optical continuum is flat ($\alpha_{opt} = 2.0$), Hα is strong and broad but Hβ is very weak and may be narrow. [O III]$\lambda\lambda$4959, 5007 are relatively strong and narrow and [S II]$\lambda\lambda$6717, 6731 are also very strong. Features from the underlying galaxy can be seen and are difficult to separate from both red and blue Fe II features. CCD *R* and *B* images reveal this to be an extended object whose major axis lies at a position angle of ~135°. There is another point-like blue object 16 arcsec to the east, i.e. away from the X-ray position. Many other galaxies can be seen in the field.

E1704 + 608*, z = 0.37. This is another PG quasar (see Green, Schmidt & Liebert 1986) and shows variability in its X-ray spectrum over a two-year period – C92 for a full description. A low-resolution spectrum from 0.3 to 10.1 μm is published in Neugebauer *et al.* (1987) and is fitted with a broken power law of $\alpha = 1.67$ in the low-frequency range (> 1 μm) and 0.43 in the high-frequency range (the same as for E1352 + 183). It is a radio-selected source and other names include 3CR 351 and 4C 60.24. HCC report that this object has a halo or broad tail (also like E1352 + 182), and an *Ln*:*Lf* of 4.0 in the *R* band and 14 in the *B* band.

E1805 + 700, z = 0.19. This is a very weak X-ray source with no detectable hard component. It is a new USS identification classified as a NL Seyfert 1. The optical continuum is flat ($\alpha_{opt} = 1.8$ in F_ν), Hα is quite strong and very narrow and Hβ is much weaker. The [O III] lines are also weak and both red and blue Fe II are present (blue is stronger than red). CCD images show a field crowded with other galaxies. The source itself is extended; it appears circular on the *R* image, but more elongated on the blue with the major axis lying at a PA of ~45°. There are five other objects within 40 arcsec of the source and at least two of these are galaxies, but the identified AGN lies closest to the X-ray position.

E2318 − 423*, z = 0.21. This is a secure USS AGN, which has a strong hard X-ray component. It is X-ray selected and is taken from the EMSS.